

AD-A215 948

4

GL-TR-89-0181

**DEVELOPMENT OF A
SUPERCONDUCTING SIX-AXIS ACCELEROMETER**

H. J. Paik, J. W. Parke, and E. R. Canavan

Department of Physics and Astronomy
University of Maryland
College Park, MD 20742

July, 1989

DTIC
ELECTE
DEC 19 1989
S E D

Final Report
April 1, 1985 - March 31, 1988
Approved for public release; distribution unlimited

GEOPHYSICS LABORATORY
AIR FORCE SYSTEMS COMMAND
UNITED STATES AIR FORCE
HANSCOM AIR FORCE BASE, MA 01731-5000

89 12 18 122

REPORT DOCUMENTATION PAGE

Form Approved
OMB No. 0704-0188

| | | | | | |
|--|---|---|---|------------------------------|----------------------------------|
| 1a. REPORT SECURITY CLASSIFICATION Unclassified | | | 1b. RESTRICTIVE MARKINGS | | |
| 2a. SECURITY CLASSIFICATION AUTHORITY | | | 3. DISTRIBUTION / AVAILABILITY OF REPORT Approved for public release, distribution unlimited | | |
| 2b. DECLASSIFICATION / DOWNGRADING SCHEDULE | | | | | |
| 4. PERFORMING ORGANIZATION REPORT NUMBER(S) | | | 5. MONITORING ORGANIZATION REPORT NUMBER(S) GL-TR-89-0181 | | |
| 6a. NAME OF PERFORMING ORGANIZATION University of Maryland | 6b. OFFICE SYMBOL (If applicable) | 7a. NAME OF MONITORING ORGANIZATION Geophysics Laboratory | | | |
| 6c. ADDRESS (City, State, and ZIP Code) Department of Physics and Astronomy College Park, MD 20742 | | 7b. ADDRESS (City, State, and ZIP Code) Hanscom AFB, MA 01731-5000 | | | |
| 8a. NAME OF FUNDING / SPONSORING ORGANIZATION Geophysics Laboratory | 8b. OFFICE SYMBOL (If applicable) LWG | 9. PROCUREMENT INSTRUMENT IDENTIFICATION NUMBER F19628-85-K-0042 | | | |
| 8c. ADDRESS (City, State, and ZIP Code) Hanscom AFB, MA 01731-5000 | | 10. SOURCE OF FUNDING NUMBERS | | | |
| | | PROGRAM ELEMENT NO. 61102F | PROJECT NO. 2309 | TASK NO. G1 | WORK UNIT ACCESSION NO. B1 |
| 11. TITLE (Include Security Classification) Development of a Superconducting Six-Axis Accelerometer | | | | | |
| 12. PERSONAL AUTHOR(S) Paik, Ho Jung; Parke, Joel William; and Canavan, Edgar Richard | | | | | |
| 13a. TYPE OF REPORT Final | 13b. TIME COVERED FROM 4/1/85 TO 3/31/88 | 14. DATE OF REPORT (Year, Month, Day) July 1989 | | 15. PAGE COUNT 110 | |
| 16. SUPPLEMENTARY NOTATION | | | | | |
| 17. COSATI CODES | | | 18. SUBJECT TERMS (Continue on reverse if necessary and identify by block number) | | |
| FIELD | GROUP | SUB-GROUP | Accelerometer, Inertial Guidance, Navigation, Geodesy, Superconductivity | | |
| | | | | | |
| 19. ABSTRACT (Continue on reverse if necessary and identify by block number) | | | | | |
| <p>This report describes research on the superconducting six-axis accelerometer performed at the University of Maryland from April, 1985, to March, 1988, under Air Force Contract F19628-85-K-0042.</p> <p>This report consists of four chapters. After an introduction and summary is given in Chapter 1, Chapter 2 discusses the theory of a superconducting six-axis accelerometer. The construction and test of the superconducting six-axis accelerometer are given in Chapters 3 and 4, respectively.</p> <p>The superconducting six-axis accelerometer described in this report was invented to monitor the platform motions of a superconducting gravity gradiometer which is under development at the University of Maryland for space application. The signals from the accelerometer will be used to control the position and the attitude of the gradiometer platform. The superconducting six-axis accelerometer represents by itself a complete inertial navigation system. Integrated with the superconducting gravity gradiometer, it becomes a gradiometer-aided inertial navigation system.</p> | | | | | |
| 20. DISTRIBUTION / AVAILABILITY OF ABSTRACT <input checked="" type="checkbox"/> UNCLASSIFIED/UNLIMITED <input type="checkbox"/> SAME AS RPT. <input type="checkbox"/> DTIC USERS | | | 21. ABSTRACT SECURITY CLASSIFICATION Unclassified | | |
| 22a. NAME OF RESPONSIBLE INDIVIDUAL Lt. Col. Gerry Shaw | | | 22b. TELEPHONE (Include Area Code) (617) 377-3486 | 22c. OFFICE SYMBOL GL/LWG | |

Contents

| | |
|--|-----------|
| Table of Contents | iii |
| List of Figures | v |
| List of Tables | vii |
| 1. Introduction and Summary | 1 |
| 2. Theory of a Superconducting Six-Axis Accelerometer | 3 |
| 2.1 Introduction | 3 |
| 2.2 Dynamics of a Superconducting Six-Axis Accelerometer | 6 |
| 2.2.1 Dynamics of a Single-Axis Accelerometer in a Rotating, Accelerated Reference Frame | 6 |
| 2.2.2 Dynamics of a Rigid Body in a Rotating Accelerated Reference Frame | 10 |
| 2.2.3 Accelerometer Equations of Motion | 20 |
| 2.3 Superconducting Circuitry | 24 |
| 2.3.1 Levitation Circuitry | 30 |
| 2.3.2 Sensing Circuitry | 36 |
| 2.4 Six-Axis Accelerometer Transfer Functions | 42 |
| 2.5 Fundamental Noise of the Accelerometer | 45 |
| 2.5.1 Transducer Brownian Motion Noise | 46 |
| 2.5.2 SQUID Amplifier Noise | 47 |
| 2.5.3 Potential Sensitivity | 47 |
| 3. Construction of the Superconducting Six-Axis Accelerometer | 52 |
| 3.1 Accelerometer Hardware | 52 |
| 3.1.1 Mechanical Components | 52 |
| 3.1.2 Superconducting Coils | 57 |
| 3.2 Superconducting Circuitry | 59 |
| 3.2.1 Levitation Circuitry | 61 |
| 3.2.2 Sensing Circuitry | 64 |
| 3.3 Construction of the Experimental Test Apparatus | 66 |
| 3.3.1 Thermal and Mechanical Design of the Cryostat | 66 |

| | | |
|-------|---|----|
| 3.3.2 | Electrical Isolation of the SSA | 69 |
| 3.3.3 | Vibration Isolation of the SSA and Shaker Design | 70 |
| 3.4 | Computer Control and Interface Electronics | 72 |
| 4. | Test of the Superconducting Six-Axis Accelerometer | 74 |
| 4.1 | Accelerometer Parameters | 75 |
| 4.1.1 | Levitation and Sensing Inductance Modeling | 75 |
| 4.1.2 | DC Inductance Measurements | 80 |
| 4.2 | Accelerometer Resonant Modes | 80 |
| 4.3 | Calibration and Noise Measurement | 83 |
| 4.3.1 | Sensing Drive Circuitry | 83 |
| 4.3.2 | Residual Misbalance | 86 |
| 4.3.3 | Linear Acceleration | 89 |
| 4.3.4 | Angular Acceleration | 95 |
| 4.4 | Future Improvements | 99 |

Bibliography

101

| | |
|----------------------|-------------------------------------|
| Accession For | |
| NTIS GRA&I | <input checked="" type="checkbox"/> |
| DTIC TAB | <input type="checkbox"/> |
| Unannounced | <input type="checkbox"/> |
| Justification _____ | |
| By _____ | |
| Distribution/ _____ | |
| Availability Codes | |
| _____ | |
| Dist _____ | |
| A-1 | |

List of Figures

| | | |
|------|---|----|
| 2.1 | A schematic illustrating the principle of a superconducting bridge acceleration transducer. | 5 |
| 2.2 | The single-axis accelerometer proof mass coordinate frame. | 7 |
| 2.3 | Schematic of the six-axis accelerometer proof mass. | 11 |
| 2.4 | Perspective view of the six-axis accelerometer proof mass and coil forms. . | 26 |
| 2.5 | Linear superconducting levitation and feedback circuitry. | 31 |
| 2.6 | Angular superconducting levitation and feedback circuitry. | 33 |
| 2.7 | Superconducting sensing circuitry. | 37 |
| 2.8 | Simplified superconducting sensing circuitry for the r_x degree of freedom. . | 38 |
| 2.9 | A schematic illustrating detection of acceleration in the SSA: r_x degree of freedom. | 48 |
| 3.1 | An exploded view of the SSA hardware. | 53 |
| 3.2 | An exploded view of the SSA proof mass. | 55 |
| 3.3 | A schematic drawing of one of the coil forms in the SSA. | 55 |
| 3.4 | An isometric view of the six coil form holders. | 56 |
| 3.5 | An isometric view of the precision mounting cube. | 57 |
| 3.6 | A photograph of the partially assembled SSA. | 60 |
| 3.7 | A schematic of the levitation circuitry. | 63 |
| 3.8 | A schematic of the sensing circuitry. | 65 |
| 3.9 | A schematic of the SSA cryostat insert. | 68 |
| 3.10 | A cross sectional view of the SSA shaker. | 71 |
| 4.1 | A schematic picture of a current loop above a superconducting plane interacting with an image current loop below. | 77 |
| 4.2 | The rf isolation transformer and circuitry used to drive each of the sensing circuits in the SSA. | 84 |
| 4.3 | A bridge circuit containing a small resistive component. | 88 |
| 4.4 | The very low frequency spectra of noise as measured by the r_x and r_z sensing circuits. | 91 |
| 4.5 | The expected low frequency spectrum of seismic noise generated by the earth. | 92 |

| | | |
|-----|--|----|
| 4.6 | The low-frequency spectra of seismic noise as measured by the θ_x , θ_y , and θ_z sensing circuits. | 97 |
|-----|--|----|

List of Tables

| | | |
|-----|---|----|
| 2.1 | Initial position of the center of the superconducting coils with respect to the center of the proof mass in the six-axis accelerometer. | 27 |
| 4.1 | Experimental parameters for the SSA. | 76 |
| 4.2 | Levitation currents, resonance frequencies, and mechanical quality factors for each of the six modes of the SSA. | 82 |
| 4.3 | Parameters for rf isolation circuits in the SSA. | 85 |
| 4.4 | Theoretical parameters for rf isolation circuits in the SSA. | 87 |

Chapter 1

Introduction and Summary

A sensitive superconducting six-axis accelerometer (SSA) has been developed for application in gravity survey and inertial guidance. A breadboard SSA has been constructed and operated to verify the design concepts of the device. The construction of the breadboard SSA followed closely the original design proposed by Paik [4,11]. Based on the experience obtained with the breadboard, an improved model of the SSA has been designed and is under construction.

The design involves a single levitated superconducting proof mass of a special geometry whose motion is monitored in six degrees of freedom. The proof mass has the shape of an inverted cube, three orthogonal square plates bisecting each other, and is made of niobium (Nb). It is levitated on magnetic fields produced by persistent currents in 24 superconducting levitation/feedback coils. Its motion in three linear and three angular degrees of freedom is sensed by 24 superconducting sensing coils, which form six independent inductance bridges. The six bridges are driven at six different frequencies and are detected by a single SQUID, whose output is demodulated to recover the six acceleration signals. The persistent currents in the levitation/feedback coils are adjusted to null the six inductance bridges and the SQUID demodulated signals are fed back to the corresponding levitation/feedback coils to keep the proof mass at the null position.

The coil forms have been machined out of a titanium alloy, TiV4Al6, and all the coils were wound initially with niobium wire. Niobium was chosen because of its high value of H_{c1} so that the coils can be operated in the Type-I region where currents are more stable. All the parts fit inside a 10.16 cm titanium cube.

Two problems were encountered with this design. First, the titanium alloy

used for the coil forms had an unusually low superconducting transition temperature, 4.5 K. Since the magnetic fields should be able to return through the coil forms, we had to operate the SSA at an elevated temperature near 5 K to keep the coil forms from becoming superconducting. In the new model of the SSA, a different alloy of titanium is used whose transition temperature is below 1.5 K. Another problem that has plagued the progress of our research is the brittleness of the thin niobium wires at low temperatures. After a long battle to overcome the problem of wire breaking upon thermal cycling, we resorted to a compromise solution of winding the coils with niobium-titanium (Nb-Ti) wire. Although mechanically strong, the Nb-Ti wire has to be operated in a Type-II region, thereby increasing the drifts in the superconducting circuits. In the improved model, we have gone back to Nb wire to eliminate this problem.

The breadboard SSA has been operated completely. Levitation and balance have been achieved in all six degrees of freedom. The output of a single SQUID has been successfully demodulated to recover the six acceleration signals. The external rf noise, which had been a main concern for operating the bridge sensing circuits at the input of a SQUID, has been filtered sufficiently by means of rf shielded transformers.

In addition to constructing an improved model of SSA, further tests will be carried out on the breadboard SSA under a new Air Force contract. In particular, the effect of oscillator noise and the source of any excess low frequency noise must be investigated. The feedback circuits need to be developed to improve the dynamic range of the device.

The theoretical sensitivity of the SSA is $10^{-12} \text{g Hz}^{-1/2}$ for the linear and $10^{-5} \text{arcsec sec}^{-2} \text{Hz}^{-1/2}$ for the angular acceleration. The SSA of the new design will be integrated with the three-axis superconducting gravity gradiometer (SGG) being developed under a NASA contract. It is envisioned that the combined SGG/SSA package will be flown in the Earth orbit for a gravity mapping mission in the late 1990's. The superconducting gravity gradiometer/accelerometer system with such high sensitivity, if successfully developed, will find many important applications in gravity survey and inertial guidance.

Chapter 2

Theory of a Superconducting Six-Axis Accelerometer

2.1 Introduction

A "six-axis" accelerometer measures the linear and angular acceleration in all six degrees of freedom at the same point in space time. A superconducting six-axis accelerometer operates at liquid helium temperatures and is able to take advantage of the low thermal noise and the extremely high stability of materials and currents, which is a direct consequence of cryogenic temperatures. The six-axis accelerometer uses the properties of quantized magnetic flux to magnetically levitate a single superconducting proof mass with extreme stability. Additional superconducting circuits monitor and control the position of the proof mass. High sensitivity is achieved through the use of a SQUID (Superconducting QUantum Interference Device) to amplify the displacements of the proof mass away from equilibrium.

Like the accelerometers in the gravity gradiometer, the superconducting proof mass in the six-axis accelerometer (SSA) is free to respond to acceleration. However, the proof mass in this case is free to respond to accelerations in all six degrees of freedom. In the accelerometers in the gravity gradiometer, the proof mass position is confined by a mechanical spring and the accelerometer responds to acceleration in inverse proportion to the stiffness of this mechanical spring. In the six axis accelerometer, the proof mass is surrounded by quantized magnetic flux which confines the motion. Each degree of

freedom responds to acceleration in inverse proportion to the stiffness of a "magnetic spring".

These "magnetic springs" are generated by the superconducting coils placed in close proximity to the proof mass. The niobium proof mass excludes the magnetic flux from these coils due to the Meissner effect and any motion of the proof mass forces flux to redistribute itself within the superconducting circuitry. This transfer of energy produces a restoring force which opposes this change and creates the electrical equivalent to a mechanical spring.

Each degree of freedom in the SSA is confined and controlled by an independent superconducting circuit made up of four levitation coils. The stiffness in each degree of freedom is controlled by these circuits. The three circuits which control the linear degrees of freedom, provide the levitation force necessary to suspend the proof mass against the pull of gravity. The three remaining circuits provide feedback control for the angular degrees of freedom. In all, twenty-four levitation inductances surround the proof mass.

An additional twenty-four sensing inductances surround the proof mass, and are used to detect the motion of the proof mass. When acceleration is applied to the SSA, the proof mass is displaced in inverse proportion to the stiffness of the "magnetic" springs which surround the proof mass. Detection of this displacement is possible since the Meissner effect forces the inductance of the sensing coils to change in proportion to the displacement of the proof mass. Each degree of freedom is monitored by four sensing coils connected together to form a superconducting bridge circuit. The sensing coils which make up each bridge circuit are properly selected so that the output of each bridge is dependent on only one degree of freedom. The outputs of all the bridge circuits are connected in series to a SQUID amplifier, which converts this signal to an output voltage. Each bridge is driven by an independent oscillating current, and a misbalance of any one of the bridge circuits will appear at the output of the SQUID amplifier. Recovery of the original displacement of the proof mass in each degree of freedom is accomplished through the use of six lock-in amplifiers, each independently tuned to the correct carrier frequency.

A simplified version of this detection technique is shown in Fig. 2.1, for an accelerometer with one degree of freedom. As the proof mass is displaced from equilibrium in the positive x direction, the sensing inductances L_2 and L_4 decrease and the sensing inductances L_1 and L_3 increase. This change in sensing inductance unbalances

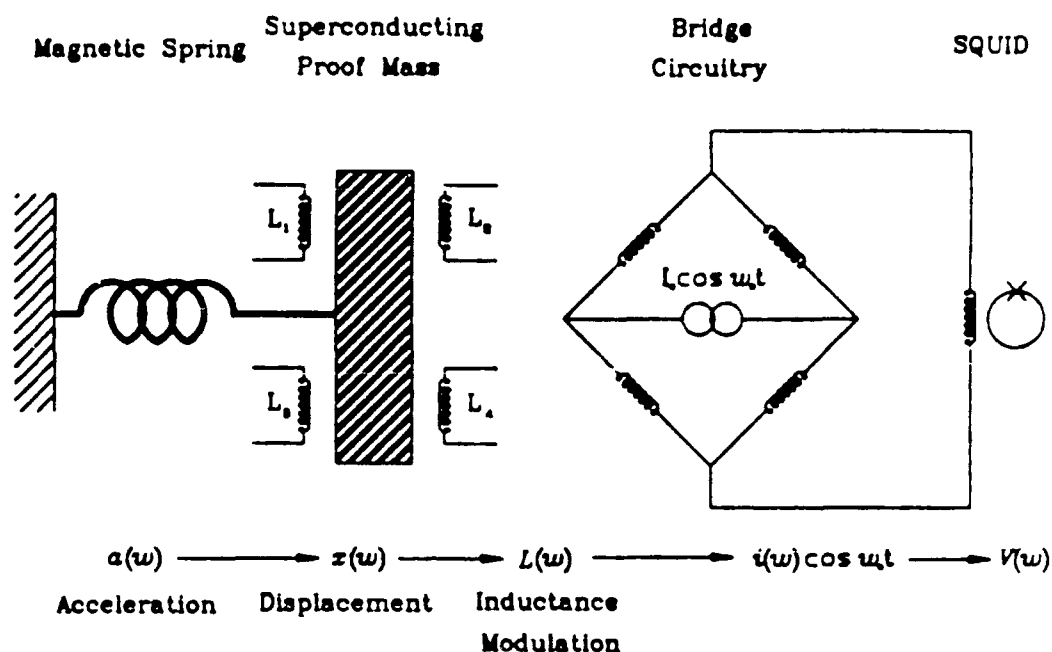


Figure 2.1. A schematic illustrating the principle of a superconducting bridge acceleration transducer.

the bridge circuit and an oscillating current proportional in amplitude to the misbalance appears across the output coil. This current is then amplified and converted to an output voltage through the use of a SQUID amplifier. Demodulation through the use of a lock-in amplifier then recovers the original misbalance signal.

In this section, we have presented a very brief description of the operation of the SSA. In the rest of this chapter, we will expand upon this description. We will first present a general description of the dynamical equations of the accelerometer. This will be followed by a description and analysis of the levitation and sensing circuitry. We will then combine this analysis and derive the transfer functions for the SSA which relate the external acceleration of the housing to the output. In the final section, we discuss the potential sensitivity of the SSA. Throughout this chapter, unless otherwise stated, we will employ summation notation, where any two like indices will denote a sum over each of the three axes, x , y , and z .

2.2 Dynamics of a Superconducting Six-Axis Accelerometer

An accelerometer must measure the acceleration of itself relative to an inertial reference frame. In a six-axis accelerometer, it is necessary to simultaneously measure the three linear and the three angular accelerations applied to the accelerometer. In actuality, the position and orientation of the proof mass is measured relative to the accelerometer housing, and the acceleration of the proof mass housing is inferred from the dynamics of the proof mass. Thus, it is necessary to clearly understand how the dynamics of the accelerometer can be used to derive the applied acceleration from a knowledge of the position and orientation of the proof mass.

In an accelerometer with only one degree of freedom, the equation of motion that relates the acceleration of the accelerometer housing to the position of the proof mass is relatively simple. In the SSA, it is necessary to contend with both the linear and angular degrees of freedom. This additional angular freedom complicates the description greatly and we will first consider the dynamics of a single-axis accelerometer.

We will then derive the dynamical equations for a rigid body in rotating, accelerated reference frame, i.e., the dynamical equations of the proof mass relative to the accelerometer housing which is rotating and accelerated. These dynamical equations will consist of three linear equations of motion and three Euler equations. The three linear equations will directly relate the measurement of the position of the proof mass to the acceleration of the accelerometer housing. The three angular equations will be more complicated. Euler's equations provide a description of the angular acceleration of a body. It will be necessary to parametrize the orientation of the proof mass in terms of a particular set of angles, and combine the kinematic equations with the dynamical equations to derive a set of angular equations of motion that relate the orientation of the proof mass to the angular accelerations of the proof mass housing.

2.2.1 Dynamics of a Single-Axis Accelerometer in a Rotating, Accelerated Reference Frame

In this section, we will be concerned with two reference frames: the reference frame attached to the accelerometer housing from which the proof mass position is

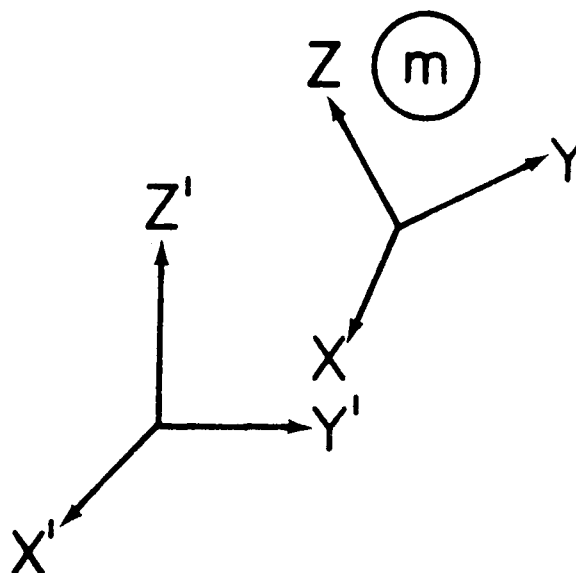


Figure 2.2. The single-axis accelerometer proof mass coordinate frame.

measured, and an inertial reference frame in which the accelerometer housing is rotating and accelerating. In order to derive Lagrange's equations, we will work in component notation. This is not as elegant as working in vector notation, but it is powerful. After we have derived Lagrange's equations, we can return to the elegance of vector notation.

The proof mass of a single-axis accelerometer is shown schematically in Fig. 2.2. The unprimed coordinates are taken as fixed to the accelerometer housing, and the primed coordinates are fixed to an inertial reference frame. The coordinates of the center of mass of the proof mass in the inertial reference frame are defined by

$$x'_i = R_{ik}^H r_k^P + r_i^H, \quad (2.1)$$

where R^H is the rotation matrix describing the orientation of the accelerometer housing with respect to the inertial reference frame, \mathbf{r}^H is the position of the accelerometer housing in the inertial reference frame, and \mathbf{r}^P is the position of the proof mass body relative to the accelerometer housing.

In order to formulate the dynamics of the accelerometer, we must compute the velocity of the proof mass in the inertial reference frame. This is a function of R^H , \mathbf{r}^H , and \mathbf{r}^P . Once we know this velocity, we can write down the Lagrangian for the

accelerometer and solve for the equations of motion. Differentiating Eq. (2.1) with respect to time gives the components of the velocity of the center of mass in the inertial reference frame,

$$\mathbf{v}'_i = \dot{R}_{ik}^H \mathbf{r}_k^P + R_{ik}^H \dot{\mathbf{r}}_k^P + \dot{\mathbf{r}}_i^H. \quad (2.2)$$

This can be written in the standard way by grouping terms so that all constituent components can be viewed in the inertial reference frame. We have

$$\mathbf{v}'_i = \dot{R}_{ik}^H R_{kj}^{H^{-1}} R_{jl}^H \mathbf{r}_l^P + R_{ik}^H \dot{\mathbf{r}}_k^P + \dot{\mathbf{r}}_i^H. \quad (2.3)$$

The second term in this equation is the velocity of the proof mass relative to the housing as viewed in the inertial reference frame, and the third term is just the velocity of the housing. The first term is the product of two terms: the first, $\dot{R}_{ik}^H R_{kj}^{H^{-1}}$, is related to the angular velocity of the housing, and the second, $R_{jl}^H \mathbf{r}_l^P$, is just the position of the proof mass relative to the housing as seen in the inertial reference frame. From Eq. (2.3) we see that $\dot{R}_{ik}^H R_{kj}^{H^{-1}}$ maps the position of the proof mass in the rotating frame into its velocity as seen from the inertial reference frame. Furthermore, $\dot{R}_{ik}^H R_{kj}^{H^{-1}}$ is antisymmetric and related to the components of angular velocity, $\boldsymbol{\omega}$. In the inertial reference frame, the components of $\boldsymbol{\omega}$ satisfy the equation [5]:

$$\dot{R}_{ij}^H R_{jk}^{H^{-1}} = \omega'_j \epsilon_{ijk}. \quad (2.4)$$

This is the usual $\boldsymbol{\omega}$. Substituting Eq. (2.4) into Eq. (2.3), we have

$$\mathbf{v}'_i = \omega'_j \epsilon_{ijk} R_{kl}^H \mathbf{r}_l^P + R_{ik}^H \dot{\mathbf{r}}_k^P + \dot{\mathbf{r}}_i^H. \quad (2.5)$$

We may now rewrite this in vector notation:

$$\mathbf{v}' = \boldsymbol{\omega} \times \mathbf{r}^P + \mathbf{v}^P + \mathbf{v}^H, \quad (2.6)$$

where \mathbf{v}^P is the velocity of the proof mass relative to the housing, and \mathbf{v}^H is the velocity of the housing. We have derived this standard result from a component formalism. This is the same technique we will use to derive Lagrange's equations of motion.

The Lagrangian for the dynamics of an accelerometer in a rotating, accelerated reference frame is

$$\mathcal{L} = \frac{1}{2} m \mathbf{v}' \cdot \mathbf{v}' - V(\mathbf{r}^P) - m \Phi_E(\mathbf{x}'). \quad (2.7)$$

where $V(\mathbf{r}^P)$ is the potential energy internal to the accelerometer, and $\Phi_E(\mathbf{x}')$ is the gravitational potential energy. The internal potential energy, V , includes the energy of the mechanical spring and the electromagnetic energy of the superconducting circuitry.

The generalized linear momentum from this Lagrangian, as measured with respect to the accelerometer housing, is

$$p_k \equiv \frac{\partial \mathcal{L}}{\partial \dot{r}_k^P} = m \frac{\partial v_j'}{\partial \dot{r}_k^P} v_j' = m R_{jk}^H \left(\dot{R}_{jl}^H r_l^P + R_{jl}^H \dot{r}_l^P + \dot{r}_j^H \right). \quad (2.8)$$

The generalized force, as measured with respect to the experimental housing, is

$$\begin{aligned} f_k &\equiv \frac{\partial \mathcal{L}}{\partial r_k^P} \\ &= m \frac{\partial v_j'}{\partial r_k^P} v_j' - m \frac{\partial \Phi_E(\mathbf{x}')}{\partial x_i'} \frac{\partial x_i'}{\partial r_k^P} - \frac{\partial V(\mathbf{r}^P)}{\partial r_k^P} \\ &= m \dot{R}_{jk}^H \left(\dot{R}_{jl}^H r_l^P + R_{jl}^H \dot{r}_l^P + \dot{r}_j^H \right) - m R_{ik}^H \frac{\partial \Phi_E(\mathbf{x}')}{\partial x_i'} - \frac{\partial V(\mathbf{r}^P)}{\partial r_k^P}. \end{aligned} \quad (2.9)$$

The time derivative of the generalized linear momentum can now be computed:

$$\begin{aligned} \frac{d}{dt} p_k &\equiv \frac{d}{dt} \frac{\partial \mathcal{L}}{\partial \dot{r}_k^P} = m \dot{R}_{jk}^H \left(\dot{R}_{jl}^H r_l^P + R_{jl}^H \dot{r}_l^P + \dot{r}_j^H \right) \\ &\quad + m R_{jk}^H \left(\ddot{R}_{jl}^H r_l^P + 2 \dot{R}_{jl}^H \dot{r}_l^P + R_{jl}^H \ddot{r}_l^P + \ddot{r}_j^H \right). \end{aligned} \quad (2.10)$$

Lagrange's equation sets the generalized force equal to the time rate of change of the generalized momentum:

$$R_{jk}^H (\ddot{R}_{jl}^H r_l^P + 2 \dot{R}_{jl}^H \dot{r}_l^P + R_{jl}^H \ddot{r}_l^P + \ddot{r}_j^H) = - R_{jk}^H \frac{\partial \Phi_E(\mathbf{x}')}{\partial x_j'} - \frac{1}{m} \frac{\partial V(\mathbf{r}^P)}{\partial r_k^P}. \quad (2.11)$$

Using the fact that \mathbf{R}^H is orthogonal, $R_{jk}^H = R_{kj}^{H-1}$, and rearranging terms gives

$$\ddot{\mathbf{r}}_k^P + \frac{1}{m} \frac{\partial V(\mathbf{r}^P)}{\partial \mathbf{r}_k^P} = \mathbf{a}_k^E, \quad (2.12)$$

where \mathbf{a}^E is the external acceleration applied to the accelerometer:

$$\mathbf{a}_k^E = - R_{kj}^{H-1} \left(\ddot{r}_j^H + 2 \dot{R}_{jl}^H \dot{r}_l^P + \ddot{R}_{jl}^H r_l^P + \frac{\partial \Phi_E(\mathbf{x}')}{\partial x_j'} \right). \quad (2.13)$$

The external acceleration applied to the accelerometer, \mathbf{a}^E , can be written:

$$\mathbf{a}_k^E \equiv -R_{kj}^{H^{-1}} \left(\ddot{\mathbf{r}}_j^H + \frac{\partial \Phi_E(\mathbf{x}')}{\partial \mathbf{x}'_j} \right) - 2R_{kj}^{H^{-1}} \dot{R}_{jl}^H \dot{\mathbf{r}}_l^P - R_{kj}^{H^{-1}} \ddot{R}_{jl}^H \mathbf{r}_l^P. \quad (2.14)$$

This can be written more clearly in terms of the angular velocity of the housing, $\boldsymbol{\omega}$. We have already seen the components of $\boldsymbol{\omega}$ in the inertial reference frame, Eq. (2.4). The components of $\boldsymbol{\omega}$, as viewed from the rotating housing, are defined as

$$\omega_i \equiv R_{il}^{H^{-1}} \omega'_l. \quad (2.15)$$

In analogy to Eq. (2.4), we find that

$$R_{kj}^{H^{-1}} \dot{R}_{jl}^H = \omega_j \epsilon_{kjl}. \quad (2.16)$$

$R^{H^{-1}} \ddot{R}^H$ can similarly be replaced. By differentiating Eq. (2.16) with respect to time and applying Eq. (2.16) to the result, we find

$$R_{kj}^{H^{-1}} \ddot{R}_{jl}^H = \omega_i \omega_j \epsilon_{kjm} \epsilon_{mil} + \dot{\omega}_i \epsilon_{kil}. \quad (2.17)$$

Substituting Eqs. (2.16) and (2.17) into Eq. (2.14), we find

$$\mathbf{a}_k^E \equiv -R_{kj}^{H^{-1}} \left(\ddot{\mathbf{r}}_j^H + \frac{\partial \Phi_E(\mathbf{x}')}{\partial \mathbf{x}'_j} \right) - 2\omega_j \dot{\mathbf{r}}_l^P \epsilon_{kjl} - \epsilon_{kjm} \omega_j \epsilon_{mil} \omega_i \mathbf{r}_l^P - \epsilon_{kjm} \dot{\omega}_i \mathbf{r}_l^P. \quad (2.18)$$

If we rewrite this in vectorial notation, the result is clear:

$$\mathbf{a}^E = -\ddot{\mathbf{r}}^H - \nabla \Phi_E - 2\boldsymbol{\omega} \times \dot{\mathbf{r}}^P - \boldsymbol{\omega} \times (\boldsymbol{\omega} \times \mathbf{r}^P) - \dot{\boldsymbol{\omega}} \times \mathbf{r}^P. \quad (2.19)$$

The first term of the right hand side is the acceleration of the housing, the second term is the gravitational acceleration, the third term is the Coriolis acceleration, the fourth term is the centrifugal acceleration, and the fifth and final term couples the angular acceleration to the linear acceleration in proportion to the displacement of the proof mass away from the center of the accelerometer housing.

2.2.2 Dynamics of a Rigid Body in a Rotating Accelerated Reference Frame

In the SSA, it is necessary to contend with both the linear and angular degrees of freedom. This additional angular freedom complicates the description greatly. We will

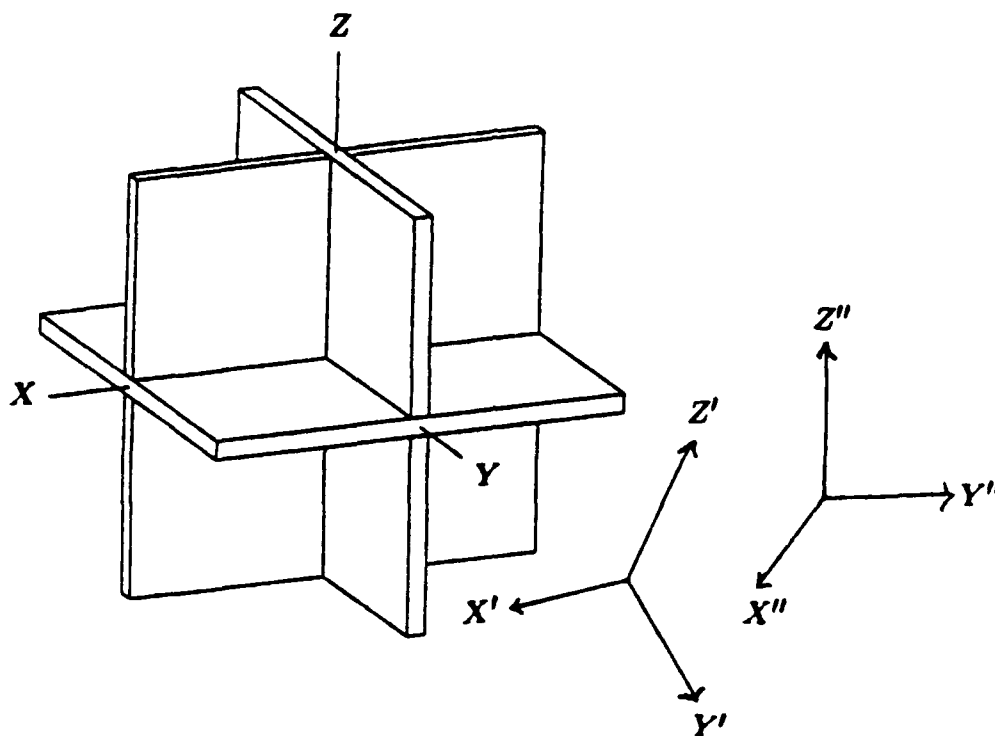


Figure 2.3. Schematic of the six-axis accelerometer proof mass.

be dealing with three specific reference frames: an inertial reference frame, a reference frame attached to the accelerometer housing, and a reference frame attached to the proof mass. Since all measurements of the position and orientation of the proof mass are made with respect to the accelerometer housing, we will derive all of our equations of motion with respect to that coordinate system.

We will begin the derivation of the dynamical equations by describing the position and orientation of the proof mass in terms of our three specific reference frames. After this is done, we will derive the linear and angular velocity of the proof mass in inertial space. This will allow us to construct the Lagrangian for SSA. After the Lagrangian is constructed, we will derive our linear and angular equations of motion.

The proof mass of the six-axis accelerometer is shown in Fig. 2.3. The unprimed coordinates are taken as fixed in the body of the proof mass, the primed coordinates are fixed to the accelerometer housing, and the double primed coordinates are fixed to an inertial reference frame.

In order to understand the dynamics of the proof mass, we begin by first relating

the components of a single point, P , as seen in the three coordinate systems. In the reference frame fixed to the proof mass, the coordinates of P are, by definition,

$$x_i. \quad (2.20)$$

This same point, as seen in the primed coordinate system attached to the accelerometer housing, has coordinates

$$x'_i = R_{ij}^P x_j + r_i^P, \quad (2.21)$$

where \mathbf{R}^P is the rotation matrix which describes the orientation of the proof mass with respect to the accelerometer housing, and \mathbf{r}^P is the displacement of the proof mass away from the center of the housing. The coordinates of P , as seen in the inertial reference frame, are

$$x''_i = R_{ij}^H x'_j + r_i^H = R_{ij}^H R_{jk}^P x_k + R_{ij}^H r_j^P + r_i^H, \quad (2.22)$$

where \mathbf{R}^H is the rotation matrix which describes the orientation of the housing of the accelerometer with respect to the inertial reference frame, and \mathbf{r}^H is the position of the housing in the inertial reference frame.

In order to construct the Lagrangian which describes the dynamics of the SSA, we must compute the angular velocity and the linear velocity of the proof mass relative to inertial space. This velocity will be a function of \mathbf{R}^P , \mathbf{R}^H , \mathbf{r}^P , and \mathbf{r}^H . Once this is done, we will be able to solve for the equations of motion.

We are free to choose the axes of the coordinate system fixed to the proof mass to lie along the principal body axes of the proof mass, and free to choose the center of mass to lie at the origin of this coordinate system. Thus the coordinates of the center of mass in the inertial reference frame are

$$x''_i = R_{ij}^H r_j^P + r_i^H, \quad (2.23)$$

where we have set $\mathbf{x} = 0$ in Eq. (2.22). This is exactly the same equation as in Section 2.2.1, where we described the dynamics of a single-axis accelerometer in a rotating accelerated reference frame. Following the same procedure as in Eqs. (2.1) through (2.5), the velocity of the center of mass of the proof mass is

$$v''_i = \omega_j^{H} \epsilon_{ijk} R_{kl}^H r_l^P + R_{ik}^H \dot{r}_k^P + \dot{r}_i^H, \quad (2.24)$$

where ω^H is the angular velocity of the housing in inertial space, and has components which satisfy the equation:

$$\dot{R}_{ij}^H R_{jk}^{H-1} = \omega_j''^H \epsilon_{ijk}. \quad (2.25)$$

We may now rewrite Eq. (2.24) in vector notation:

$$\mathbf{v}'' = \omega^H \times \mathbf{r}^P + \mathbf{v}^P + \mathbf{v}^H, \quad (2.26)$$

where \mathbf{v}^P is the velocity of the center of mass of the proof mass relative to the housing, and \mathbf{v}^H is the velocity of the housing.

Next, we must compute the angular velocity of the proof mass with respect to inertial space. In this case the displacements of the coordinate origins, \mathbf{r}^P and \mathbf{r}^H , do not affect the transformation of a vector. In fact, if \mathbf{f} is an arbitrary vector fixed to the accelerometer proof mass, then we may write

$$\mathbf{f}_i'' = R_{ij}^H R_{jk}^P \mathbf{f}_k. \quad (2.27)$$

Differentiating this vector with respect to time must give us the angular velocity. We find

$$\dot{\mathbf{f}}_i'' = \dot{R}_{ij}^H R_{jk}^P \mathbf{f}_k + R_{ij}^H \dot{R}_{jk}^P \mathbf{f}_k, \quad (2.28)$$

and this may be rewritten:

$$\dot{\mathbf{f}}_i'' = \dot{R}_{ij}^H R_{jl}^{H-1} R_{lm}^H R_{mk}^P \mathbf{f}_k + R_{ij}^H \dot{R}_{jr}^P R_{rk}^{P-1} R_{kl}^{H-1} R_{lp}^H R_{pq}^P \mathbf{f}_q. \quad (2.29)$$

Substituting Eq. (2.27), we find

$$\dot{\mathbf{f}}_i'' = \left(\dot{R}_{ij}^H R_{jl}^{H-1} + R_{ij}^H \dot{R}_{jr}^P R_{rk}^{P-1} R_{kl}^{H-1} \right) \mathbf{f}_l''. \quad (2.30)$$

Because \mathbf{f} is a vector fixed to the accelerometer proof mass, its time derivative must obey the equation

$$\dot{\mathbf{f}}_i'' = \epsilon_{ijl} \omega_j'' \mathbf{f}_l''. \quad (2.31)$$

Identifying the two coefficients of \mathbf{f}_l'' in Eqs. (2.30) and (2.31), we have

$$\epsilon_{ijl} \omega_j'' = \dot{R}_{ij}^H R_{jl}^{H-1} + R_{ij}^H \dot{R}_{jr}^P R_{rk}^{P-1} R_{kl}^{H-1}. \quad (2.32)$$

The first term on the right hand side of this equation is, from Eq. (2.4),

$$\dot{R}_{ij}^H R_{jl}^{H-1} = \omega_j''^H \epsilon_{ijl}. \quad (2.33)$$

The second term on the right hand side of Eq. (2.32) is more complicated. The two middle factors, $\dot{\mathbf{R}}^P \mathbf{R}^{P-1}$, can be written, from Eq. (2.4):

$$\dot{R}_{jr}^P R_{rk}^{P-1} = \omega_r'^P \epsilon_{jrk}. \quad (2.34)$$

Substituting these two results into the equation for the angular velocity of the proof mass, we find

$$\epsilon_{ijl} \omega_j'' = \epsilon_{ijl} \omega_j''^H + R_{ij}^H \epsilon_{jrk} \omega_r'^P R_{kl}^{H-1}. \quad (2.35)$$

Recognizing that the components of the Levi-Civita tensor must remain the same in all Cartesian coordinate systems, this can be written:

$$\epsilon_{ijl} \omega_j'' = (\omega_j''^H + R_{jk}^H \omega_k'^P) \epsilon_{ijl}. \quad (2.36)$$

Thus, the components of the angular velocity of the proof mass, ω , are

$$\omega_j'' = \omega_j''^H + R_{jk}^H \omega_k'^P, \quad (2.37)$$

where ω^H is the angular velocity of the accelerometer housing, and $\mathbf{R}^H \omega^P$ is the angular velocity of the proof mass with respect to the housing, as seen in the inertial reference frame.

We can now compute the Lagrangian for the six-axis accelerometer:

$$\mathcal{L} = \frac{1}{2} m \mathbf{v}'' \cdot \mathbf{v}'' + \frac{1}{2} \mathbf{w} \cdot \mathbf{I} \cdot \mathbf{w} - V(\mathbf{R}^P, \mathbf{r}^P) - m \phi(\mathbf{x}''), \quad (2.38)$$

where $V(\mathbf{R}^P, \mathbf{r}^P)$ is the potential energy internal to the accelerometer, $\phi(\mathbf{x}'')$ is the gravitational potential energy of the proof mass, m is the mass of the proof mass, and \mathbf{I} is the moment of inertia tensor for the proof mass. The internal potential energy, V , includes the electromagnetic energy of the superconducting circuitry.

Linear Dynamical Equations

We first compute the dynamical equations for the linear degrees of freedom. The generalized linear momentum from the SSA Lagrangian, as measured with respect to the accelerometer housing, is

$$p_k'^P \equiv \frac{\partial \mathcal{L}}{\partial \dot{r}_k^P} = m \frac{\partial v_j''}{\partial \dot{r}_k^P} v_j'' = m R_{jk}^H \left(\dot{R}_{jl}^H r_l^P + R_{jl}^H \dot{r}_l^P + \dot{r}_j^H \right). \quad (2.39)$$

The generalized linear force, as measured with respect to the accelerometer housing, is

$$\begin{aligned}
 f_k^P &\equiv \frac{\partial \mathcal{L}}{\partial r_k^P} \\
 &= m \frac{\partial v_j''}{\partial r_k^P} v_j'' - m \frac{\partial \Phi_E(x'')}{\partial x_i''} \frac{\partial x_i''}{\partial r_k^P} - \frac{\partial V(\mathbf{R}^P, \mathbf{r}^P)}{\partial r_k^P} \\
 &= m \dot{R}_{jk}^H \left(\dot{R}_{jl}^H r_l^P + R_{jl}^H \dot{r}_l^P + \dot{r}_j^H \right) - m R_{ik}^H \frac{\partial \Phi_E(x'')}{\partial x_i''} - \frac{\partial V(\mathbf{R}^P, \mathbf{r}^P)}{\partial r_k^P}. \quad (2.40)
 \end{aligned}$$

This analysis is identical to that in Section 2.2.1. Setting the time derivative of the generalized momenta equal to the generalized force, and following the same analysis as in Eqs. (2.3) through (2.8), we find

$$\ddot{r}_k^P + \frac{1}{m} \frac{\partial V(\mathbf{R}^P, \mathbf{r}^P)}{\partial r_k^P} = a_k^E, \quad (2.41)$$

where \mathbf{a}^E is the external acceleration applied to the accelerometer:

$$a_k^E \equiv -R_{kj}^{H^{-1}} \left(\ddot{r}_j^H + \frac{\partial \Phi_E(x'')}{\partial x_j''} \right) - 2\omega_j'^H \dot{r}_l^P \epsilon_{kjl} - \epsilon_{kjm} \omega_j'^H \epsilon_{mil} \omega_i'^H r_l^P - \epsilon_{kjm} \dot{\omega}_i'^H r_l^P, \quad (2.42)$$

where $\omega_i'^H \equiv R_{il}^{H^{-1}} \omega_l''^H$ are the components of the angular velocity of the housing, as viewed from the rotating housing. If we rewrite this in vectorial notation, the result is clear:

$$\mathbf{a}^E = -\ddot{\mathbf{r}}^H - \nabla \Phi_E - 2\boldsymbol{\omega}^H \times \dot{\mathbf{r}}^P - \boldsymbol{\omega}^H \times (\boldsymbol{\omega}^H \times \mathbf{r}^P) - \dot{\boldsymbol{\omega}}^H \times \mathbf{r}^P. \quad (2.43)$$

This result is identical to Eq. (2.19). The first term of the right hand side is the acceleration of the housing, the second term is the gravitational acceleration, the third term is the Coriolis acceleration, the fourth term is the centrifugal acceleration, the fifth and final term couples the angular acceleration to the linear acceleration in proportion to the displacement of the proof mass away from the center of the housing. This equation forms the cornerstone for an understanding of the linear acceleration of the center of mass of the six-axis accelerometer.

Angular Dynamical Equations

The angular equations of motion can now be computed. In order to correctly compute these equations, we must incorporate six constraint equations that insure that

the state variables, R_{ij}^P , are varied in such a way that the matrix \mathbf{R}^P remains an orthogonal transformation. We can do this by using the method of Lagrange multipliers, whereby we add our constraint equations to the Lagrangian. We find

$$\mathcal{L} = \frac{1}{2} m \mathbf{v}'' \cdot \mathbf{v}'' + \frac{1}{2} \boldsymbol{\omega} \cdot \mathbf{I} \cdot \boldsymbol{\omega} - V(\mathbf{R}^P, \mathbf{r}^P) - m\phi(\mathbf{x}'') + \lambda_{lm} (R_{lp}^P R_{mp}^P - \delta_{lm}), \quad (2.44)$$

where λ_{lm} is symmetric. This will insure that the matrix \mathbf{R}^P remains orthogonal, i.e.,

$$R_{lp}^P R_{mp}^P - \delta_{lm} = 0. \quad (2.45)$$

The generalized angular momentum from this Lagrangian can now be computed:

$$\begin{aligned} P_{ij}^{'P} &\equiv \frac{\partial \mathcal{L}}{\partial \dot{R}_{ij}^P} = \frac{\partial \omega''_k}{\partial \dot{R}_{ij}^P} I''_{kq} \omega''_q = R_{kl}^H \frac{\partial \omega'^P_l}{\partial \dot{R}_{ij}^P} I''_{lq} (\omega''^H_q + R_{qv}^H \omega'^P_v) \\ &= \frac{\partial \omega'^P_l}{\partial \dot{R}_{ij}^P} I'_{lq} (\omega'^H_q + \omega'^P_q), \end{aligned} \quad (2.46)$$

where we have made the substitution

$$I'_{lq} \equiv R_{lv}^{H^{-1}} I''_{vw} R_{wq}^H, \quad (2.47)$$

for the components of the moment of inertia tensor, \mathbf{I} , as seen in the reference frame of the accelerometer housing, and made the substitution

$$\omega'^H_q = R_{qv}^{H^{-1}} \omega''^H_v, \quad (2.48)$$

for the components of the angular velocity of the housing, as seen in the reference frame of the rotating housing.

The generalized angular forces can similarly be computed:

$$\begin{aligned} N_{ij}^{'P} &\equiv \frac{\partial \mathcal{L}}{\partial R_{ij}^P} \\ &= \frac{\partial \omega''_k}{\partial R_{ij}^P} I''_{kq} \omega''_q - \frac{\partial V(\mathbf{R}^P, \mathbf{r}^P)}{\partial R_{ij}^P} + \lambda_{im} R_{mj}^P + \lambda_{li} R_{lj}^P + \frac{1}{2} \omega''_k \frac{\partial I''_{kq}}{\partial R_{ij}^P} \omega''_q \\ &= \frac{\partial \omega'^P_i}{\partial R_{ij}^P} I'_{lq} (\omega'^H_q + \omega'^P_q) - \frac{\partial V(\mathbf{R}^P, \mathbf{r}^P)}{\partial R_{ij}^P} + 2\lambda_{im} R_{mj}^P + \omega_m I_{mj} \omega'_i. \end{aligned} \quad (2.49)$$

where we have used the symmetry of λ , and made the same substitution for the components of \mathbf{I} and $\boldsymbol{\omega}^H$.

The partial derivatives of ω^P can be computed by recognizing (from Eq. (2.34)) that ω^P is the dual of $\dot{\mathbf{R}}^P \mathbf{R}^{P-1}$, i.e.,

$$\omega_l^P = \frac{1}{2} \epsilon_{lpm} \dot{R}_{mn}^P R_{pn}^P. \quad (2.50)$$

The partial derivatives can now be computed:

$$\frac{\partial \omega_l^P}{\partial R_{ij}^P} = \frac{1}{2} \epsilon_{lim} \dot{R}_{mj}^P, \quad (2.51)$$

$$\frac{\partial \omega_l^P}{\partial \dot{R}_{ij}^P} = -\frac{1}{2} \epsilon_{lim} R_{mj}^P. \quad (2.52)$$

Substituting these expressions into the equations for \mathbf{N} and \mathbf{P} gives

$$N_{ij}^{'P} \equiv \frac{1}{2} \epsilon_{lim} \dot{R}_{mj}^P I'_{lq} (\omega_q^H + \omega_q^P) - \frac{\partial V(\mathbf{R}^P, \mathbf{r}^P)}{\partial R_{ij}^P} + 2\lambda_{im} R_{mj}^P + \omega_m I_{mj} \omega'_i, \quad (2.53)$$

$$P_{ij}^{'P} \equiv -\frac{1}{2} \epsilon_{lim} R_{mj}^P I'_{lq} (\omega_q^H + \omega_q^P). \quad (2.54)$$

The angular equations of motion can now be computed. Setting the time derivative of the generalized momenta equal to the generalized force gives

$$\begin{aligned} \frac{1}{2} \epsilon_{lim} R_{mj}^P I'_{lq} (\dot{\omega}_q^H + \dot{\omega}_q^P) = \\ \epsilon_{lim} \dot{R}_{mj}^P I'_{lq} (\omega_q^H + \omega_q^P) - \frac{\partial V(\mathbf{R}^P, \mathbf{r}^P)}{\partial R_{ij}^P} + 2\lambda_{im} R_{mj}^P \\ + \frac{1}{2} \epsilon_{lim} R_{mj}^P \dot{I}'_{lq} (\omega_q^H + \omega_q^P) + \omega_m I_{mj} \omega'_i. \end{aligned} \quad (2.55)$$

Lagrange's equations can be simplified by multiplying both sides by \mathbf{R}^{P-1} , and substituting Eq. (2.34) into the result. We find

$$\begin{aligned} \frac{1}{2} \epsilon_{lij} I'_{lq} (\dot{\omega}_q^H + \dot{\omega}_q^P) = \\ \epsilon_{lim} \epsilon_{mu j} \omega_u^{'P} I'_{lq} (\omega_q^H + \omega_q^P) - R_{ju}^P \frac{\partial V(\mathbf{R}^P, \mathbf{r}^P)}{\partial R_{iu}^P} + 2\lambda_{ij} + \omega'_m I'_{mj} \omega'_i \\ + \frac{1}{2} \epsilon_{lij} \dot{I}'_{lq} (\omega_q^H + \omega_q^P). \end{aligned} \quad (2.56)$$

This can be further simplified by making the substitution:

$$\dot{I}'_{lq} = \omega_m^{'P} \epsilon_{lmn} I'_{nq} + \epsilon_{qmn} I'_{ln} \omega'_m, \quad (2.57)$$

and applying the identity:

$$\epsilon_{ilm}\epsilon_{ujm} = \delta_{lu}\delta_{ij} - \delta_{lj}\delta_{iu}. \quad (2.58)$$

We find

$$\begin{aligned} \frac{1}{2}\epsilon_{lij}I'_{lq}(\dot{\omega}'^H_q + \dot{\omega}'^P_q) = \\ \delta_{ij}\omega'^P_l I'_{lq}(\omega'^H_q + \omega'^P_q) + \omega'^P_i I'_{jq}(\omega'^H_q + \omega'^P_q) - R^P_{ju} \frac{\partial V(\mathbf{R}^P, \mathbf{r}^P)}{\partial R^P_{iu}} + 2\lambda_{ij} \\ + \frac{1}{2}\omega'^P_i I'_{jq}\omega'_q - \frac{1}{2}\omega'^P_j I'_{iq}\omega'_q + \frac{1}{2}\epsilon_{lij}I'_{lc}\epsilon_{cqm}\omega'^P_m\omega'^H_q. \end{aligned} \quad (2.59)$$

This set of nine equations can be viewed as a 3x3 matrix of equations. These equations contain the six forces of constraint, λ_{ij} , that force the components of \mathbf{R}^P to satisfy the condition that \mathbf{R}^P be an orthogonal transformation. They can be eliminated by separating the symmetric and antisymmetric portions of our matrix of equations. This will leave us with six equations which contain the constraints, and three equations which do not. We find, for the symmetric part of our matrix of equations,

$$\begin{aligned} 2\lambda_{ij} = & -\delta_{ij}\omega'^P_l I'_{lq}(\omega'^H_q + \omega'^P_q) - \frac{1}{2}(\omega'^P_i I'_{jq} + \omega'^P_j I'_{iq})(\omega'^H_q + \omega'^P_q) \\ & + \frac{1}{2}\left[R^P_{ju} \frac{\partial V(\mathbf{R}^P, \mathbf{r}^P)}{\partial R^P_{iu}} + R^P_{iu} \frac{\partial V(\mathbf{R}^P, \mathbf{r}^P)}{\partial R^P_{ju}}\right]. \end{aligned} \quad (2.60)$$

These equations give us the forces of constraint.

Substituting these forces back into our nine equations of motion eliminates the symmetric part of the matrix of equations. Taking the dual of our matrix of equations leaves us with the antisymmetric portion:

$$\begin{aligned} \epsilon_{kij}\frac{1}{2}\epsilon_{lij}I'_{lq}(\dot{\omega}'^H_q + \dot{\omega}'^P_q) = & \epsilon_{kij}\delta_{lj}\omega'^P_l I'_{lq}(\omega'^H_q + \omega'^P_q) + 2\epsilon_{kij}\lambda_{ij} \\ & + 2\epsilon_{kij}\omega'^P_i I'_{jq}\omega'_q - I'_{ik}\epsilon_{cjm}\omega'^P_m\omega'^H_q \\ & - \epsilon_{kij}R^P_{ju} \frac{\partial V(\mathbf{R}^P, \mathbf{r}^P)}{\partial R^P_{iu}}. \end{aligned} \quad (2.61)$$

This can be simplified by using the identity in Eq. (2.58), and dropping all symmetric terms. We find

$$I'_{kq}\dot{\omega}'^P_q = -I'_{kq}\dot{\omega}'^H_q - 2\epsilon_{kij}\omega'^P_i I'_{jq}\omega'_q + I'_{kq}\epsilon_{qij}\omega'^P_i\omega'^H_j + \epsilon_{kij}R^P_{ju} \frac{\partial V(\mathbf{R}^P, \mathbf{r}^P)}{\partial R^P_{iu}}. \quad (2.62)$$

These are Euler's equations in the reference frame of the accelerometer housing.

The last term on the right hand side of this equation is the applied torque from the coils surrounding the proof mass, i.e.,

$$T'_k \equiv \epsilon_{kij} R_{ju}^P \frac{\partial V(\mathbf{R}^P, \mathbf{r}^P)}{\partial R_{iu}^P} . \quad (2.63)$$

To see this more clearly, we will reduce the problem to two dimensions, and force all rotations to take place in the x - y plane. We can then define

$$\mathbf{R}^P \equiv e^{\theta} \mathbf{J}^3 , \quad (2.64)$$

where \mathbf{J}^3 is the generator of rotations about the z axis, and has components $J_{ij}^3 = -\epsilon_{ij3}$. In this two-dimensional simplification, $V(\mathbf{R}^P, \mathbf{r}^P)$ can only be a function of θ . The torque generated by the potential V is

$$T'_3 = - \frac{\partial V}{\partial \theta} . \quad (2.65)$$

We can rewrite this, using the chain rule of calculus:

$$\begin{aligned} T'_3 &= - \frac{\partial V}{\partial \theta} = - \frac{\partial V}{\partial R_{k_2}^P} \frac{\partial R_{k_2}^P}{\partial \theta} \\ &= - \frac{\partial V}{\partial R_{k_2}^P} J_{km}^3 R_{mj}^P = \epsilon_{3ij} R_{ju}^P \frac{\partial V}{\partial R_{iu}^P} . \end{aligned} \quad (2.66)$$

Thus Euler's equation can be rewritten:

$$I'_{kq} \dot{\omega}'_q{}^P = -I'_{kq} \dot{\omega}'_q{}^H - 2\epsilon_{kij} \omega'_i{}^P I'_{jq} \omega'_q{}^H + I'_{kq} \epsilon_{qij} \omega'_i{}^P \omega'_j{}^H + T'_k . \quad (2.67)$$

The components of the moment of inertia tensor, \mathbf{I} , are known explicitly, only in the reference frame of the proof mass. Since we have chosen our axes to lie along the principal axes of the proof mass, \mathbf{I} is diagonal in this reference frame. If the proof mass of the accelerometer is completely symmetrical so that all three principal moments of inertia are equal, then the moment of inertia tensor will be diagonal in all rotated Cartesian coordinate systems. This allows us to simplify the right hand side of Euler's equations. If the proof mass was not completely symmetrical, then terms coupling the square of the angular momentum of the housing would introduce errors in the measurement of the

angular acceleration of the accelerometer housing. Setting $I'_{ij} = I\delta_{ij}$ in Eq. (2.67), we have

$$I\dot{\omega}'^P_k - T'_k = -I\dot{\omega}'^H_k - I\epsilon_{kij}\omega'^P_i\omega'^H_j. \quad (2.68)$$

This equation forms the cornerstone for an understanding of the detection of the angular acceleration of the housing with respect to inertial space.

2.2.3 Accelerometer Equations of Motion

We have now completed our description of the dynamics of the SSA. This description does not yet describe how a measurement of the orientation of the proof mass will allow us to measure the angular acceleration of the accelerometer housing. In order to complete this description, it is necessary to pick a particular set of angles with which to describe the orientation of the proof mass. This will then allow us to combine the kinematics of this description with Euler's equations, and derive explicit angular equations of motion which will directly relate the orientation of the proof mass to the angular acceleration of the accelerometer housing.

The detection of linear acceleration is, on the other hand, completely described by Eq. (2.41):

$$\ddot{r}^P_k + \frac{1}{m} \frac{\partial V(R^P, r^P)}{\partial r^P_k} = a^E_k. \quad (2.69)$$

where

$$\alpha^E = -\ddot{r}^H - \nabla\Phi_E - 2\omega^H \times \dot{r}^P - \omega^H \times (\omega^H \times r^P) - \dot{\omega}^H \times r^P. \quad (2.70)$$

The superconducting coils surrounding the proof mass generate the potential V . The position of the proof mass with respect to the housing is controlled by these coils. The coils are rigidly mounted to the housing of the accelerometer. Ideally, in an accelerometer, we demand that this applied, i.e., measured, acceleration is equal and opposite to the acceleration of the housing. It is clear from Eq. (2.70) that, in order to equate the linear acceleration of the housing to the linear acceleration of the proof mass, we must keep the displacement of the proof mass from the center of the housing, r^P , and the velocity of this displacement, \dot{r}^P , to a minimum.

This can be achieved by using force rebalance feedback. This type of feedback effectively stiffens the magnetic spring between the housing and the proof mass, and

at the same time dampens any oscillations. The applied feedback exactly cancels the acceleration of the housing and holds the proof mass at rest with respect to the housing. This forces \mathbf{r}^P and $\dot{\mathbf{r}}^P$ to vanish.

Although Eq. (2.68) completely describes the angular motion of the accelerometer, it is not clear how a measurement of the angular position of the proof mass describes the angular acceleration of the housing. The orientation of the proof mass of the SSA can be described by the rotation matrix \mathbf{R}^P , but such a description is not convenient. In order to explicitly describe the motion of the proof mass, it is necessary to parameterize the rotation matrix in terms of three angles. The usual choice is to describe \mathbf{R}^P in terms of the Euler angles. If we were to describe \mathbf{R}^P in terms of Euler angles, then we could write [5]

$$\mathbf{R}^P = e^{\phi \mathbf{J}^3} e^{\theta \mathbf{J}^2} e^{\psi \mathbf{J}^1}, \quad (2.71)$$

where \mathbf{J}^i , $i = 1, 2, 3$, are the generators of rotation about the i -th axis, and have components $J_{jk}^i = -\epsilon_{jki}$. The Euler parametrization of the rotation group has many advantages, but in examining Eq. (2.71), it is immediately apparent that, for small angles, there is no simple relationship between rotation about the x axis, and ϕ , θ , and ψ . Thus, we will instead choose the parameterization:

$$\mathbf{R}^P = e^{\theta_x \mathbf{J}^1} e^{\theta_y \mathbf{J}^2} e^{\theta_z \mathbf{J}^3}. \quad (2.72)$$

This places rotations about all three axes on roughly equal footing. Although the angles θ_x , θ_y , and θ_z do not exactly correspond to rotations about the x , y , and z axes of the accelerometer, for small angles this is a good approximation, and it makes the succeeding calculations more tractable. The fact that the three successive rotations do not commute will lead to equations with nonsymmetrical cross terms in the second and higher orders. However, it will be seen that these unsymmetrical terms eventually drop out. Expanding Eq. (2.72) into explicit matrix form, we find

$$\mathbf{R}^P = \begin{bmatrix} \cos\theta_y \cos\theta_z & -\cos\theta_y \sin\theta_z & \sin\theta_y \\ \cos\theta_x \sin\theta_z + \sin\theta_x \sin\theta_y \cos\theta_z & \cos\theta_x \cos\theta_z - \sin\theta_x \sin\theta_y \sin\theta_z & -\sin\theta_x \cos\theta_y \\ \sin\theta_x \sin\theta_z - \cos\theta_x \sin\theta_y \cos\theta_z & \cos\theta_x \sin\theta_y \sin\theta_z + \sin\theta_x \cos\theta_z & \cos\theta_x \cos\theta_y \end{bmatrix}. \quad (2.73)$$

Substituting \mathbf{R}^P into Eq. (2.50) and solving for ω^P , we find

$$\omega_1^P = \sin\theta_y \frac{d\theta_z}{dt} + \frac{d\theta_x}{dt}. \quad (2.74)$$

$$\omega_2^P = \cos \theta_x \frac{d\theta_y}{dt} - \sin \theta_x \cos \theta_y \frac{d\theta_z}{dt}, \quad (2.75)$$

$$\omega_3^P = \cos \theta_x \cos \theta_y \frac{d\theta_z}{dt} + \sin \theta_x \frac{d\theta_y}{dt}. \quad (2.76)$$

These equations relate the rate of change of our three angular coordinates to the angular velocity, ω^P .

In order to write Euler's equations explicitly in terms of θ_x , θ_y , and θ_z , the torque (Eq. (2.63)) applied by the superconducting coils surrounding the proof mass must be related to partial derivatives of the potential V with respect to θ . Once more utilizing the chain rule of calculus, we may write

$$\begin{aligned} -\frac{\partial V}{\partial \theta_x} &= -\frac{\partial V}{\partial R_{kj}^P} \frac{\partial R_{kj}^P}{\partial \theta_x} = -\frac{\partial V}{\partial R_{kj}^P} J_{km}^1 R_{mj}^P = \epsilon_{km1} \frac{\partial V}{\partial R_{kj}^P} R_{mj}^P \\ &= T_1', \end{aligned} \quad (2.77)$$

where we have substituted our parametrization for R^P . The partial derivative of the potential, V , with respect to θ_y and θ_z can similarly be computed:

$$\begin{aligned} -\frac{\partial V}{\partial \theta_y} &= -\frac{\partial V}{\partial R_{kj}^P} \frac{\partial R_{kj}^P}{\partial \theta_y} = -\frac{\partial V}{\partial R_{kj}^P} \left(e^{\theta_x J^1} J^2 e^{-\theta_x J^1} \right)_{km} R_{mj}^P \\ &= -\frac{\partial V}{\partial R_{kj}^P} \left(J^2 \cos \theta_x + J^3 \sin \theta_x \right)_{km} R_{mj}^P \\ &= T_2' \cos \theta_x + T_3' \sin \theta_x, \end{aligned} \quad (2.78)$$

$$\begin{aligned} -\frac{\partial V}{\partial \theta_z} &= -\frac{\partial V}{\partial R_{kj}^P} \frac{\partial R_{kj}^P}{\partial \theta_z} \\ &= -\frac{\partial V}{\partial R_{kj}^P} \left(e^{\theta_x J^1} e^{\theta_y J^2} J^3 e^{-\theta_y J^2} e^{-\theta_x J^1} \right)_{km} R_{mj}^P \\ &= -\frac{\partial V}{\partial R_{kj}^P} \left[e^{\theta_x J^1} \left(J^1 \sin \theta_y + J^3 \cos \theta_y \right) e^{-\theta_x J^1} \right]_{km} R_{mj}^P \\ &= -\frac{\partial V}{\partial R_{kj}^P} \left(J^1 \sin \theta_y - J^2 \sin \theta_x \cos \theta_y + J^3 \cos \theta_x \cos \theta_y \right)_{km} R_{mj}^P \\ &= \sin \theta_y T_1' - \sin \theta_x \cos \theta_y T_2' + \cos \theta_x \cos \theta_y T_3'. \end{aligned} \quad (2.79)$$

Solving Eqs. (2.77), (2.78), and (2.79) for T_1' , T_2' , and T_3' , we find

$$T_1' = -\frac{\partial V}{\partial \theta_x}, \quad (2.80)$$

$$T'_2 = -\cos\theta_x \frac{\partial V}{\partial\theta_y} + \frac{\sin\theta_x}{\cos\theta_y} \frac{\partial V}{\partial\theta_z} - \frac{\sin\theta_x \sin\theta_y}{\cos\theta_y} \frac{\partial V}{\partial\theta_x}, \quad (2.81)$$

$$T'_3 = -\frac{\cos\theta_x}{\cos\theta_y} \frac{\partial V}{\partial\theta_z} - \sin\theta_x \frac{\partial V}{\partial\theta_y} + \frac{\cos\theta_x \sin\theta_y}{\cos\theta_y} \frac{\partial V}{\partial\theta_x}. \quad (2.82)$$

This completes the parametrization of \mathbf{R}^P in terms of θ_x , θ_y , and θ_z .

We can now compute Euler's equations in terms of these angles. Substituting the expressions for T'_i and $\omega_i'^P$ into Eq. (2.68), and solving for $\ddot{\theta}_x$, $\ddot{\theta}_y$, and $\ddot{\theta}_z$, we find

$$\begin{aligned} \ddot{\theta}_x = & \cos\theta_x \tan\theta_y \dot{\omega}_3'^H - \sin\theta_x \tan\theta_y \dot{\omega}_2'^H - \dot{\omega}_1'^H \\ & + \frac{\omega_3'^H}{\cos\theta_y} (\sin\theta_x \dot{\theta}_z - \cos\theta_y \cos\theta_x \dot{\theta}_y + \sin\theta_x \sin\theta_y \dot{\theta}_x) \\ & + \frac{\omega_2'^H}{\cos\theta_y} (\cos\theta_x \dot{\theta}_z + \sin\theta_x \cos\theta_y \dot{\theta}_y + \cos\theta_x \sin\theta_y \dot{\theta}_x) - \frac{\omega_1'^H}{\cos\theta_y} \dot{\theta}_y \sin\theta_y \\ & - \frac{\dot{\theta}_y \dot{\theta}_z}{\cos\theta_y} + \frac{\dot{\theta}_x \dot{\theta}_y \sin\theta_y}{\cos\theta_y} + \frac{1}{I} \frac{\tan\theta_y}{\cos\theta_y} \frac{\partial V}{\partial\theta_z} - \frac{1}{I} \frac{1}{\cos^2\theta_y} \frac{\partial V}{\partial\theta_x}, \end{aligned} \quad (2.83)$$

$$\begin{aligned} \ddot{\theta}_y = & -\cos\theta_x \dot{\omega}_2'^H - \sin\theta_x \dot{\omega}_3'^H + (\omega_3'^H \cos\theta_x - \omega_2'^H \sin\theta_x) (\dot{\theta}_x + \sin\theta_y \dot{\theta}_z) \\ & - \omega_1'^H \cos\theta_y \dot{\theta}_z - \frac{1}{I} \frac{\partial V}{\partial\theta_y} + \dot{\theta}_x \dot{\theta}_z \cos\theta_y, \end{aligned} \quad (2.84)$$

$$\begin{aligned} \ddot{\theta}_z = & -\frac{\cos\theta_x}{\cos\theta_y} \dot{\omega}_3'^H + \frac{\sin\theta_x}{\cos\theta_y} \dot{\omega}_2'^H \\ & - (\omega_3'^H \sin\theta_x + \omega_2'^H \cos\theta_x) \frac{1}{\cos\theta_y} (\dot{\theta}_x + \sin\theta_y \dot{\theta}_z) + \frac{\omega_1'^H}{\cos\theta_y} \dot{\theta}_y \\ & - \frac{1}{I \cos^2\theta_y} \frac{\partial V}{\partial\theta_z} + \frac{\tan\theta_y}{I} \frac{\partial V}{\partial\theta_x} + \tan\theta_y \dot{\theta}_y \dot{\theta}_z - \frac{1}{\cos\theta_y} \dot{\theta}_x \dot{\theta}_y. \end{aligned} \quad (2.85)$$

Unlike the equations for the linear acceleration of the six-axis accelerometer, these equations which relate the acceleration of θ_x , θ_y , and θ_z to the angular acceleration of the accelerometer housing are highly nonlinear. This is not a difficulty, since the proof mass of the accelerometer is surrounded by superconducting coils which confine its motion and force all θ and $\dot{\theta}$ terms to be small. Thus we can linearize our equations of motion, and drop all second order terms. Expanding Eqs. (2.83), (2.84), and (2.85) to

first order, we find

$$\ddot{\theta}_x + \frac{1}{I} \frac{\partial V}{\partial \theta_x} = -\dot{\omega}_1^H + \theta_y \dot{\omega}_3^H - \omega_3^H \dot{\theta}_y + \omega_2^H \dot{\theta}_z + \frac{\theta_y}{I} \frac{\partial V}{\partial \theta_z}, \quad (2.86)$$

$$\ddot{\theta}_y + \frac{1}{I} \frac{\partial V}{\partial \theta_y} = -\dot{\omega}_2^H - \theta_x \dot{\omega}_3^H + \omega_3^H \dot{\theta}_x - \omega_1^H \dot{\theta}_z, \quad (2.87)$$

$$\ddot{\theta}_z + \frac{1}{I} \frac{\partial V}{\partial \theta_z} = -\dot{\omega}_3^H + \theta_x \dot{\omega}_2^H - \omega_2^H \dot{\theta}_x + \omega_1^H \dot{\theta}_y + \frac{\theta_y}{I} \frac{\partial V}{\partial \theta_x}. \quad (2.88)$$

These equations are much more reasonable, and clearly show the connection between the dynamics of the proof mass and the angular acceleration of the housing. It is clear that, in order to equate the angular acceleration of the housing to the angular acceleration of the angular coordinates of the proof mass, we must keep the angular displacement of the proof mass from the center of the housing, θ , and the velocity of this displacement, $\dot{\theta}$, to a minimum.

This can be achieved by applying force rebalance feedback to the angular degrees of freedom. This effectively stiffens the dynamics between the housing and the proof mass, and at the same time dampens any oscillations. The applied feedback exactly cancels the acceleration of the housing and holds the proof mass at rest with respect to the housing. This forces θ and $\dot{\theta}$ to vanish.

2.3 Superconducting Circuitry

The superconducting inductance bridge has been analyzed in detail by Paik [12] as a readout circuit for a gravitational-wave transducer. Input and output impedances, and forward and reverse transductances of the inductance-bridge transducer have been computed. Here we carry out a similar analysis, with less generality, for a more complex system: a six-axis accelerometer with a levitated proof mass.

We have taken our analysis as far as we are able without restricting the design to a particular geometric configuration. In this section we will present the actual geometry of the proof mass and describe the positions and orientations of the superconducting coils which surround it. We will also examine the superconducting circuitry which controls, levitates, and senses the position and orientation of the proof mass. We will compute the potential energy, V , of the superconducting circuitry, and derive the transfer functions that relate the output current of each bridge circuit to the applied displacement of the

proof mass. We will not, however, describe any construction details, but rather defer that discussion until a later chapter.

Figure 2.4 shows a perspective view of the proof mass for the six-axis accelerometer. Each of the three intersecting planes which make up the proof mass is defined to have a thickness of $2d$, and a length of $2L$. Twenty four sensing coils and twenty four levitation coils are mounted on eight titanium coil forms, as shown in Fig. 2.4. Each of the coil form surfaces on the titanium cubes contain one sensing coil and one levitation coil. Each of the coils in the accelerometer is labeled according to its position with respect to the proof mass coordinate system. For example, $L_{xy\bar{z}}^S$ is the inductance of the sensing coil above the xy plane in the $+x, +y$ quadrant on the $-z$ side of the proof mass. Similarly, $L_{\bar{y}zx}^L$ is the inductance of the levitation coil above the yz plane in the $-y, +z$ quadrant on the $+x$ side of the proof mass.

Each of the coils which surrounds the proof mass remains fixed to the accelerometer housing. The distance from the center of each coil to the proof mass surface, and the orientation of each coil with respect to the proof mass surface changes as the position and orientation of the proof mass change. This forces the inductance of each coil to change since the Meissner effect excludes all magnetic flux from the body of the proof mass. Before we can understand how the superconducting circuitry functions, it is necessary to compute the inductance of each superconducting coil in the SSA.

Paik [10] has shown that the inductance of a spiral coil above a superconducting plane is

$$L = L_0 + \Lambda r = \Lambda(r_0 + r), \quad (2.89)$$

where $\Lambda = \mu_0^2 A n_r^2$, A is the area of the spiral coil, r_0 is the effective spacing of the coil above the superconducting plane, and n_r is the number of turns per unit length along the radius. This expression can be expanded to include second order terms, i.e.,

$$L = L_0 + \Lambda r - \frac{\gamma}{2} r^2 - \frac{\beta}{2} \theta^2, \quad (2.90)$$

where γ and β are nonlinear coefficients which describe the change in inductance through second order for displacement (r) and orientation (θ). These coefficients will play a major role in determining the resonance frequencies of the SSA. These coefficients are important when the size of the levitation or sensing coil begins to approach the equilibrium distance away from the superconducting plane. We will calculate these parameters in Chapter 4 for our particular design.

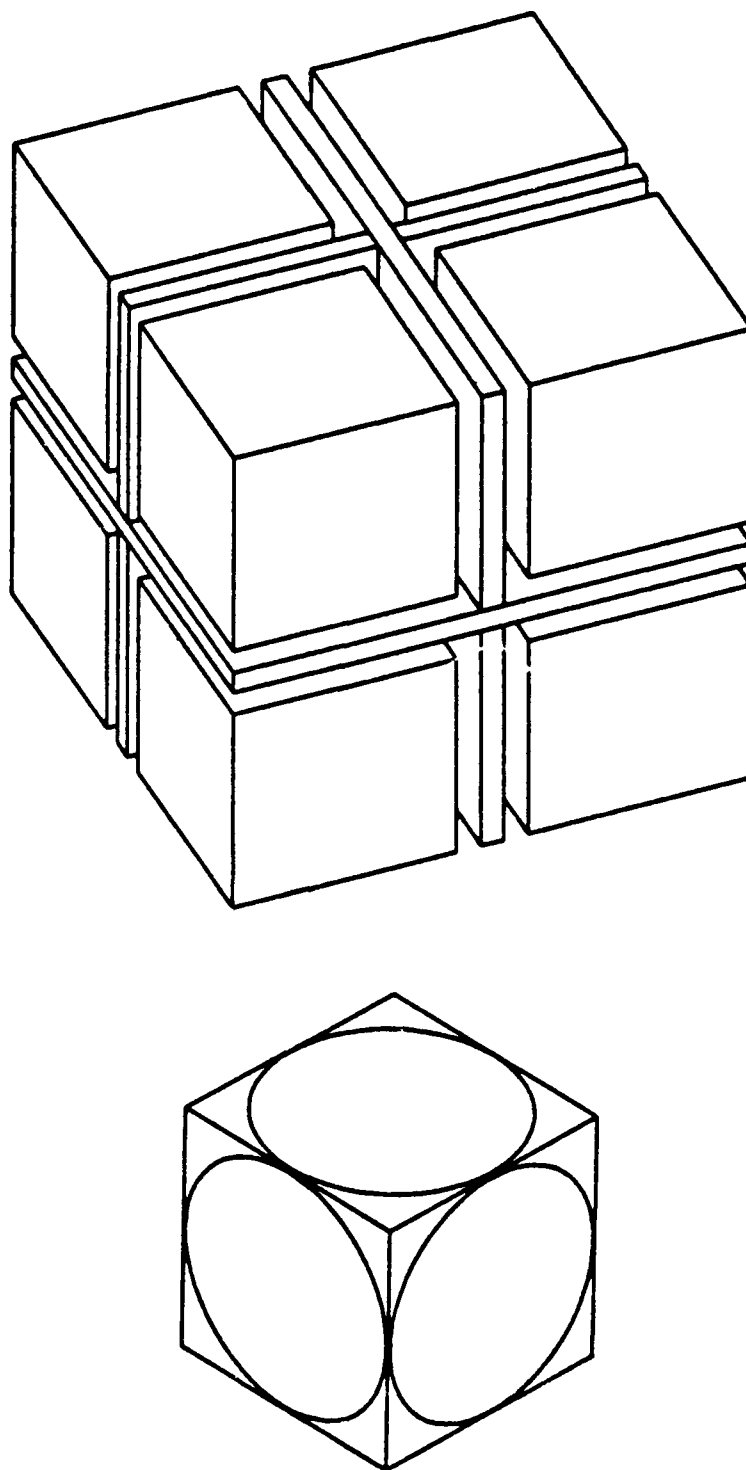


Figure 2.4. Perspective view of the six-axis accelerometer proof mass and coil forms.

| Coil | x | y | z | Coil | x | y | z | Coil | x | y | z |
|-----------------------------|------|------|------|-----------------------------|------|------|------|-----------------------------|------|------|------|
| L_{xzy} | c | d | c | L_{xyz} | c | c | d | L_{yzx} | d | c | c |
| $L_{x\bar{z}y}$ | c | d | $-c$ | $L_{\bar{x}yz}$ | $-c$ | c | d | $L_{\bar{y}zx}$ | d | $-c$ | c |
| $L_{\bar{x}\bar{z}y}$ | $-c$ | d | $-c$ | $L_{\bar{x}\bar{y}z}$ | $-c$ | $-c$ | d | $L_{\bar{y}\bar{z}x}$ | d | $-c$ | $-c$ |
| $L_{\bar{x}zy}$ | $-c$ | d | c | $L_{x\bar{y}z}$ | c | $-c$ | d | $L_{y\bar{z}x}$ | d | c | $-c$ |
| $L_{x\bar{z}\bar{y}}$ | c | $-d$ | c | $L_{x\bar{y}\bar{z}}$ | c | c | $-d$ | $L_{y\bar{z}\bar{x}}$ | $-d$ | c | c |
| $L_{\bar{x}\bar{z}\bar{y}}$ | c | $-d$ | $-c$ | $L_{\bar{x}\bar{y}\bar{z}}$ | $-c$ | c | $-d$ | $L_{\bar{y}\bar{z}\bar{x}}$ | $-d$ | $-c$ | c |
| $L_{\bar{x}z\bar{y}}$ | $-c$ | $-d$ | $-c$ | $L_{\bar{x}y\bar{z}}$ | $-c$ | $-c$ | $-d$ | $L_{\bar{y}z\bar{x}}$ | $-d$ | $-c$ | $-c$ |
| $L_{\bar{x}z\bar{y}}$ | $-c$ | $-d$ | c | $L_{x\bar{y}\bar{z}}$ | c | $-c$ | $-d$ | $L_{y\bar{z}\bar{x}}$ | $-d$ | c | $-c$ |

Table 2.1. Initial position of the center of the superconducting coils with respect to the center of the proof mass in the six-axis accelerometer.

Knowing the initial position and orientation of each coil allows us to compute the new spacing and orientation of each coil with respect to the proof mass. This new spacing and orientation, when combined with Eq. (2.90), describes the inductance of each coil in the SSA as a function of the position and orientation of the proof mass. If \mathbf{x}' is the initial position of the center of a coil, then, from Eq. (2.21), the coordinates of that point, as seen in the coordinate system attached to the proof mass, are

$$x_j = R_{ji}^{P^{-1}} (x'_i - r_i^P). \quad (2.91)$$

Only one of these three coordinates will have any significance. For example, in order to compute the inductance of the L_{xyz} coil, we need to know the displacement of the coil from the surface of the proof mass. After our transformation of the initial position of the L_{xyz} coil, only the z component will be needed, as the new position in x and y will not affect the inductance of the coil, since the L_{xyz} coil lies parallel to the x - y plane.

The initial position of the center of each of the coils in the accelerometer is given in Table 2.1, where d is the initial separation of each coil from the center of mass of the proof mass along the normal direction of the coil, and c is the initial separation of each coil from the center of mass along the direction parallel to the coil surface.

By taking the inverse of Eq. (2.73) and applying Eq. (2.91) to the initial position of the center of each coil, and expanding through second order in $\boldsymbol{\theta}$ and \mathbf{r}^P , it is possible to calculate the displacement of each coil away from the proof mass surface. A similar

calculation yields the orientation of the coil with respect to the proof mass. Substituting the displacement and orientation into Eq. (2.90) for each coil in the SSA, we find

$$L_{xzy} = L_0 + \Lambda \left[-r_y + c(\theta_x - \theta_z) + c\theta_y\theta_z - r_z\theta_x + r_x\theta_z - d(\theta_x^2 + \theta_z^2)/2 \right] - \frac{\gamma}{2} \left[r_y^2 + c^2(\theta_x - \theta_z)^2 - 2r_y c(\theta_x - \theta_z) \right] - \frac{\beta}{2} (\theta_x^2 + \theta_z^2), \quad (2.92)$$

$$L_{x\bar{z}y} = L_0 + \Lambda \left[-r_y + c(-\theta_x - \theta_z) - c\theta_z\theta_y - r_z\theta_x + r_x\theta_z - d(\theta_x^2 + \theta_z^2)/2 \right] - \frac{\gamma}{2} \left[r_y^2 + c^2(\theta_x + \theta_z)^2 + 2r_y c(\theta_x + \theta_z) \right] - \frac{\beta}{2} (\theta_x^2 + \theta_z^2), \quad (2.93)$$

$$L_{\bar{x}zy} = L_0 + \Lambda \left[-r_y + c(-\theta_x + \theta_z) - c\theta_z\theta_y - r_z\theta_x + r_x\theta_z - d(\theta_x^2 + \theta_z^2)/2 \right] - \frac{\gamma}{2} \left[r_y^2 + c^2(\theta_x - \theta_z)^2 + 2r_y c(\theta_x - \theta_z) \right] - \frac{\beta}{2} (\theta_x^2 + \theta_z^2), \quad (2.94)$$

$$L_{\bar{x}\bar{z}y} = L_0 + \Lambda \left[-r_y + c(\theta_x + \theta_z) + c\theta_z\theta_y - r_z\theta_x + r_x\theta_z - d(\theta_x^2 + \theta_z^2)/2 \right] - \frac{\gamma}{2} \left[r_y^2 + c^2(\theta_x + \theta_z)^2 - 2r_y c(\theta_x + \theta_z) \right] - \frac{\beta}{2} (\theta_x^2 + \theta_z^2), \quad (2.95)$$

$$L_{xzy\bar{y}} = L_0 + \Lambda \left[r_y + c(-\theta_x + \theta_z) - c\theta_z\theta_y + r_z\theta_x - r_x\theta_z - d(\theta_x^2 + \theta_z^2)/2 \right] - \frac{\gamma}{2} \left[r_y^2 + c^2(\theta_x - \theta_z)^2 - 2r_y c(\theta_x - \theta_z) \right] - \frac{\beta}{2} (\theta_x^2 + \theta_z^2), \quad (2.96)$$

$$L_{x\bar{z}\bar{y}} = L_0 + \Lambda \left[r_y + c(\theta_x + \theta_z) + c\theta_z\theta_y + r_z\theta_x - r_x\theta_z - d(\theta_x^2 + \theta_z^2)/2 \right] - \frac{\gamma}{2} \left[r_y^2 + c^2(\theta_x + \theta_z)^2 + 2r_y c(\theta_x + \theta_z) \right] - \frac{\beta}{2} (\theta_x^2 + \theta_z^2), \quad (2.97)$$

$$L_{\bar{x}zy\bar{y}} = L_0 + \Lambda \left[r_y + c(\theta_x - \theta_z) + c\theta_z\theta_y + r_z\theta_x - r_x\theta_z - d(\theta_x^2 + \theta_z^2)/2 \right] - \frac{\gamma}{2} \left[r_y^2 + c^2(\theta_x - \theta_z)^2 + 2r_y c(\theta_x - \theta_z) \right] - \frac{\beta}{2} (\theta_x^2 + \theta_z^2), \quad (2.98)$$

$$L_{\bar{x}\bar{z}\bar{y}} = L_0 + \Lambda \left[r_y + c(-\theta_x - \theta_z) - c\theta_z\theta_y + r_z\theta_x - r_x\theta_z - d(\theta_x^2 + \theta_z^2)/2 \right] - \frac{\gamma}{2} \left[r_y^2 + c^2(\theta_x + \theta_z)^2 - 2r_y c(\theta_x + \theta_z) \right] - \frac{\beta}{2} (\theta_x^2 + \theta_z^2), \quad (2.99)$$

$$L_{xy\bar{z}} = L_0 + \Lambda \left[-r_z + c(\theta_y - \theta_x) - r_x\theta_y + r_y\theta_x - d(\theta_x^2 + \theta_y^2)/2 \right] - \frac{\gamma}{2} \left[r_z^2 + c^2(\theta_x - \theta_y)^2 + 2r_z c(\theta_x - \theta_y) \right] - \frac{\beta}{2} (\theta_x^2 + \theta_y^2), \quad (2.100)$$

$$L_{\bar{x}y\bar{z}} = L_0 + \Lambda \left[-r_z + c(-\theta_y - \theta_x) - r_x\theta_y + r_y\theta_x - d(\theta_x^2 + \theta_y^2)/2 \right] - \frac{\gamma}{2} \left[r_z^2 + c^2(\theta_x + \theta_y)^2 + 2r_z c(\theta_x + \theta_y) \right] - \frac{\beta}{2} (\theta_x^2 + \theta_y^2), \quad (2.101)$$

$$L_{x\bar{y}\bar{z}} = L_0 + \Lambda \left[-r_z + c(-\theta_y + \theta_x) - r_x\theta_y + r_y\theta_x - d(\theta_x^2 + \theta_y^2)/2 \right] - \frac{\gamma}{2} \left[r_z^2 + c^2(\theta_x - \theta_y)^2 - 2r_z c(\theta_x - \theta_y) \right] - \frac{\beta}{2} (\theta_x^2 + \theta_y^2), \quad (2.102)$$

$$L_{x\bar{y}z} = L_0 + \Lambda \left[-r_z + c(\theta_y + \theta_x) - r_x\theta_y + r_y\theta_x - d(\theta_x^2 + \theta_y^2)/2 \right]$$

$$- \frac{\gamma}{2} \left[r_z^2 + c^2(\theta_x + \theta_y)^2 - 2r_z c(\theta_x + \theta_y) \right] - \frac{\beta}{2} (\theta_x^2 + \theta_y^2), \quad (2.103)$$

$$\begin{aligned} L_{xy\bar{z}} &= L_0 + \Lambda \left[r_z + c(-\theta_y + \theta_x) + r_x \theta_y - r_y \theta_x - d(\theta_x^2 + \theta_y^2)/2 \right] \\ &\quad - \frac{\gamma}{2} \left[r_z^2 + c^2(\theta_x - \theta_y)^2 + 2r_z c(\theta_x - \theta_y) \right] - \frac{\beta}{2} (\theta_x^2 + \theta_y^2), \end{aligned} \quad (2.104)$$

$$\begin{aligned} L_{\bar{x}y\bar{z}} &= L_0 + \Lambda \left[r_z + c(\theta_y + \theta_x) + r_x \theta_y - r_y \theta_x - d(\theta_x^2 + \theta_y^2)/2 \right] \\ &\quad - \frac{\gamma}{2} \left[r_z^2 + c^2(\theta_x + \theta_y)^2 + 2r_z c(\theta_x + \theta_y) \right] - \frac{\beta}{2} (\theta_x^2 + \theta_y^2), \end{aligned} \quad (2.105)$$

$$\begin{aligned} L_{\bar{x}\bar{y}\bar{z}} &= L_0 + \Lambda \left[r_z + c(\theta_y - \theta_x) + r_x \theta_y - r_y \theta_x - d(\theta_x^2 + \theta_y^2)/2 \right] \\ &\quad - \frac{\gamma}{2} \left[r_z^2 + c^2(\theta_x - \theta_y)^2 - 2r_z c(\theta_x - \theta_y) \right] - \frac{\beta}{2} (\theta_x^2 + \theta_y^2), \end{aligned} \quad (2.106)$$

$$\begin{aligned} L_{x\bar{y}\bar{z}} &= L_0 + \Lambda \left[r_z + c(-\theta_y - \theta_x) + r_x \theta_y - r_y \theta_x - d(\theta_x^2 + \theta_y^2)/2 \right] \\ &\quad - \frac{\gamma}{2} \left[r_z^2 + c^2(\theta_x + \theta_y)^2 - 2r_z c(\theta_x + \theta_y) \right] - \frac{\beta}{2} (\theta_x^2 + \theta_y^2), \end{aligned} \quad (2.107)$$

$$\begin{aligned} L_{yzz} &= L_0 + \Lambda \left[-r_x + c(\theta_z - \theta_y) + c(\theta_y \theta_x + \theta_z \theta_x) - r_y \theta_z + r_z \theta_y - d(\theta_y^2 + \theta_z^2)/2 \right] \\ &\quad - \frac{\gamma}{2} \left[r_x^2 + c^2(\theta_y - \theta_z)^2 + 2r_x c(\theta_y - \theta_z) \right] - \frac{\beta}{2} (\theta_y^2 + \theta_z^2), \end{aligned} \quad (2.108)$$

$$\begin{aligned} L_{\bar{y}zz} &= L_0 + \Lambda \left[-r_x - c(\theta_z + \theta_y) + c(\theta_z \theta_x - \theta_y \theta_x) - r_y \theta_z + r_z \theta_y - d(\theta_y^2 + \theta_z^2)/2 \right] \\ &\quad - \frac{\gamma}{2} \left[r_x^2 + c^2(\theta_y + \theta_z)^2 + 2r_x c(\theta_y + \theta_z) \right] - \frac{\beta}{2} (\theta_y^2 + \theta_z^2), \end{aligned} \quad (2.109)$$

$$\begin{aligned} L_{\bar{y}\bar{z}z} &= L_0 + \Lambda \left[-r_x + c(\theta_y - \theta_z) - c(\theta_y \theta_x + \theta_z \theta_x) - r_y \theta_z + r_z \theta_y - d(\theta_y^2 + \theta_z^2)/2 \right] \\ &\quad - \frac{\gamma}{2} \left[r_x^2 + c^2(\theta_y - \theta_z)^2 - 2r_x c(\theta_y - \theta_z) \right] - \frac{\beta}{2} (\theta_y^2 + \theta_z^2), \end{aligned} \quad (2.110)$$

$$\begin{aligned} L_{y\bar{z}z} &= L_0 + \Lambda \left[-r_x + c(\theta_z + \theta_y) + c(\theta_y \theta_x - \theta_z \theta_x) - r_y \theta_z + r_z \theta_y - d(\theta_y^2 + \theta_z^2)/2 \right] \\ &\quad - \frac{\gamma}{2} \left[r_x^2 + c^2(\theta_y - \theta_z)^2 - 2r_x c(\theta_y + \theta_z) \right] - \frac{\beta}{2} (\theta_y^2 + \theta_z^2), \end{aligned} \quad (2.111)$$

$$\begin{aligned} L_{yzz\bar{z}} &= L_0 + \Lambda \left[r_x + c(\theta_y - \theta_z) - c(\theta_y \theta_x + \theta_z \theta_x) + r_y \theta_z - r_z \theta_y - d(\theta_y^2 + \theta_z^2)/2 \right] \\ &\quad - \frac{\gamma}{2} \left[r_x^2 + c^2(\theta_y - \theta_z)^2 + 2r_x c(\theta_y - \theta_z) \right] - \frac{\beta}{2} (\theta_y^2 + \theta_z^2), \end{aligned} \quad (2.112)$$

$$\begin{aligned} L_{\bar{y}z\bar{z}} &= L_0 + \Lambda \left[r_x + c(\theta_z + \theta_y) + c(\theta_y \theta_x - \theta_z \theta_x) + r_y \theta_z - r_z \theta_y - d(\theta_y^2 + \theta_z^2)/2 \right] \\ &\quad - \frac{\gamma}{2} \left[r_x^2 + c^2(\theta_y + \theta_z)^2 + 2r_x c(\theta_y + \theta_z) \right] - \frac{\beta}{2} (\theta_y^2 + \theta_z^2), \end{aligned} \quad (2.113)$$

$$\begin{aligned} L_{\bar{y}\bar{z}\bar{z}} &= L_0 + \Lambda \left[r_x + c(\theta_z - \theta_y) + c(\theta_y \theta_x + \theta_z \theta_x) + r_y \theta_z - r_z \theta_y - d(\theta_y^2 + \theta_z^2)/2 \right] \\ &\quad - \frac{\gamma}{2} \left[r_x^2 + c^2(\theta_y - \theta_z)^2 - 2r_x c(\theta_y - \theta_z) \right] - \frac{\beta}{2} (\theta_y^2 + \theta_z^2), \end{aligned} \quad (2.114)$$

$$L_{y\bar{z}\bar{z}} = L_0 + \Lambda \left[r_x - c(\theta_z + \theta_y) + c(\theta_z \theta_x - \theta_y \theta_x) + r_y \theta_z - r_z \theta_y - d(\theta_y^2 + \theta_z^2)/2 \right]$$

$$- \frac{\gamma}{2} \left[r_x^2 + c^2(\theta_y + \theta_z)^2 - 2r_x c(\theta_y + \theta_z) \right] - \frac{\beta}{2} (\theta_y^2 + \theta_z^2), \quad (2.115)$$

where we have simplified our notation from r^P to r , since, from this point on, we will only be interested in displacements of the proof mass relative to the accelerometer housing. The fact that the equations for inductance are not symmetric stems from the non-commutivity of the three successive rotations used to describe the orientation of the proof mass in Eq. (2.72).

Although each coil form in the accelerometer contains two coils, they share a common center, and we have been able to treat them identically. Thus, both the levitation and the sensing coils obey the same formula for inductance but the parameters L_0 , Λ , β , γ , and d are different, so, later in our formulas, we will distinguish these coils by substituting L_S , Λ_S , β_S , γ_S , and d_S for the sensing inductance parameters, and L_L , Λ_L , β_L , γ_L , and d_L for the levitation inductance parameters.

The SSA is oriented in the so called "umbrella" orientation, so that all three sensitive axes make the same angle to the vertical. This orientation is identical to the orientation of the gravity gradiometer, and has the advantage of distributing the pull of gravity equally among the three axes.

2.3.1 Levitation Circuitry

In the presence of gravity, the r_x , r_y , and r_z levitation circuits each must equally levitate the proof mass. These three circuits are shown in Fig. 2.5. In examining the r_x levitation circuit, we see that all four of the levitation coils are located at the back of the x plane of the proof mass. If a current is stored in the r_x levitation circuit, all four coils will push the proof mass upward equally. This is the source of the force that levitates the proof mass. The additional transformer is included simply so that we can add or subtract current from the circuit in order to raise or lower the proof mass position and apply feedback.

The r_x levitation circuit contains a single loop about which the trapped flux must remain constant. We can treat the five inductances in this circuit as one equivalent inductance:

$$L_{yz\bar{x}} + L_{\bar{y}z\bar{x}} + L_{y\bar{z}\bar{x}} + L_{y\bar{z}\bar{x}} + L. \quad (2.116)$$

If we store a levitation current, I_{r_x} , in this circuit, then the amount of trapped flux is

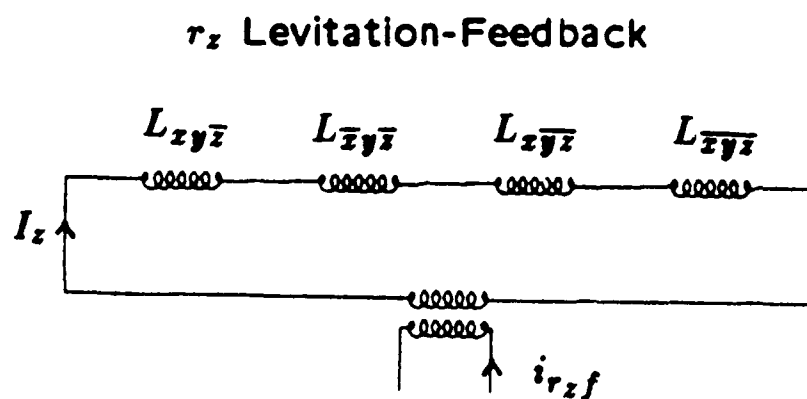
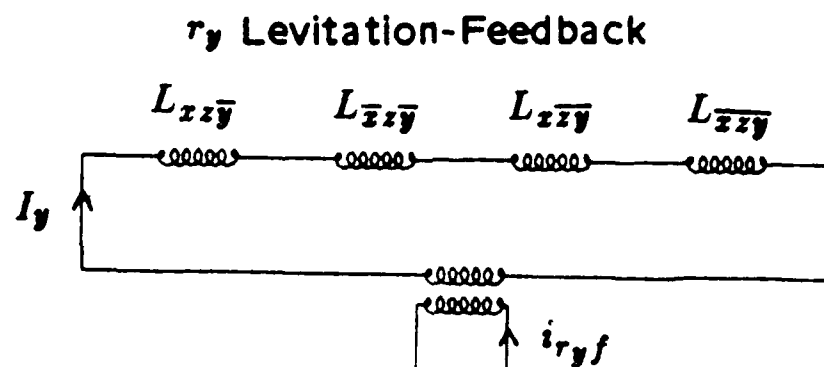
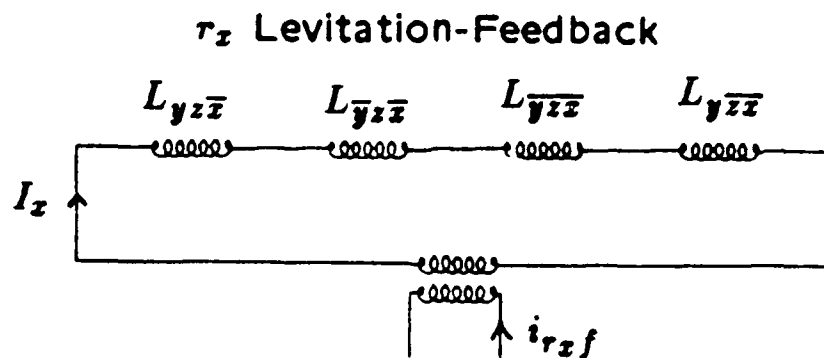


Figure 2.5. Linear superconducting levitation and feedback circuitry.

$(4L_L + L)I_{r_x}$, and the potential energy of this circuit is, therefore,

$$V_{r_x} = \frac{(4L_L + L)^2 I_{r_x}^2}{2(L_{y_z \bar{x}} + L_{\bar{y} z \bar{x}} + L_{\bar{y} z \bar{x}} + L_{y \bar{z} \bar{x}} + L)}. \quad (2.117)$$

Substituting the required inductances, and expanding this to second order in r and θ gives

$$\begin{aligned} V_{r_x} = & \frac{(4L_L + L)I_{r_x}^2}{2} - 2I_{r_x}^2 \Lambda_L r_x + \left(\frac{8\Lambda_L^2}{4L_L + L} + \gamma_L \right) I_{r_x}^2 r_x^2 \\ & + 2I_{r_x}^2 \Lambda_L (\theta_y r_z - \theta_z r_y) + I_{r_x}^2 (\Lambda_L d_L + c^2 \gamma_L + \beta_L) (\theta_y^2 + \theta_z^2). \end{aligned} \quad (2.118)$$

Thus we see that our r_x levitation circuit provides a levitation force, $2I_{r_x}^2 \Lambda_L$, and an additional spring constant, $2[8\Lambda_L^2/(4L_L + L) + \gamma_L]I_{r_x}^2$. There is also an interesting cross coupling term.

Similar analysis of the r_y and r_z levitation circuits leads to

$$\begin{aligned} V_{r_y} = & \frac{(4L_L + L)I_{r_y}^2}{2} - 2I_{r_y}^2 \Lambda_L r_y + \left(\frac{8\Lambda_L^2}{4L_L + L} + \gamma_L \right) I_{r_y}^2 r_y^2 \\ & + 2I_{r_y}^2 \Lambda_L (\theta_z r_x - \theta_x r_z) + I_{r_y}^2 (\Lambda_L d_L + c^2 \gamma_L + \beta_L) (\theta_x^2 + \theta_z^2), \end{aligned} \quad (2.119)$$

$$\begin{aligned} V_{r_z} = & \frac{(4L_L + L)I_{r_z}^2}{2} - 2I_{r_z}^2 \Lambda_L r_z + \left(\frac{8\Lambda_L^2}{4L_L + L} + \gamma_L \right) I_{r_z}^2 r_z^2 \\ & + 2I_{r_z}^2 \Lambda_L (\theta_x r_y - \theta_y r_x) + I_{r_z}^2 (\Lambda_L d_L + c^2 \gamma_L + \beta_L) (\theta_x^2 + \theta_y^2). \end{aligned} \quad (2.120)$$

The three angular levitation circuits are a bit more complicated. These circuits are shown in Fig. 2.6. Each of the three circuits contains four levitation coils, and one feedback transformer. Each set of four levitation coils is mounted on the upper side of one of the proof mass planes. The θ_x circuit contains the four levitation coils on the upper side of the proof mass's z plane. Two independent currents are stored in each of the two superconducting loops in the angular circuits. In the θ_x circuit shown in Fig. 2.5, the current in the loop on the left, $I_{1\theta_x}$, tends to rotate the proof mass about x axis in a counter-clockwise manner, and the current in the loop on the right, $I_{2\theta_x}$, tends to rotate the proof mass about the x axis in a clockwise manner. Both currents tend to push the proof mass downward in the $-z$ direction. The feedback transformer is included so that the angular position of the proof mass can be controlled. If the same current is stored in each loop of the θ_x circuit, then any additional current added by the feedback transformer will tend to decrease one current and increase the other. This change in

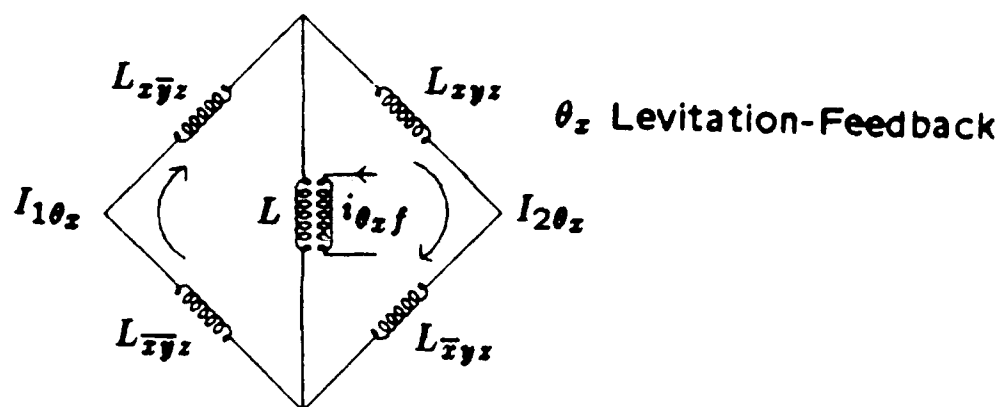
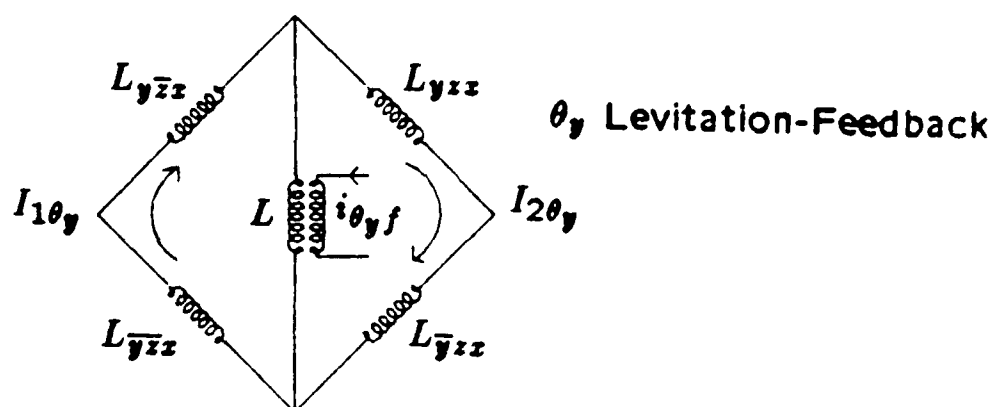
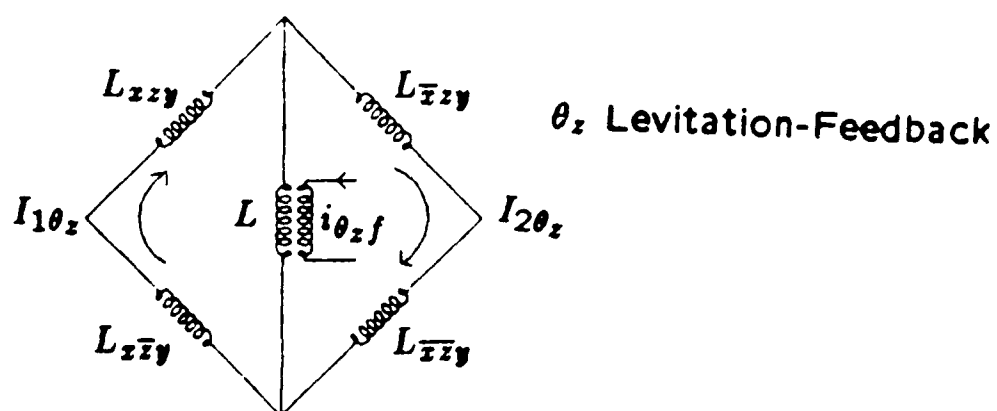


Figure 2.6. Angular superconducting levitation and feedback circuitry.

the currents in the two loops will apply a torque to the proof mass. This can be seen quantitatively by computing the potential energy of the θ_x levitation circuit.

The two flux conservation equations for the θ_x circuit are, ignoring $i_{\theta_x f}$,

$$(I_{1\theta_x} + i_1)(L_{x\bar{y}z} + L_{\bar{x}\bar{y}z}) + (I_{1\theta_x} + i_1 - I_{2\theta_x} - i_2)L = 2L_L I_{1\theta_x} + (I_{1\theta_x} - I_{2\theta_x})L, \quad (2.121)$$

$$(I_{2\theta_x} + i_2)(L_{xyz} + L_{\bar{x}\bar{y}z}) + (I_{2\theta_x} + i_2 - I_{1\theta_x} - i_1)L = 2L_L I_{2\theta_x} + (I_{2\theta_x} - I_{1\theta_x})L. \quad (2.122)$$

The potential energy of the θ_x levitation circuit is simply the electromagnetic energy stored in the inductances:

$$\begin{aligned} V_{\theta_x} = & \frac{1}{2}(L_{x\bar{y}z} + L_{\bar{x}\bar{y}z})(I_{1\theta_x} + i_1)^2 + \frac{1}{2}(L_{xyz} + L_{\bar{x}\bar{y}z})(I_{2\theta_x} + i_2)^2 \\ & + \frac{1}{2}L(I_{2\theta_x} + i_2 - I_{1\theta_x} - i_1)^2. \end{aligned} \quad (2.123)$$

Solving Eqs. (2.121) and (2.122) for i_1 and i_2 , substituting these currents and the required inductances into our expression for V_{θ_x} , and expanding V_{θ_x} to second order in r and θ gives

$$\begin{aligned} V_{\theta_x} = & (I_{2\theta_x}^2 + I_{1\theta_x}^2)L_L + \frac{1}{2}(I_{2\theta_x} - I_{1\theta_x})^2 L \\ & + (I_{2\theta_x}^2 + I_{1\theta_x}^2)\Lambda_L r_z + (I_{2\theta_x}^2 - I_{1\theta_x}^2)c\Lambda_L \theta_x \\ & + (I_{2\theta_x}^2 + I_{1\theta_x}^2)\frac{\Lambda_L^2}{L_L + L}r_z^2 + (I_{2\theta_x} + I_{1\theta_x})^2\frac{L\Lambda_L^2}{2L_L(L_L + L)}r_z^2 \\ & + (I_{2\theta_x}^2 - I_{1\theta_x}^2)\left[\frac{\Lambda_L^2(2L_L + L)}{L_L(L_L + L)} + \gamma_L\right]c\theta_x r_z + (I_{1\theta_x}^2 + I_{2\theta_x}^2)\Lambda_L(\theta_y r_x - \theta_x r_y) \\ & + (I_{2\theta_x}^2 + I_{1\theta_x}^2)\frac{c^2\Lambda_L^2}{L_L + L}\theta_x^2 + (I_{2\theta_x} - I_{1\theta_x})^2\frac{L\Lambda_L^2 c^2}{2L_L(L_L + L)}\theta_x^2 \\ & + \frac{1}{2}(I_{2\theta_x}^2 + I_{1\theta_x}^2)(\Lambda_L d_L + c^2\gamma_L + \beta_L)(\theta_x^2 + \theta_y^2). \end{aligned} \quad (2.124)$$

This potential looks quite complicated; however, we can immediately recognize the main features. The difference in the two currents $I_{1\theta_x}$ and $I_{2\theta_x}$ applies a torque to the proof mass about the x axis, and both currents push the proof mass downward in the $-z$ direction. The rest of the terms describe the "magnetic" spring due to the circuitry.

Similar analysis of the θ_y and θ_z levitation circuits gives

$$\begin{aligned} V_{\theta_y} = & (I_{2\theta_y}^2 + I_{1\theta_y}^2)L_L + \frac{1}{2}(I_{2\theta_y} - I_{1\theta_y})^2 L \\ & + (I_{2\theta_y}^2 + I_{1\theta_y}^2)\Lambda_L r_x + (I_{2\theta_y}^2 - I_{1\theta_y}^2)c\Lambda_L \theta_y \end{aligned}$$

$$\begin{aligned}
& + (I_{2\theta_y}^2 + I_{1\theta_y}^2) \frac{\Lambda_L^2}{L_L + L} r_x^2 + (I_{2\theta_y} + I_{1\theta_y})^2 \frac{L\Lambda_L^2}{2L_L(L_L + L)} r_x^2 \\
& + (I_{2\theta_y}^2 - I_{1\theta_y}^2) \left[\frac{\Lambda_L^2(2L_L + L)}{L_L(L_L + L)} + \gamma_L \right] c\theta_y r_x + (I_{1\theta_y}^2 + I_{2\theta_y}^2) \Lambda_L (\theta_z r_y - \theta_y r_z) \\
& + (I_{2\theta_y}^2 + I_{1\theta_y}^2) \frac{c^2 \Lambda_L^2}{L_L + L} \theta_y^2 + (I_{2\theta_y} - I_{1\theta_y})^2 \frac{L\Lambda_L^2 c^2}{2L_L(L_L + L)} \theta_y^2 \\
& + \frac{1}{2} (I_{2\theta_y}^2 + I_{1\theta_y}^2) (\Lambda_L d_L + c^2 \gamma_L + \beta_L) (\theta_y^2 + \theta_z^2) \\
& - (I_{2\theta_y}^2 - I_{1\theta_y}^2) \Lambda_L c \theta_z \theta_x, \tag{2.125}
\end{aligned}$$

$$\begin{aligned}
V_{\theta_z} = & (I_{2\theta_z}^2 + I_{1\theta_z}^2) L_L + \frac{1}{2} (I_{2\theta_z} - I_{1\theta_z})^2 L \\
& + (I_{2\theta_z}^2 + I_{1\theta_z}^2) \Lambda_L r_y + (I_{2\theta_z}^2 - I_{1\theta_z}^2) c \Lambda_L \theta_z \\
& + (I_{2\theta_z}^2 + I_{1\theta_z}^2) \frac{\Lambda_L^2}{L_L + L} r_y^2 + (I_{2\theta_z} + I_{1\theta_z})^2 \frac{L\Lambda_L^2}{2L_L(L_L + L)} r_y^2 \\
& + (I_{2\theta_z}^2 - I_{1\theta_z}^2) \left[\frac{\Lambda_L^2(2L_L + L)}{L_L(L_L + L)} - \gamma_L \right] c\theta_z r_y + (I_{1\theta_z}^2 + I_{2\theta_z}^2) \Lambda_L (\theta_x r_z - \theta_z r_x) \\
& + (I_{2\theta_z}^2 + I_{1\theta_z}^2) \frac{c^2 \Lambda_L^2}{L_L + L} \theta_z^2 + (I_{2\theta_z} - I_{1\theta_z})^2 \frac{L\Lambda_L^2 c^2}{2L_L(L_L + L)} \theta_z^2 \\
& + \frac{1}{2} (I_{2\theta_z}^2 + I_{1\theta_z}^2) (\Lambda_L d_L + c^2 \gamma_L + \beta_L) (\theta_x^2 + \theta_z^2). \tag{2.126}
\end{aligned}$$

We can now combine all the different potentials applied to the proof mass by the superconducting levitation circuitry. Because the SSA is operated in an umbrella orientation, equal amounts of levitation current are stored in the three linear circuits, thus we will let $I_{r_x} = I_{r_y} = I_{r_z} = I_+$ in Eqs. (2.118), (2.119), and (2.120). Similarly, we will store equal amounts of levitation current in each of the three angular circuits. Since we do not initially want to apply any torque to the proof mass, we will store equal amounts of current on each side of the angular circuits. With this in mind, we will let $I_{1\theta_x} = I_{2\theta_x} = I_{1\theta_y} = I_{2\theta_y} = I_{1\theta_z} = I_{2\theta_z} = I_-$ in Eqs. (2.124), (2.125), and (2.126). Combining all these equations together, we find that the total potential energy of all the levitation circuits together, V_L , is

$$\begin{aligned}
V_L = & \frac{3}{2} (4L_L + L) I_+^2 + 6I_-^2 L_L + 2(I_-^2 - I_+^2) \Lambda_L (r_x + r_y + r_z) \\
& + \left[2I_-^2 \frac{\Lambda_L^2}{L_L} + \left(\frac{8\Lambda_L^2}{4L_L + L} + \gamma_L \right) I_+^2 \right] (r_x^2 + r_y^2 + r_z^2) \\
& + \left[2(I_+^2 + I_-^2) (\Lambda_L d_L + c^2 \gamma_L + \beta_L) + 2I_-^2 \frac{c^2 \Lambda_L^2}{L_L + L} \right] (\theta_x^2 + \theta_y^2 + \theta_z^2) \\
& + 2(I_-^2 - I_+^2) \Lambda_L [\theta_x(r_z - r_y) + \theta_y(r_x - r_z) + \theta_z(r_y - r_x)]. \tag{2.127}
\end{aligned}$$

2.3.2 Sensing Circuitry

We have claimed that the sensing circuitry in Fig. 2.7 will provide us with information about each of the six degrees of freedom. At this point we will analyze the sensitivity to motion in the r_x degree of freedom. The r_x sensing circuit can be simplified to the circuit shown in Fig. 2.8, where we have replaced the other sensing inductance bridges by their equivalent inductance at equilibrium, L_S . The load on the portion of the circuit sensitive to r_x is then $L_{SQ} + 5L_S$, where L_{SQ} is the input inductance of the SQUID amplifier.

The sensing circuit for r_x in this simplified form, contains two independent superconducting loops about which the trapped flux must remain constant. In this case, the initial flux is zero, and we may write two flux conservation equations:

$$(L_{\bar{y}z\bar{x}} + L_{yzz})I + L_{yzz}I_0 \cos(\omega_{r_x}t) + (L_{SQ} + 5L_S)i_{r_x} = 0, \quad (2.128)$$

$$(L_{\bar{y}z\bar{x}} + L_{yzz})I - (L_{SQ} + 5L_S + L_{\bar{y}zx} + L_{y\bar{z}\bar{x}})i_{r_x} + L_{y\bar{z}\bar{x}}I_0 \cos(\omega_{r_x}t) = 0. \quad (2.129)$$

Solving these two equations for the current through the SQUID amplifier, i_{r_x} , we find

$$i_{r_x} = \frac{I_0 \cos(\omega_{r_x}t) (L_{yzz}L_{\bar{y}z\bar{x}} - L_{\bar{y}z\bar{x}}L_{y\bar{z}\bar{x}})}{[(L_{SQ} + 5L_S)(L_{\bar{y}z\bar{x}} + L_{yzz} + L_{\bar{y}zx} + L_{y\bar{z}\bar{x}}) + (L_{\bar{y}z\bar{x}} + L_{yzz})(L_{\bar{y}z\bar{x}} + L_{y\bar{z}\bar{x}})]}. \quad (2.130)$$

Substituting Eqs. (2.113), (2.108), (2.110), and (2.115) for $L_{\bar{y}z\bar{x}}$, L_{yzz} , $L_{\bar{y}zx}$, and $L_{y\bar{z}\bar{x}}$, respectively, into the above equation, we find, after expanding to second order in r and θ ,

$$i_{r_x} = I_0 \cos(\omega_{r_x}t) \left[\frac{\Lambda_S r_x}{L_{SQ} + 6L_S} + \frac{\Lambda_S(r_y\theta_z - r_z\theta_y)}{L_{SQ} + 6L_S} - \frac{c^2(\Lambda_S^2 + \gamma_S L_S)\theta_y\theta_z}{L_S(L_{SQ} + 6L_S)} + \dots \right]. \quad (2.131)$$

Thus we see that i_{r_x} is directly proportional to the position of the accelerometer in r_x .

Similar analysis of the y , z , θ_x , θ_y , and θ_z sensing circuits leads to

$$i_{r_y} = I_0 \cos(\omega_{r_y}t) \left[\frac{\Lambda_S r_y}{L_{SQ} + 6L_S} + \frac{\Lambda_S(r_z\theta_x - r_x\theta_z)}{L_{SQ} + 6L_S} - \frac{c^2(\Lambda_S^2 + \gamma_S L_S)\theta_x\theta_z}{L_S(L_{SQ} + 6L_S)} + \dots \right], \quad (2.132)$$

$$i_{r_z} = I_0 \cos(\omega_{r_z}t) \left[\frac{\Lambda_S r_z}{L_{SQ} + 6L_S} + \frac{\Lambda_S(r_x\theta_y - r_y\theta_x)}{L_{SQ} + 6L_S} - \frac{c^2(\Lambda_S^2 + \gamma_S L_S)\theta_x\theta_y}{L_S(L_{SQ} + 6L_S)} + \dots \right], \quad (2.133)$$

$$i_{\theta_x} = I_0 \cos(\omega_{\theta_x}t) \left[\frac{c\Lambda_S\theta_x}{L_{SQ} + 6L_S} + \frac{(\Lambda_S^2 + \gamma_S L_S)c\theta_y r_z}{L_S(L_{SQ} + 6L_S)} + \dots \right], \quad (2.134)$$

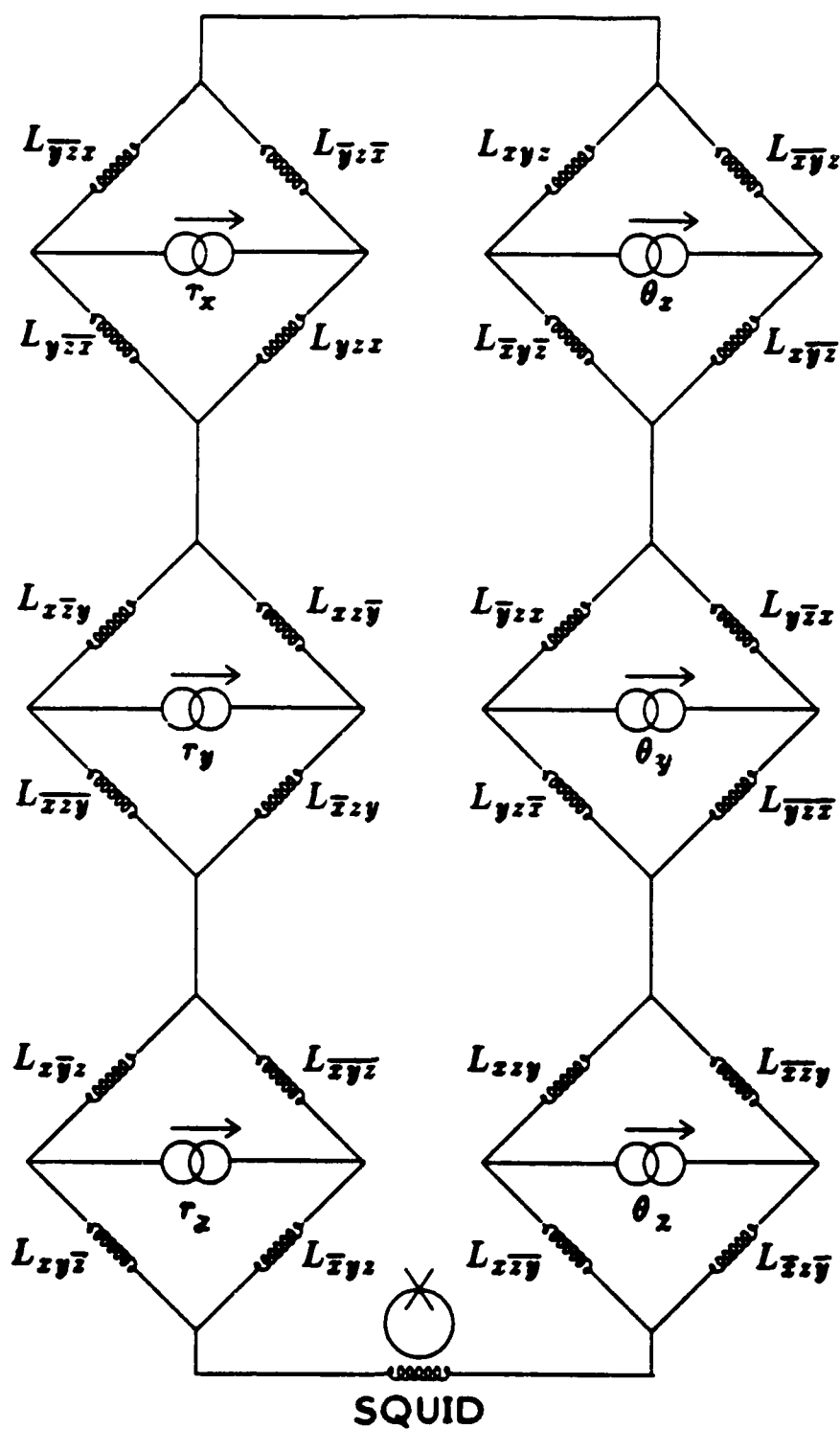


Figure 2.7. Superconducting sensing circuitry.

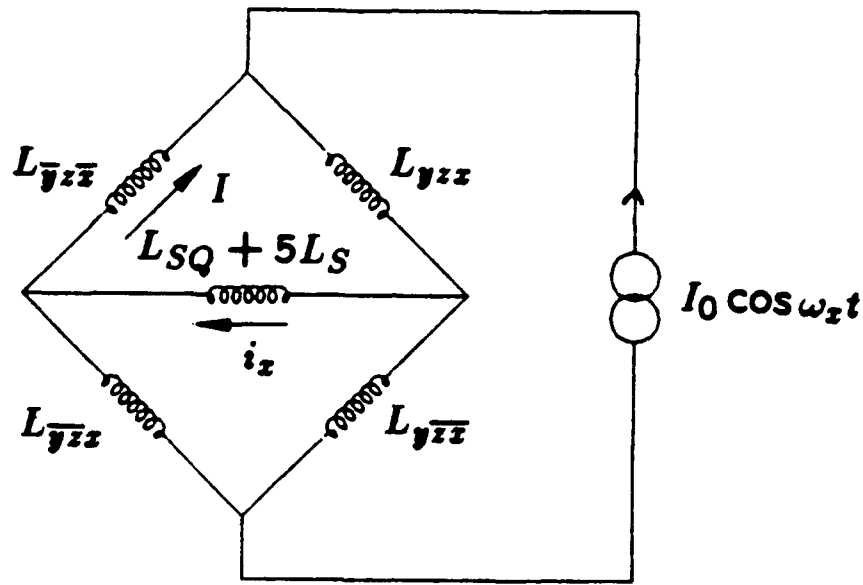


Figure 2.8. Simplified superconducting sensing circuitry for the r_x degree of freedom.

$$i_{\theta_y} = I_0 \cos(\omega_{\theta_y} t) \left[\frac{c\Lambda_S \theta_y}{L_{SQ} + 6L_S} + \frac{(\Lambda_S^2 + \gamma_S L_S) c\theta_z r_x - L_S c\Lambda_S \theta_x \theta_z}{L_S (L_{SQ} + 6L_S)} + \dots \right], \quad (2.135)$$

$$i_{\theta_z} = I_0 \cos(\omega_{\theta_z} t) \left[\frac{c\Lambda_S \theta_z}{L_{SQ} + 6L_S} + \frac{(\Lambda_S^2 + \gamma_S L_S) c\theta_x r_y}{L_S (L_{SQ} + 6L_S)} + \dots \right]. \quad (2.136)$$

The final current that flows through the SQUID is the combined total, $i_{r_x} + i_{r_y} + i_{r_z} + i_{\theta_x} + i_{\theta_y} + i_{\theta_z}$, and if each bridge is modulated with a different frequency current, then it is possible to recover each individual output. This is accomplished by utilizing six lock-in amplifiers, each one tuned to the separate carrier frequency.

Each sensing circuit will affect the dynamics of the proof mass. As the proof mass changes position with respect to the bridge inductances, the currents flowing through the circuit must redistribute. This change in current patterns redistributes the energy stored in the sensing bridge and changes the magnetic potential energy. As the amount of sensing current is increased, the stiffness of the "magnetic" springs surrounding the proof mass is increased. In order to understand this quantitatively, it is necessary to compute the amount of energy stored in the sensing bridges as the position of the proof mass changes. The total electromagnetic energy stored in the r_x sensing circuit is, from Fig. 2.8,

$$E = \frac{1}{2} L_{\bar{y}\bar{z}\bar{x}} I^2 + \frac{1}{2} L_{yzz} (I + I_0 \cos \omega_{r_x} t)^2 + \frac{1}{2} L_{\bar{y}\bar{z}x} (I - i_{r_x})^2$$

$$+ \frac{1}{2} L_{y\bar{z}\bar{x}} (I + I_0 \cos \omega_{r_x} t - i_{r_x})^2 + \frac{1}{2} (L_{SQ} + 5L_S) i_{r_x}^2. \quad (2.137)$$

This is not the correct potential energy of the sensing circuit, however. As the proof mass moves, the current source attached to the sensing circuit must maintain a current $I_0 \cos \omega_x t$. This forces the current source to supply energy. The voltage induced across the current source is the time rate of change of the magnetic flux across the bridge:

$$V = \frac{d}{dt} \Phi = \frac{d}{dt} [L_{yzz}(I + I_0 \cos \omega_{r_x} t) + L_{y\bar{z}\bar{x}}(I + I_0 \cos \omega_{r_x} t - i_{r_x})]. \quad (2.138)$$

The power supplied by the current source at any instance of time is the product of the voltage drop and the supplied current, i.e.,

$$P = I_0 \cos \omega_{r_x} t \frac{d}{dt} [L_{yzz}(I + I_0 \cos \omega_{r_x} t) + L_{y\bar{z}\bar{x}}(I + I_0 \cos \omega_{r_x} t - i_{r_x})]. \quad (2.139)$$

If we now displace the proof mass a small distance δx away from equilibrium, then we can compute the force in the x direction, f_x . The energy we have received in this displacement is $f_x \delta x$. The change in the total electromagnetic energy stored in the sensing circuit is $(dE/dx)\delta x$, and the amount of work done by the current supply is

$$\begin{aligned} W_C &= \int P dt \\ &= \int I_0 \cos \omega_{r_x} t \frac{d}{dt} [L_{yzz}(I + I_0 \cos \omega_{r_x} t) + L_{y\bar{z}\bar{x}}(I + I_0 \cos \omega_{r_x} t - i_{r_x})] dt \\ &= \int I_0 \cos \omega_{r_x} t \frac{d}{dx} [L_{yzz}(I + I_0 \cos \omega_{r_x} t) + L_{y\bar{z}\bar{x}}(I + I_0 \cos \omega_{r_x} t - i_{r_x})] \frac{dx}{dt} dt \\ &= I_0 \cos \omega_{r_x} t \frac{d}{dx} [L_{yzz}(I + I_0 \cos \omega_{r_x} t) + L_{y\bar{z}\bar{x}}(I + I_0 \cos \omega_{r_x} t - i_{r_x})] \delta x. \end{aligned} \quad (2.140)$$

Thus conservation of total energy demands that

$$W_C = \frac{dE}{dx} \delta x + f_x \delta x. \quad (2.141)$$

Substituting in Eq. (2.140) for W_C and solving for f_x , we find

$$f_x = -\frac{d}{dx} \{E - I_0 \cos \omega_{r_x} t [L_{yzz}(I + I_0 \cos \omega_{r_x} t) + L_{y\bar{z}\bar{x}}(I + I_0 \cos \omega_{r_x} t - i_{r_x})]\}. \quad (2.142)$$

Thus we see that the proper potential energy of the sensing circuit is

$$V_{r_x} = E - I_0 \cos \omega_{r_x} t [L_{yzz}(I + I_0 \cos \omega_{r_x} t) + L_{y\bar{z}\bar{x}}(I + I_0 \cos \omega_{r_x} t - i_{r_x})]. \quad (2.143)$$

Combining like terms and simplifying, we find

$$V_{r_x} = \frac{1}{2}(L_{\bar{y}z\bar{x}} + L_{yzz} + L_{\bar{y}z\bar{x}} + L_{y\bar{z}\bar{x}})I^2 - \frac{1}{2}(L_{yzz} + L_{y\bar{z}\bar{x}})I_0^2 \cos^2 \omega_{r_x} t \\ + \frac{1}{2}(L_{\bar{y}z\bar{x}} + L_{y\bar{z}\bar{x}} + L_{SQ} + 5L_S)i_{r_x}^2 - (L_{\bar{y}z\bar{x}} + L_{y\bar{z}\bar{x}})Ii_{r_x}. \quad (2.144)$$

Solving Eqs. (2.128) and (2.129) for I , substituting I , i_{r_x} , and Eqs. (2.113), (2.108), (2.110), and (2.115) for $L_{\bar{y}z\bar{x}}$, L_{yzz} , $L_{\bar{y}z\bar{x}}$, and $L_{y\bar{z}\bar{x}}$, respectively, into the above equation, we find, after expanding to second order in r and θ ,

$$V_{r_x} = \frac{1}{4}I_0^2(1 + \cos 2\omega_{r_x} t) \left[-L_S + \left(\frac{\Lambda_S^2}{L_{SQ} + 6L_S} + \frac{\gamma_S}{2} \right) r_x^2 \right. \\ \left. + \left(\frac{c^2 \Lambda_S^2}{L_S} \right) \theta_y^2 + \frac{1}{2} (\Lambda_S d_S + c^2 \gamma_S + \beta_S) (\theta_y^2 + \theta_z^2) \right]. \quad (2.145)$$

This shows the relationship between the square of the sensing current and the "stiffness" of the accelerometer. The sensing current oscillates at a high frequency, well above the resonance frequencies of the accelerometer, and it is an excellent approximation in practice to ignore the time varying portion of the potential.

Similar analysis of the r_y , r_z , θ_x , θ_y , and θ_z gives

$$V_{r_y} = \frac{1}{4}I_0^2(1 + \cos 2\omega_{r_y} t) \left[-L_S + \left(\frac{\Lambda_S^2}{L_{SQ} + 6L_S} + \frac{\gamma_S}{2} \right) r_y^2 \right. \\ \left. + \left(\frac{c^2 \Lambda_S^2}{L_S} \right) \theta_z^2 + \frac{1}{2} (\Lambda_S d_S + c^2 \gamma_S + \beta_S) (\theta_x^2 + \theta_z^2) \right], \quad (2.146)$$

$$V_{r_z} = \frac{1}{4}I_0^2(1 + \cos 2\omega_{r_z} t) \left[-L_S + \left(\frac{\Lambda_S^2}{L_{SQ} + 6L_S} + \frac{\gamma_S}{2} \right) r_z^2 \right. \\ \left. + \left(\frac{c^2 \Lambda_S^2}{L_S} \right) \theta_x^2 + \frac{1}{2} (\Lambda_S d_S + c^2 \gamma_S + \beta_S) (\theta_x^2 + \theta_y^2) \right], \quad (2.147)$$

$$V_{\theta_x} = \frac{1}{4}I_0^2(1 + \cos 2\omega_{\theta_x} t) \left[-L_S + \left(\frac{c^2 \Lambda_S^2}{L_{SQ} + 6L_S} \right) \theta_x^2 \right. \\ \left. + \left(\frac{c^2 \Lambda_S^2}{L_S} \right) \theta_y^2 + \frac{1}{2} (\Lambda_S d_S + c^2 \gamma_S + \beta_S) (\theta_x^2 + \theta_y^2) + \frac{\gamma_S}{2} r_x^2 \right], \quad (2.148)$$

$$V_{\theta_y} = \frac{1}{4}I_0^2(1 + \cos 2\omega_{\theta_y} t) \left[-L_S + \left(\frac{c^2 \Lambda_S^2}{L_{SQ} + 6L_S} \right) \theta_y^2 \right. \\ \left. + \left(\frac{c^2 \Lambda_S^2}{L_S} \right) \theta_z^2 + \frac{1}{2} (\Lambda_S d_S + c^2 \gamma_S + \beta_S) (\theta_y^2 + \theta_z^2) + \frac{\gamma_S}{2} r_y^2 \right], \quad (2.149)$$

$$V_{\theta_z} = \frac{1}{4}I_0^2(1 + \cos 2\omega_{\theta_z} t) \left[-L_S + \left(\frac{c^2 \Lambda_S^2}{L_{SQ} + 6L_S} \right) \theta_z^2 \right.$$

$$+ \left(\frac{c^2 \Lambda_S^2}{L_S} \right) \theta_x^2 + \frac{1}{2} \left(\Lambda_S d_S + c^2 \gamma_S + \beta_S \right) (\theta_x^2 + \theta_z^2) + \frac{\gamma_S}{2} r_y^2 \Big]. \quad (2.150)$$

In our analysis up to this point, we have driven all sensing circuits with the same magnitude of sensing current, I_0 . It is desirable to separate the effects of the linear and angular sensing circuits by driving each with a different magnitude of oscillating current. Thus, we will drive all three linear circuits with an oscillating current of magnitude I_r , and all three angular circuits with an oscillating current of magnitude I_θ . The total potential derived from all six sensing circuits, V_S , is then

$$\begin{aligned} V_S = & -\frac{3}{4}(I_r^2 + I_\theta^2)L_S + \frac{1}{4} \left[I_r^2 \frac{\Lambda_S^2}{L_{SQ} + 6L_S} + (I_r^2 + I_\theta^2) \frac{\gamma_S}{2} \right] (r_x^2 + r_y^2 + r_z^2) \\ & + \frac{1}{4} \left[(I_r^2 + I_\theta^2) \left(\frac{c^2 \Lambda_S^2}{L_S} + \Lambda_S d_S + c^2 \gamma_S + \beta_S \right) + I_\theta^2 \frac{c^2 \Lambda_S^2}{L_{SQ} + 6L_S} \right] (\theta_x^2 + \theta_y^2 + \theta_z^2), \end{aligned} \quad (2.151)$$

where we have dropped the time dependent portion of the potential.

The complete potential for the SSA is, from Eqs. (2.127) and (2.151),

$$\begin{aligned} V \equiv V_L + V_S = & V_0 + 2(I_-^2 - I_+^2)\Lambda_L(r_x + r_y + r_z) \\ & + 2(I_-^2 - I_+^2)\Lambda_L[\theta_x(r_z - r_y) + \theta_y(r_x - r_z) + \theta_z(r_y - r_x)] \\ & + 2 \left[I_-^2 \frac{\Lambda_L^2}{L_L} + I_+^2 \left(\frac{4\Lambda_L^2}{4L_L + L} + \frac{\gamma_L}{2} \right) \right] (r_x^2 + r_y^2 + r_z^2) \\ & + \frac{1}{4} \left[I_r^2 \frac{\Lambda_S^2}{L_{SQ} + 6L_S} + (I_r^2 + I_\theta^2) \frac{\gamma_S}{2} \right] (r_x^2 + r_y^2 + r_z^2) \\ & + \left[2(I_+^2 + I_-^2) (\Lambda_L d_L + c^2 \gamma_L + \beta_L) + 2I_-^2 \frac{c^2 \Lambda_L^2}{L_L + L} \right] (\theta_x^2 + \theta_y^2 + \theta_z^2) \\ & + \frac{1}{4} \left[(I_r^2 + I_\theta^2) \left(\frac{c^2 \Lambda_S^2}{L_S} + \Lambda_S d_S + c^2 \gamma_S + \beta_S \right) + I_\theta^2 \frac{c^2 \Lambda_S^2}{L_{SQ} + 6L_S} \right] (\theta_x^2 + \theta_y^2 + \theta_z^2), \end{aligned} \quad (2.152)$$

where

$$V_0 \equiv \frac{3}{2}(4L_L + L)I_+^2 + 6I_-^2 L_L - \frac{3}{4}(I_r^2 + I_\theta^2)L_S. \quad (2.153)$$

We can rewrite the potential V , by defining

$$f_{DC} \equiv 2(I_+^2 - I_-^2)\Lambda_L, \quad (2.154)$$

$$k_S \equiv \frac{1}{2} \left[I_r^2 \frac{\Lambda_S^2}{L_{SQ} + 6L_S} + (I_r^2 + I_\theta^2) \frac{\gamma_S}{2} \right], \quad (2.155)$$

$$k_L \equiv 4 \left[I_-^2 \frac{\Lambda_L^2}{L_L} + I_+^2 \left(\frac{4\Lambda_L^2}{4L_L + L} + \frac{\gamma_L}{2} \right) \right], \quad (2.156)$$

$$\tau_L \equiv 4 \left[(I_+^2 + I_-^2) (\Lambda_L d_L + c^2 \gamma_L + \beta_L) + I_-^2 \frac{c^2 \Lambda_L^2}{L_L + L} \right], \quad (2.157)$$

$$\tau_S \equiv \frac{1}{2} \left\{ (I_r^2 + I_\theta^2) \left[\frac{c^2 \Lambda_S^2}{L_S} + \Lambda_S d_S + c^2 \gamma_S + \beta_S \right] + I_\theta^2 \frac{c^2 \Lambda_S^2}{L_{SQ} + 6L_S} \right\}. \quad (2.158)$$

We find, after substituting these expressions into our potential V ,

$$\begin{aligned} V = & V_0 - f_{DC}(r_x + r_y + r_z) \\ & - f_{DC} [\theta_x(r_z - r_y) + \theta_y(r_x - r_z) + \theta_z(r_y - r_x)] \\ & + \frac{1}{2}(k_L + k_S)(r_x^2 + r_y^2 + r_z^2) + \frac{1}{2}(\tau_L + \tau_S)(\theta_x^2 + \theta_y^2 + \theta_z^2). \end{aligned} \quad (2.159)$$

It is immediately clear how each portion of the potential contributes to the dynamics of the SSA: k_L , and k_S are the linear spring constants generated by the levitation and sensing circuitry, τ_L , and τ_S are the angular spring constants generated by the levitation and sensing circuitry, f_{DC} is the DC force generated by the levitation circuitry, and f_{DC} is also a measure of the cross coupling between the linear and angular levitation circuits.

2.4 Six-Axis Accelerometer Transfer Functions

In the last two sections, we have derived the equations of motion for the SSA, the sensitivity of the sensing circuitry to changes in the position of the proof mass, and the potential energy of the magnetic springs which levitate the proof mass. In this section, we will combine all the information in the previous sections and describe the SSA in terms of transfer functions relating acceleration to displacement and displacement to output current. This will enable us to describe the fundamental noise of the accelerometer and the potential sensitivity of the SSA in the next section.

A displacement of the proof mass in the SSA away from equilibrium is echoed by a current response i , in the input coil of the SQUID amplifier. The six transfer functions relating the output current of the SSA to the position and orientation of the proof mass can be derived from Eqs. (2.131) through (2.136). We find:

$$H_{r_x i} \equiv \frac{i_x}{r_x} = I_r \cos \omega_{r_x} t \frac{\Lambda_S}{L_{SQ} + 6L_S}, \quad (2.160)$$

$$H_{r_y i} \equiv \frac{i_y}{r_y} = I_r \cos \omega_{r_y} t \frac{\Lambda_S}{L_{SQ} + 6L_S}, \quad (2.161)$$

$$H_{r_z i} \equiv \frac{i_z}{r_z} = I_r \cos \omega_{r_z} t \frac{\Lambda_S}{L_{SQ} + 6L_S}, \quad (2.162)$$

$$H_{\theta_x i} \equiv \frac{i_{\theta_x}}{\theta_x} = I_\theta \cos \omega_{\theta_x} t \frac{c\Lambda_S}{L_{SQ} + 6L_S}, \quad (2.163)$$

$$H_{\theta_y i} \equiv \frac{i_{\theta_y}}{\theta_y} = I_\theta \cos \omega_{\theta_y} t \frac{c\Lambda_S}{L_{SQ} + 6L_S}, \quad (2.164)$$

$$H_{\theta_z i} \equiv \frac{i_{\theta_z}}{\theta_z} = I_\theta \cos \omega_{\theta_z} t \frac{c\Lambda_S}{L_{SQ} + 6L_S}, \quad (2.165)$$

where we have dropped all second order terms, and replaced I_0 by I_r and I_θ in the linear and angular sensing circuits, respectively.

An acceleration of the SSA is echoed by a displacement of the proof mass. This displacement of the proof mass is described by the equations of motion for the SSA, Eq. (2.69) for the linear degrees of freedom, and Eqs. (2.86), (2.87), and (2.88) for the angular degrees of freedom. Substituting the potential, V , from Eq. (2.159) into these equations, we find:

$$\ddot{r}_x + \omega_r^2 r_x = \frac{f_{DC}}{m} + \frac{f_{DC}}{m}(\theta_y - \theta_z) + a_x^E, \quad (2.166)$$

$$\ddot{r}_y + \omega_r^2 r_y = \frac{f_{DC}}{m} + \frac{f_{DC}}{m}(\theta_z - \theta_x) + a_y^E, \quad (2.167)$$

$$\ddot{r}_z + \omega_r^2 r_z = \frac{f_{DC}}{m} + \frac{f_{DC}}{m}(\theta_x - \theta_y) + a_z^E, \quad (2.168)$$

$$\ddot{\theta}_x + \omega_\theta^2 \theta_x = \frac{f_{DC}}{I}(r_z - r_y) + \dot{\omega}_1^H + \theta_y \dot{\omega}_3^H - \omega_3^H \dot{\theta}_y + \omega_2^H \dot{\theta}_z, \quad (2.169)$$

$$\ddot{\theta}_y + \omega_\theta^2 \theta_y = \frac{f_{DC}}{I}(r_x - r_z) + \dot{\omega}_2^H - \theta_x \dot{\omega}_3^H - \omega_1^H \dot{\theta}_z + \omega_3^H \dot{\theta}_x, \quad (2.170)$$

$$\ddot{\theta}_z + \omega_\theta^2 \theta_z = \frac{f_{DC}}{I}(r_y - r_x) + \dot{\omega}_3^H + \theta_x \dot{\omega}_2^H - \omega_2^H \dot{\theta}_x + \omega_1^H \dot{\theta}_y, \quad (2.171)$$

where we have dropped the superscript from r^P , dropped all second order terms, and defined

$$\omega_r^2 \equiv \frac{k_L + k_S}{m}, \quad (2.172)$$

$$\omega_\theta^2 \equiv \frac{\tau_L + \tau_S}{I}. \quad (2.173)$$

The SSA is orientated in the “umbrella” orientation so that all three axes make the same angle with the vertical, and the acceleration of gravity is applied equally to the three axes. With the SSA in the “umbrella” orientation on the surface of the earth,

levitation currents are stored in the SSA so that

$$\frac{f_{DC}}{m} = \frac{gE}{\sqrt{3}}. \quad (2.174)$$

This levitation force cancels the DC component of the external acceleration, a^E . Equations (2.166) through (2.171) can be rewritten:

$$\ddot{r}_i + \omega_r^2 r_i = a_i, \quad (2.175)$$

$$\ddot{\theta}_i + \omega_\theta^2 \theta_i = \alpha_i, \quad (2.176)$$

where

$$a_x \equiv a_x^E + \frac{gE}{\sqrt{3}} + \frac{gE}{\sqrt{3}}(\theta_y - \theta_z), \quad (2.177)$$

$$a_y \equiv a_y^E + \frac{gE}{\sqrt{3}} + \frac{gE}{\sqrt{3}}(\theta_z - \theta_x), \quad (2.178)$$

$$a_z \equiv a_z^E + \frac{gE}{\sqrt{3}} + \frac{gE}{\sqrt{3}}(\theta_x - \theta_y), \quad (2.179)$$

$$\alpha_x \equiv \frac{gEm}{\sqrt{3}I}(r_z - r_y) + \dot{\omega}_1^H + \theta_y \dot{\omega}_3^H - \omega_3^H \dot{\theta}_y + \omega_2^H \dot{\theta}_z, \quad (2.180)$$

$$\alpha_y \equiv \frac{gEm}{\sqrt{3}I}(r_x - r_z) + \dot{\omega}_2^H - \theta_x \dot{\omega}_3^H - \omega_1^H \dot{\theta}_z + \omega_3^H \dot{\theta}_x, \quad (2.181)$$

$$\alpha_z \equiv \frac{gEm}{\sqrt{3}I}(r_y - r_x) + \dot{\omega}_3^H + \theta_x \dot{\omega}_2^H - \omega_2^H \dot{\theta}_x + \omega_1^H \dot{\theta}_y. \quad (2.182)$$

Up until this point, we have assumed that no damping of the motion of the proof mass occurs. In reality, the superconducting circuitry and the experimental support structure force the Q of the modes in the SSA to be finite. The damping of the proof mass in the linear degrees of freedom can be modeled by the addition of a velocity dependent force, $\dot{r}\omega_r/Q_r$ to the equations of motion for the SSA, where Q_r is the quality of the linear resonance. The damping of the proof mass in the angular degrees of freedom can be similarly modeled by the addition of a velocity dependent force, $\dot{\theta}\omega_\theta/Q_\theta$ to the angular equations of motion for the SSA, where Q_θ is the quality of the angular resonances. Adding these additional terms to Eqs. (2.175) and (2.176), we find

$$\ddot{r}_i + \frac{\omega_r}{Q_r} \dot{r}_i + \omega_r^2 r_i = a_i. \quad (2.183)$$

$$\ddot{\theta}_i + \frac{\omega_\theta}{Q_\theta} \dot{\theta}_i + \omega_\theta^2 \theta_i = \alpha_i. \quad (2.184)$$

These equations of motion can be written in the frequency domain by defining

$$r_i(t) \equiv r_i(\omega)e^{i\omega t}, \quad (2.185)$$

$$a_i(t) \equiv a_i(\omega)e^{i\omega t}, \quad (2.186)$$

$$\theta_i(t) \equiv \theta_i(\omega)e^{i\omega t}, \quad (2.187)$$

$$\alpha_i(t) \equiv \alpha_i(\omega)e^{i\omega t}. \quad (2.188)$$

Substituting these definitions into our equations of motion, and solving for the ratios, $r_i(\omega)/a_i(\omega)$ and $\theta_i(\omega)/\alpha_i(\omega)$, we find

$$H_{ax} \equiv \frac{r_x(\omega)}{a_x(\omega)} = \frac{1}{\omega_r^2 + i\omega_r\omega/Q_r - \omega^2}, \quad (2.189)$$

$$H_{ay} \equiv \frac{r_y(\omega)}{a_y(\omega)} = \frac{1}{\omega_r^2 + i\omega_r\omega/Q_r - \omega^2}, \quad (2.190)$$

$$H_{az} \equiv \frac{r_z(\omega)}{a_z(\omega)} = \frac{1}{\omega_r^2 + i\omega_r\omega/Q_r - \omega^2}, \quad (2.191)$$

$$H_{\alpha\theta_x} \equiv \frac{\theta_x(\omega)}{\alpha_x(\omega)} = \frac{1}{\omega_\theta^2 + i\omega_\theta\omega/Q_\theta - \omega^2}. \quad (2.192)$$

$$H_{\alpha\theta_y} \equiv \frac{\theta_y(\omega)}{\alpha_y(\omega)} = \frac{1}{\omega_\theta^2 + i\omega_\theta\omega/Q_\theta - \omega^2}. \quad (2.193)$$

$$H_{\alpha\theta_z} \equiv \frac{\theta_z(\omega)}{\alpha_z(\omega)} = \frac{1}{\omega_\theta^2 + i\omega_\theta\omega/Q_\theta - \omega^2}. \quad (2.194)$$

The transfer functions relating acceleration to displacement, Eqs. (2.189) through (2.194), and displacement to output current, Eqs. (2.160) through (2.165), can be combined to define the transfer functions relating acceleration to output current:

$$H_{a_x i} \equiv \frac{i_x(\omega)}{a_x(\omega)} = I_r \cos\omega_{r_x} t \frac{\Lambda_S}{LSQ + 6LS} \frac{1}{\omega_r^2 + i\omega_r\omega/Q_r - \omega^2}, \quad (2.195)$$

$$H_{a_y i} \equiv \frac{i_y(\omega)}{a_y(\omega)} = I_r \cos\omega_{r_y} t \frac{\Lambda_S}{LSQ + 6LS} \frac{1}{\omega_r^2 + i\omega_r\omega/Q_r - \omega^2}, \quad (2.196)$$

$$H_{a_z i} \equiv \frac{i_z(\omega)}{a_z(\omega)} = I_r \cos\omega_{r_z} t \frac{\Lambda_S}{LSQ + 6LS} \frac{1}{\omega_r^2 + i\omega_r\omega/Q_r - \omega^2}, \quad (2.197)$$

$$H_{\alpha_x i} \equiv \frac{i_{\theta_x}(\omega)}{\alpha_x(\omega)} = I_\theta \cos\omega_{\theta_x} t \frac{c\Lambda_S}{LSQ + 6LS} \frac{1}{\omega_\theta^2 + i\omega_\theta\omega/Q_\theta - \omega^2}, \quad (2.198)$$

$$H_{\alpha_y i} \equiv \frac{i_{\theta_y}(\omega)}{\alpha_y(\omega)} = I_\theta \cos\omega_{\theta_y} t \frac{c\Lambda_S}{LSQ + 6LS} \frac{1}{\omega_\theta^2 + i\omega_\theta\omega/Q_\theta - \omega^2}, \quad (2.199)$$

$$H_{\alpha_z i} \equiv \frac{i_{\theta_z}(\omega)}{\alpha_z(\omega)} = I_\theta \cos\omega_{\theta_z} t \frac{c\Lambda_S}{LSQ + 6LS} \frac{1}{\omega_\theta^2 + i\omega_\theta\omega/Q_\theta - \omega^2}. \quad (2.200)$$

2.5 Fundamental Noise of the Accelerometer

The fundamental noise of the SSA can be described in terms of the equivalent acceleration noise, a^N and α^N , applied to the proof mass. This equivalent input accelera-

tion noise is generated by two separate processes in the SSA. The first, Brownian motion noise, actually generates acceleration noise in the form of thermodynamic fluctuations. The second, SQUID amplifier noise, adds noise to the measured signal, which is reflected in the output as an equivalent input acceleration.

Since the processes in the SSA are stationary, we can equate the auto correlation

$$R_{xx}(\tau) \equiv \langle x(t)x^*(t+\tau) \rangle \quad (2.201)$$

of a signal from the SSA, $x(t)$, to a time average:

$$R_{xx}(\tau) = \lim_{T \rightarrow \infty} \frac{1}{2T} \int_{-T}^T x(t)x^*(t+\tau)dt. \quad (2.202)$$

The Wiener-Khintchine theorem [14,15] allows us, in turn, to relate this to the power spectrum density:

$$S_x(\omega) = \int_{-\infty}^{\infty} R_{xx}(\tau)e^{-i\omega\tau}d\tau, \quad (2.203)$$

$$R_{xx}(\tau) = \frac{1}{2\pi} \int_{-\infty}^{\infty} S_x(\omega)e^{i\omega\tau}d\omega. \quad (2.204)$$

2.5.1 Transducer Brownian Motion Noise

The Brownian motion of the SSA at a temperature T appears at the proof mass as three linear and three angular noise terms, $a_i^T(\omega)$ and $\alpha_i^T(\omega)$, respectively. By applying $a_i^T(\omega)$ and $\alpha_i^T(\omega)$ to the transfer functions relating the position and orientation of the SSA to acceleration, Eqs. (2.189) through (2.194), we can relate the position and orientation of the SSA to the Brownian motion noise. This will allow us to compute the average potential energy of each mode, and in turn, by applying the equipartition theorem, compute the spectral density of the Brownian noise.

The transfer functions relating the position of the SSA to the applied Brownian motion noise are, from Eqs. (2.189) through (2.194),

$$r_i(\omega) = \frac{a_i^T(\omega)}{\omega_r^2 + i\omega\omega_r/Q_r - \omega^2}, \quad (2.205)$$

$$\theta_i(\omega) = \frac{\alpha_i^T(\omega)}{\omega_\theta^2 + i\omega\omega_\theta/Q_\theta - \omega^2}. \quad (2.206)$$

The thermal energy in each of the linear modes of the SSA can now be computed:

$$k_B T = m\omega_r^2 \langle r_i^2(t) \rangle$$

$$\begin{aligned}
&= m\omega_r^2 R_{r,r}(0) \\
&= m\omega_r^2 \frac{1}{2\pi} \int_{-\infty}^{\infty} S_r(\omega) d\omega \\
&= m\omega_r^2 \frac{1}{2\pi} \int_{-\infty}^{\infty} \frac{S_{a_i^T}(\omega)}{|\omega_r^2 + i\omega\omega_r/Q_r - \omega^2|^2} d\omega, \tag{2.207}
\end{aligned}$$

where k_B is Boltzmann's constant and we have used the fact, from Eqs. (2.205), (2.202), and (2.203), that

$$S_r(\omega) = \frac{S_{a_i^T}(\omega)}{|\omega_r^2 + i\omega\omega_r/Q_r - \omega^2|^2}. \tag{2.208}$$

Since the thermal fluctuations are white in character, $S_{a_i^T}(\omega)$ is a constant, and we can perform the integral immediately. We find

$$k_B T = \frac{mQ_r}{2\omega_r} S_{a_i^T}, \tag{2.209}$$

or

$$S_{a_i^T} = \frac{2k_B T \omega_r}{mQ_r}. \tag{2.210}$$

This equation is the mechanical analog of the Nyquist equation. The power spectral density for each of the angular modes of the SSA can similarly be computed:

$$S_{\alpha_i^T} = \frac{2k_B T \omega_\theta}{IQ_\theta}. \tag{2.211}$$

2.5.2 SQUID Amplifier Noise

A noise model of the rf SQUID can be found in [6,7]. In this model, the optimum source impedance is much smaller than the input impedance ωL_{SQ} . Because of this impedance mismatch, the noise of the SQUID is dominated by current noise, $S_I(\omega)$, and can be characterized by an "input energy sensitivity":

$$E_S(\omega) \equiv \frac{1}{2} L_{SQ} S_I(\omega). \tag{2.212}$$

2.5.3 Potential Sensitivity

The output of the SSA is modulated by the applied carrier frequency in each of the six degrees of freedom and each of these signals must be separately demodulated by a lock-in amplifier. This process is represented schematically in Fig. 2.9, for the τ_x degree of freedom. In order to fully understand how each fundamental noise source contributes

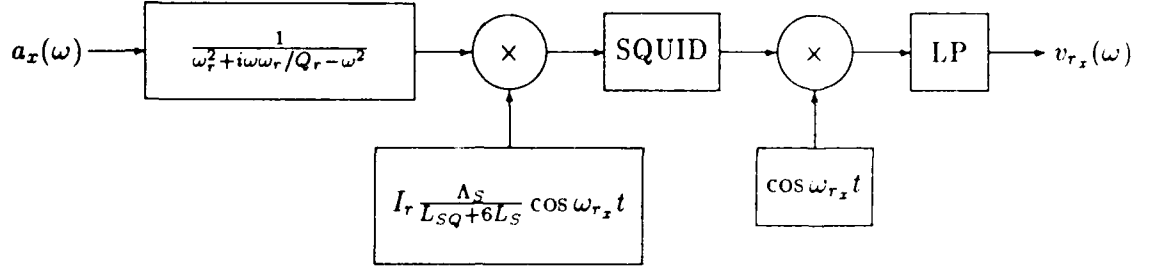


Figure 2.9. A schematic illustrating detection of acceleration in the SSA: r_x degree of freedom.

to the total noise of the SSA, we will travel through each stage of the process for the r_x degree of freedom.

Any acceleration signal, $a_x(t)$, that drives the the SSA must compete with the Brownian motion, $a_x^T(t)$. Thus the combined power spectral density which appears at the input to the block diagram in Fig. 2.9 is

$$S_{a_x}(\omega) + S_{a_x^T}. \quad (2.213)$$

This spectral density is translated by the frequency response of the SSA into a displacement spectral density:

$$S_{r_x}(\omega) = \frac{S_{a_x}(\omega) + S_{a_x^T}}{|\omega_r^2 + i\omega\omega_r/Q_r - \omega^2|^2}. \quad (2.214)$$

This signal is modulated and appears at the input to the SQUID amplifier. Modulation of the r_x signal, Eq. (2.160), relates the spectral density, S_{i_x} , at the input to the SQUID, to the spectral density S_{r_x} :

$$S_{i_x}(\omega) = \frac{1}{4} \left(\frac{I_r \Lambda_S}{L_S Q + 6 L_S} \right)^2 [S_{r_x}(\omega - \omega_{r_x}) + S_{r_x}(\omega + \omega_{r_x})]. \quad (2.215)$$

Combining this with Eq. (2.214), we find

$$S_{i_x}(\omega) = \frac{1}{4} \left(\frac{I_r \Lambda_S}{L_S Q + 6 L_S} \right)^2 \left[\frac{S_{a_x}(\omega - \omega_{r_x}) + S_{a_x^T}}{|\omega_r^2 + i(\omega - \omega_{r_x})\omega_r/Q_r - (\omega - \omega_{r_x})^2|^2} + \frac{S_{a_x}(\omega + \omega_{r_x}) + S_{a_x^T}}{|\omega_r^2 + i(\omega + \omega_{r_x})\omega_r/Q_r - (\omega + \omega_{r_x})^2|^2} \right] + S_I, \quad (2.216)$$

where we have added the input noise spectral density from the SQUID amplifier, S_I .

This signal is then amplified by the SQUID and demodulated. The power spectral density, just before the low pass filter in Fig. 2.9, is

$$S_{v_x}(\omega) = \frac{1}{4} G^2 [S_{i_x}(\omega - \omega_{r_x}) + S_{i_x}(\omega + \omega_{r_x})], \quad (2.217)$$

where G is the gain of the SQUID in V/A. Substituting Eq. (2.216), we find

$$S_{v_x}(\omega) = \frac{1}{4}G^2 \left\{ 2S_I + \frac{1}{4} \left(\frac{I_r \Lambda_S}{L_{SQ} + 6L_S} \right)^2 \left[\frac{S_{a_x}(\omega - 2\omega_{rx}) + S_{a_x^T}}{|\omega_r^2 + i(\omega - 2\omega_{rx})\omega_r/Q_r - (\omega - 2\omega_{rx})^2|^2} \right. \right. \\ \left. \left. + \frac{S_{a_x}(\omega + 2\omega_{rx}) + S_{a_x^T}}{|\omega_r^2 + i(\omega + 2\omega_{rx})\omega_r/Q_r - (\omega + 2\omega_{rx})^2|^2} + 4 \frac{S_{a_x}(\omega) + S_{a_x^T}}{|\omega_r^2 + i\omega\omega_r/Q_r - \omega^2|^2} \right] \right\}. \quad (2.218)$$

Note that a 4, not a 2, appears in front of the last term inside the brackets, because the signals are adding coherently. Since the resonances of the SSA are of a much lower frequency than ω_{rx} , the first two terms within the brackets on the right hand side of Eq. (2.218) can be neglected, and the final output spectral density is

$$S_{v_x}(\omega) = \frac{1}{4}G^2 \left\{ 2S_I + \left(\frac{I_r \Lambda_S}{L_{SQ} + 6L_S} \right)^2 \left[\frac{S_{a_x}(\omega) + S_{a_x^T}}{|\omega_r^2 + i\omega\omega_r/Q_r - \omega^2|^2} \right] \right\}. \quad (2.219)$$

If we represent the SQUID amplifier noise as an equivalent acceleration noise, a_x^{SQ} , acting on the proof mass, then Eq. (2.219) can be rewritten:

$$S_{v_x}(\omega) = \frac{1}{4}G^2 \left(\frac{I_r \Lambda_S}{L_{SQ} + 6L_S} \right)^2 \left[\frac{S_{a_x^{SQ}}(\omega) + S_{a_x}(\omega) + S_{a_x^T}}{|\omega_r^2 + i\omega\omega_r/Q_r - \omega^2|^2} \right], \quad (2.220)$$

where

$$S_{a_x^{SQ}}(\omega) \equiv 2 \left(\frac{L_{SQ} + 6L_S}{I_r \Lambda_S} \right)^2 |\omega_r^2 + i\omega\omega_r/Q_r - \omega^2|^2 S_I. \quad (2.221)$$

Thus the minimum detectable acceleration spectral density is, from Eq. (2.220),

$$S_{a_x}(\omega) \geq S_{a_x^{SQ}}(\omega) + S_{a_x^T} \\ \geq 4 \left(\frac{L_{SQ} + 6L_S}{I_r \Lambda_S} \right)^2 |\omega_r^2 + i\omega\omega_r/Q_r - \omega^2|^2 \frac{E_S}{L_{SQ}} + \frac{2k_B T \omega_r}{mQ_r}, \quad (2.222)$$

where we have substituted Eqs. (2.221), (2.210), and (2.212).

The power spectral density extends over both positive and negative frequencies, and in order to compute the noise power, P_Ω , in any frequency band, Ω , we must include both the negative and positive frequencies. Thus, it is convenient to define a one sided power spectral density, $P(\omega)$:

$$P(\omega) \equiv [S(\omega) + S(-\omega)], \quad (2.223)$$

and the power in a frequency band, Ω , is

$$P_\Omega = \int_\Omega P(2\pi f) df. \quad (2.224)$$

The minimum detectable acceleration spectral density, $S_{a_x}(\omega)$, is then equivalent to

$$P_{a_x}(\omega) = 8 \left(\frac{LSQ + 6LS}{I_r \Lambda_S} \right)^2 \left| \omega_r^2 + i\omega\omega_r/Q_r - \omega^2 \right|^2 \frac{E_S}{LSQ} + \frac{4k_B T \omega_r}{mQ_r}. \quad (2.225)$$

For frequencies much less than the resonances of the SSA, this simplifies to

$$P_{a_x} = 8 \left(\frac{LSQ + 6LS}{I_r \Lambda_S} \right)^2 \omega_r^4 \frac{E_S}{LSQ} + \frac{4k_B T \omega_r}{mQ_r}. \quad (2.226)$$

This can be written in terms of an energy coupling coefficient, β_r :

$$\beta_r \equiv \left\langle \frac{LSQ i_x^2}{m\omega_r^2 r_x^2} \right\rangle_t, \quad (2.227)$$

where $\langle \rangle_t$ denotes a time average over one period of the carrier frequency ω_{rx} . Substituting Eq. (2.160) into our expression for β_r , we find

$$\beta_r = \frac{1}{2} \left(\frac{I_r \Lambda_S}{LSQ + 6LS} \right)^2 \frac{LSQ}{m\omega_r^2}. \quad (2.228)$$

Substituting this into the expression for the minimum detectable acceleration spectral density, Eq. (2.226), gives

$$P_{a_x} = \frac{4\omega_r}{m} \left(\frac{k_B T}{Q_r} + \frac{\omega_r E_S}{\beta_r} \right). \quad (2.229)$$

Comparing this to the minimum expression for the noise in the gravity gradiometer, it is seen that the noise from the SQUID contributes twice. This is a consequence of the demodulation which folds the two separate sidebands of the modulated signal upon each other, so that the noise in each sideband is added together. If we had used six separate SQUIDS in a more traditional DC detection scheme, we would not have suffered this penalty, but we would have lost all the benefits gained from modulation.

The coupling coefficient, β_r can be rewritten in a more compact form. If we remove the direct dependence on I_r and ω_r , by substituting Eqs. (2.155) and (2.172) into Eq. (2.228), we find

$$\beta_r = \frac{LSQ}{LSQ + 6LS} \left(\frac{k_S}{k_L + k_S} \right). \quad (2.230)$$

Thus we see that β_r can vary between 0 and $1/(1 + 6LS/LSQ)$. If Brownian noise in the SSA is dominated by SQUID noise, P_{a_x} is minimized when $k_S = k_L$, or

$$\beta_r = \frac{1}{2} \frac{LSQ}{LSQ + 6LS}. \quad (2.231)$$

This optimal coupling could be improved by inserting a superconducting transformer between the bridge circuitry and the SQUID. This would match $L_{SQ} + 6L_S$ to L_{SQ} , and β_r optimal would be 1/2.

A similar analysis of the two other linear degrees of freedom gives

$$P_{a_y} = P_{a_z} = \frac{4\omega_r}{m} \left(\frac{k_B T}{Q_r} + \frac{\omega_r E_S}{\beta_r} \right). \quad (2.232)$$

Likewise, analysis of the three angular degrees of freedom gives

$$P_{\alpha_x} = P_{\alpha_y} = P_{\alpha_z} = \frac{4\omega_\theta}{I} \left(\frac{k_B T}{Q_\theta} + \frac{\omega_\theta E_S}{\beta_\theta} \right), \quad (2.233)$$

where

$$\beta_\theta \equiv \left\langle \frac{L_{SQ} i_{\theta_x}^2}{I \omega_\theta^2 \theta_x^2} \right\rangle_t = \frac{1}{2} \left(\frac{I_\theta c \Lambda_S}{L_{SQ} + 6L_S} \right)^2 \frac{L_{SQ}}{I \omega_\theta^2}. \quad (2.234)$$

Chapter 3

Construction of the Superconducting Six-Axis Accelerometer

In the previous chapter we discussed the theory of the SSA. In this chapter we will describe the actual realization of this theory in a concrete design. In the first section, we will describe the main mechanical components that comprise the SSA: the proof mass, coil forms, coil form holders, precision mounting cube, transformers, and superconducting coils. In the second section, we will describe the superconducting circuitry. In the third section, we will examine the design of the cryostat and the suspension hardware that supports the SSA in the cryostat. In the fourth and final section, we describe the computer system, data acquisition, and interface electronics used to control the SSA.

3.1 Accelerometer Hardware

3.1.1 Mechanical Components

The primary hardware that makes up the SSA, consists of four main components: the proof mass, the titanium coil forms which hold the superconducting coils in close proximity to the proof mass, the coil form holders which align the coil forms, and a precision mounting cube which holds the coil form holders. An exploded view of the SSA is shown in Fig. 3.1.

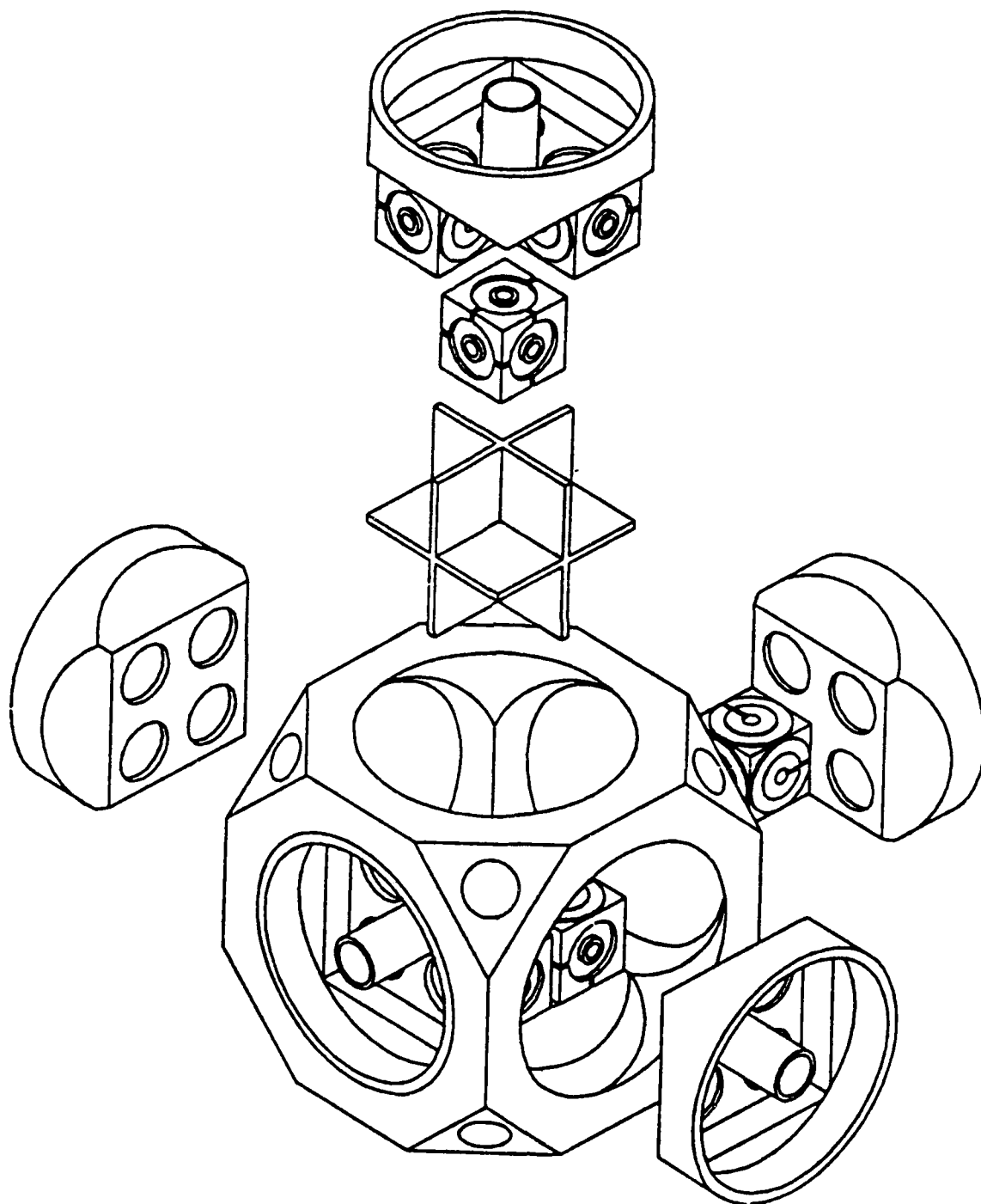


Figure 3.1. An exploded view of the SSA hardware.

The proof mass for the SSA is constructed from pure niobium (Nb). It consists of four separate plates which fit tightly together to form the final proof mass. An exploded view of this is shown in Fig. 3.2. The machining of the proof mass proceeded in four steps. In the first stage the four pieces were cut from a Nb plate. Each piece was left slightly oversized in order to maintain the precision of the final proof mass. The pieces were then heat treated in a high vacuum oven at 1800°C for 4 hours. Next all dimensions except the slots were finished using a computer controlled milling machine. The slots were then finished using an electron discharge machine (EDM). The pieces were then polished flat to a final thickness of 2.39 mm and assembled into the final proof mass. A small amount of GE 7031 varnish (General Electric Co., Schenectady, New York) was used to lock the pieces in place. The final dimensions of the proof mass are 2.784 cm on a side. The proof mass is orthogonal and flat to a part in 10^3 .

The proof mass is surrounded by eight titanium alloy cubes which hold the superconducting coils in close proximity to the proof mass. Each of the eight cubes has three surfaces which face the proof mass, and three surfaces which do not. Each of the surfaces which face away from the proof mass has a recessed pocket in which small strain relief clamps are mounted. These clamps protect the superconducting wires that connect to the superconducting coils. Each of the surfaces which face the proof mass has two flat circular regions which contain one levitation coil and one sensing coil, respectively. An isometric drawing of a coil form is shown in Fig. 3.3. Titanium was chosen as the material for the coil forms because of its strength and machinability. It was also felt that a conducting coil form would decrease the susceptibility of the superconducting circuitry to rf noise, since eddy current losses add an additional loss mechanism at high frequencies.

The coil forms are held in place by a set of six cylindrical Nb coil form holders which mount inside a precision 10.16 cm titanium cube. These six coil form holders mesh together inside the titanium cube in such a way as to form a smaller hollow Nb cube inside the titanium cube. The eight coil forms are mounted on the inside of this hollow Nb cube. Each coil form is attached to three of the six Nb coil form holders. This is possible since the six coil form holders form the six sides of the hollow Nb cube, and each coil form rests in one of the eight corners. Each of the recessed pockets in the coil forms is matched by a corresponding hole in the coil form holder. Wiring from the superconducting coils on the coil forms is routed through these holes to the large circular

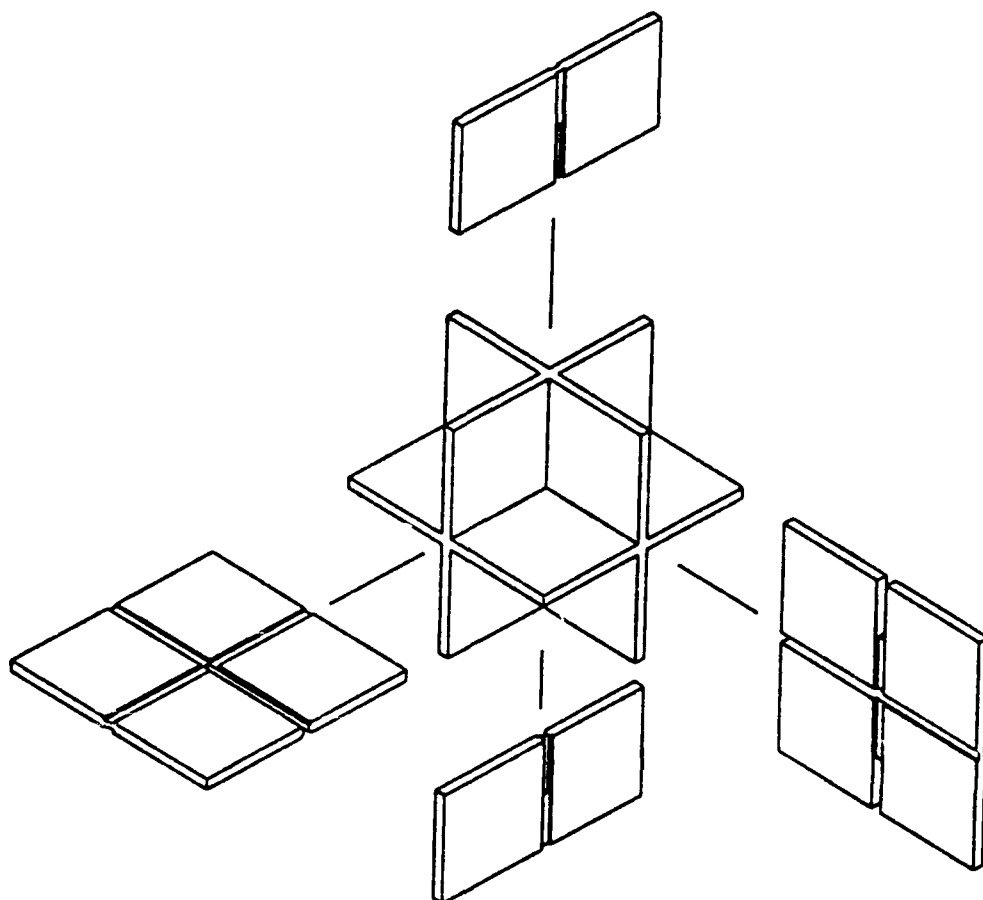


Figure 3.2. An exploded view of the SSA proofmass.

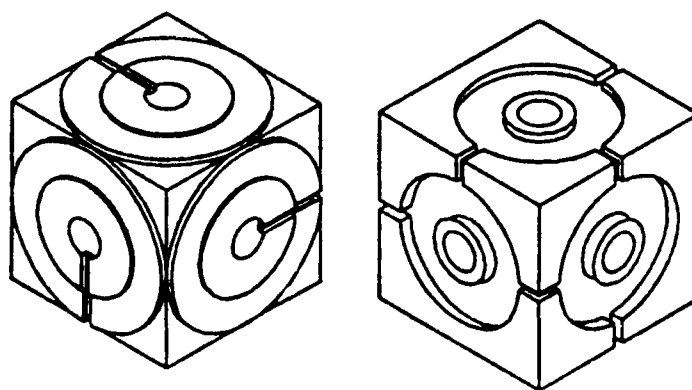


Figure 3.3. A schematic drawing of one of the coil forms in the SSA.

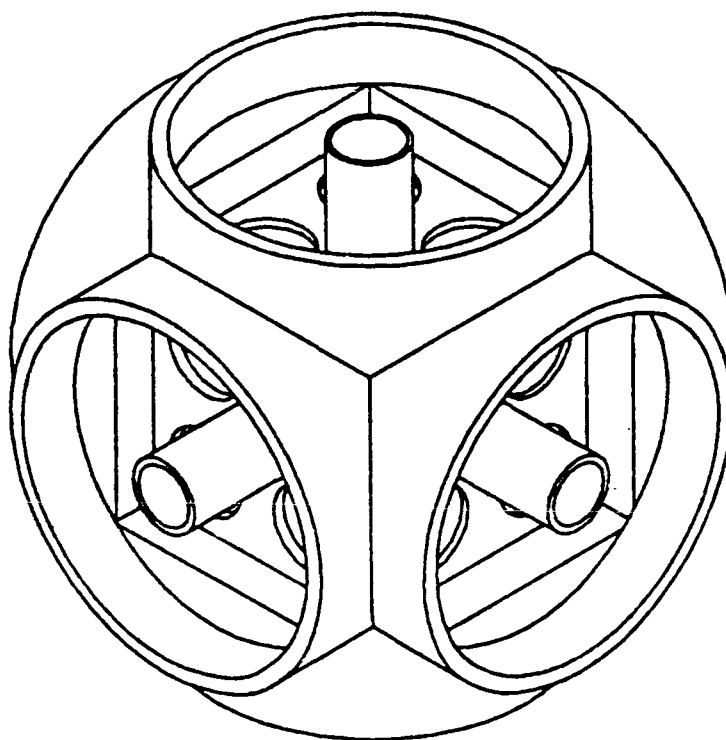


Figure 3.4. An isometric view of the six coil form holders.

pockets in the coil form holders. All the superconducting joints in the SSA are mounted in these large circular pockets. Small holes allow the superconducting wires to be routed from one pocket to another.

The cylindrical pocket at the center of each coil form holder is used to house a feedback transformer. An isometric view of the six Nb coil form holders, as they would appear inside the precision mounting cube, is shown in Fig. 3.4.

The precision titanium cube which houses the SSA is shown in Fig. 3.5. Its surfaces are flat and mutually orthogonal to better than 2 parts in 10^5 . Each of the six surfaces on the mounting cube contains a tapped bolt circle (not shown) which match the clearance holes in the accelerometers which make up the superconducting gravity gradiometer. Presently these bolt circles are used to mount Nb covers over the pockets of circuitry in the SSA, but when the SSA is integrated with the gravity gradiometer, these covers will be replaced by the six accelerometers that make up the superconducting gravity gradiometer.

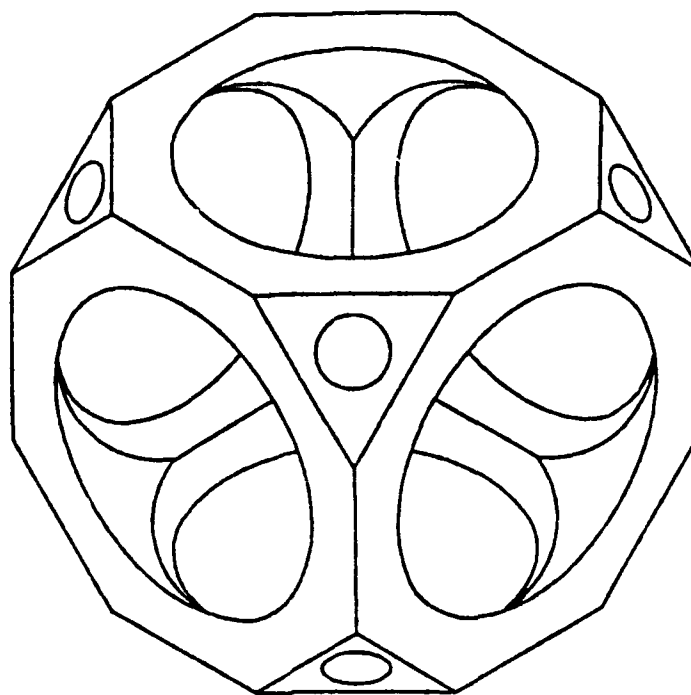


Figure 3.5. An isometric view of the precision mounting cube.

Each corner of the mounting cube has been cut perpendicular to a line passing through opposite vertices of the cube. One of these corners is used to mount the SSA in the cryostat on the suspension structure. Current and control leads enter the SSA through the other seven corners.

3.1.2 Superconducting Coils

Each surface of the coil form facing the proof mass contains two concentric superconducting coils. The outer coil is used to provide levitation and feedback to the proof mass. The inner coil is used to sense the position of the proof mass. Each coil is a spiral pancake coil wound from $76\text{ }\mu\text{m}$ diameter niobium-titanium (Nb-Ti) superconducting wire. Originally we constructed the coils in the SSA using pure Nb wire, but recent changes in the manufacturing process for pure Nb wire created reliability problems which we are currently attempting to understand. Since the SSA is constructed from 48 superconducting coils, even a small failure rate is unacceptable and we switched to tougher Nb-Ti wire. A small amount of flux creep has been observed in Nb-Ti coils

[9] and this introduces additional noise into any superconducting circuitry containing Nb-Ti coils. This is not yet a factor in the SSA since our noise is still dominated by seismic disturbances in the laboratory.

The Nb-Ti wire is insulated with ML insulation and has an overall diameter of 100 μm . Before the Nb-Ti wire is wound on the titanium coil form, the surface is carefully sanded and cleaned of all dirt and oil. The outer most coil is wound by placing a clear highly polished Plexiglas backing plate on top of the coil form. This backing plate rests on top of the surface of the inner coil and is held in place with a bolt during the winding process. There exists a small (200 μm) step between the outer and inner coil. This small step prevents the backing plate from making contact with the outer coil winding surface, and leaves room for a two layer spiral coil. A thin layer of vacuum grease is applied to the surface of the inner coil to prevent epoxy from bonding to the surface of the inner coil during the winding of the outer coil. A small radial groove from the center of the coil form to the outside allows the insertion of two small hollow Teflon tubes. The first tube runs from the center of the inner coil outwards and allows us to wind the inner coil after the outer coil is finished. The second tube guides the start of the Nb-Ti wire used in the outer coil. Winding starts from the center of the outer coil and ends after a counted number of turns. A transparent, low viscosity, epoxy, TRA-CAST BB3002 (TRA-CON, Inc., Medford, Massachusetts) is used to bond the Nb-Ti wire to the coil form. After the epoxy is set, the center bolt is removed and the backing plate is machined off, leaving a flat spiral coil consisting of two layers. The coil winding procedure used here is a modification of that described in [10,3].

After the outer coil is finished and inspected, the inner coil is wound. A hollow titanium pin with a small step (100 μm) is inserted into the center hole of the coil form. The small step prevents epoxy from running down the central hole. A small amount of vacuum grease is applied to the pin to prevent a bond from forming between the pin and the epoxy. A second clear Plexiglas backing plate with a center hole of diameter equal to the titanium pin is mounted on the pin. Careful adjustment of the spacing between the backing plate and the surface of the coil form matches this gap to the diameter of the Nb-Ti wire. A small bolt inserted through the hollow titanium pin is used to hold this spacing constant. Winding proceeds from the center of the inner coil and ends after a counted number of turns. After the epoxy is set, the center pin is removed and the backing plate is machined off, leaving a flat spiral coil consisting of a single layer.

Each of the pairs of Nb-Ti wire from the two coils is then inserted in color coded Teflon tubes. Each Teflon tube is anchored to a small stress relieving clamp mounted on the adjoining surface of the coil form that faces away from the proof mass surface.

After all parts are cleaned and inspected, the complete SSA is assembled. A photograph of the assembly is shown in Fig. 3.6. The large number of leads from the superconducting coils can be clearly seen.

3.2 Superconducting Circuitry

The superconducting joints used in the SSA are formed by spot welding two or more Nb-Ti wires to Nb-Ti foil. Each small section of foil has two or more small sections of Teflon tubing mounted at one end. These tubes keep the wire from bending at the spot weld and provide strain relief. Before the spot weld is formed, each wire is crushed flat to approximately half its original diameter. This increases the surface area of the wire in contact with the foil. Both the Nb-Ti wires and the Nb-Ti foil are polished in a diluted chemical solution of equal parts 85% H_3PO_4 , 70% HNO_3 , and 49% HF, and cleaned with distilled water to remove any residual acid. The upper and lower electrodes used in the spot welder are made of beryllium copper. The upper electrode makes contact with the flattened wire and is rectangular in shape, approximately 1 mm by 5 mm. The lower electrode is cylindrical in shape, approximately 5 mm in diameter. The contact pressure and energy settings of the spot welder are adjusted so that a test specimen, when viewed under a microscope, shows a clear fusion of the wire and the foil with little or no evaporation of material. Superconducting joints formed in this manner consistently have critical currents in excess of 8 A through many thermal cycles.

The superconducting feedback transformers used in the SSA are cylindrical in shape, with a 75 μm thick layer of brass separating the primary and the secondary. This thin brass layer forms a barrier to high frequency interference, and allows a direct connection of the feedback electronics to the SSA. Six feedback transformers are employed in all. These are mounted inside the cylindrical cavities in the six Nb coil form holders.

Six additional tuned transformers are used to connect the six inductance bridges to their room temperature oscillators. Each transformer steps up the current supplied by the room temperature oscillator by a factor of six. These transformers are cylindrical in shape and enclosed in 2.54 cm diameter Nb tubing. A thin brass layer separates the

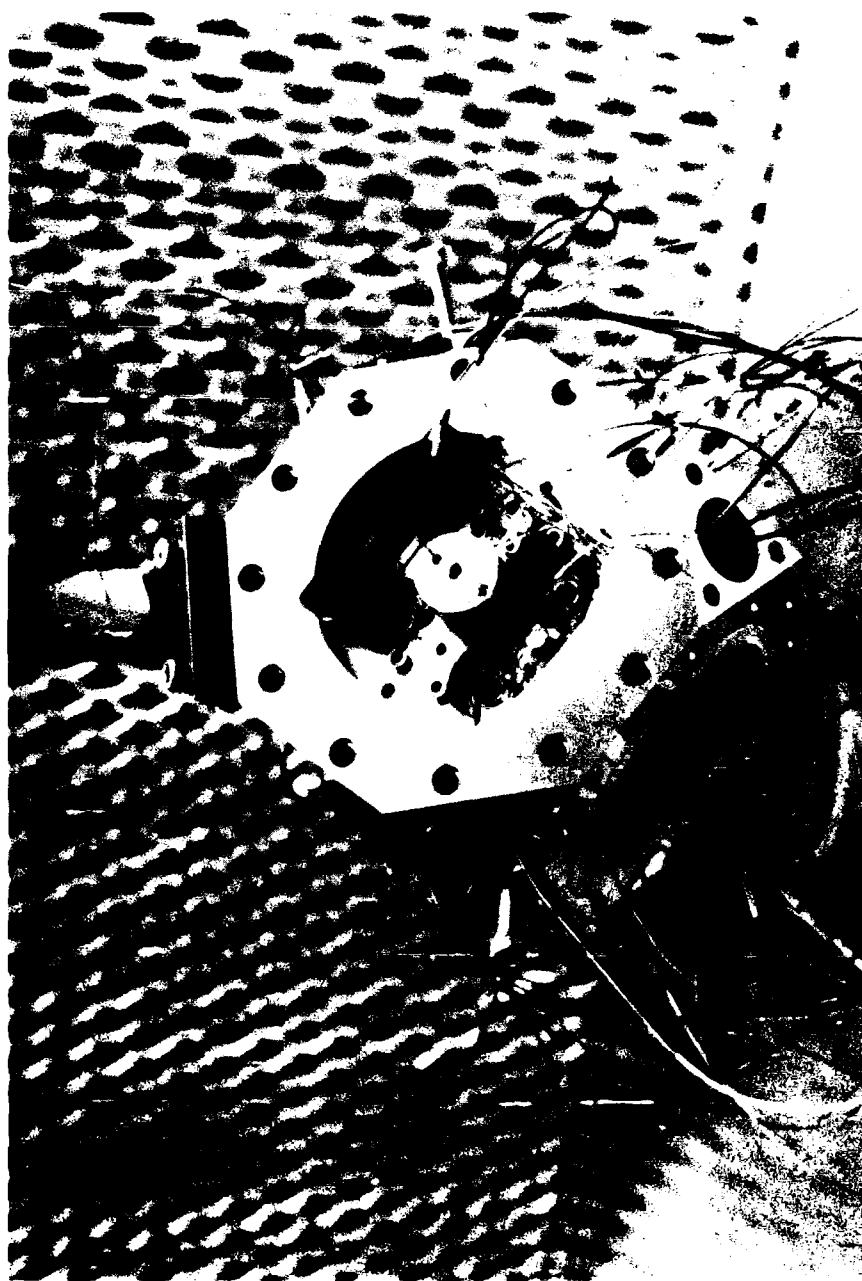


Figure 3.6. A photograph of the partially assembled SSA.

primary and the secondary, and forms a barrier to high frequency interference. This is extremely important since the secondary of each transformer is attached directly to the sensing circuitry, and very low levels of rf interference will cause the SQUID control loop to unlock. Each transformer has a polystyrene capacitor attached across the primary. This allows the transformer to resonate at a particular frequency, forming an additional noise filter for frequencies other than the resonance frequency, and providing additional current gain at that frequency. The effectiveness of this scheme is demonstrated by the ability of the SQUID to stay locked. Each of these transformers is mounted on the underside of the top of the vacuum can which houses the SSA.

Shielded heat switches are made from tiny 1/8 W, 500 Ω carbon resistors. These are specially selected carbon resistors whose resistance increases dramatically as they approach liquid helium temperatures. This provides passive feedback when the heat switch is driven by a current source. Each resistor is insulated and surrounded by a very thin layer of lead foil. This is then soldered to a lead tubing which contains the leads that attach to the resistor. This shielding prevents rf frequency from entering the superconducting circuitry through the leads connected to the heat switch. A Nb-Ti wire is then folded in half and wound noninductively around the lead shielded resistor. This wire is held in place with a small amount of GE 7031 varnish. The completed heat switch is attached to a small copper block that contains a round copper post that is tinned with solder. The Nb-Ti wire is then wound several times around this post and held in place with additional GE 7031 varnish. The copper post serves as a heat sink and insures that the only portion of the superconducting circuitry that is warmed above the transition temperature is the Nb-Ti wire directly in contact with the heat switch. These shielded heat switches are then mounted inside the large circular pockets in the Nb coil form holders. In all, sixteen heat switches are used in the SSA.

3.2.1 Levitation Circuitry

The levitation circuits used in the SSA to support and control the x linear and angular degrees of freedom are shown in Fig. 3.7, where all heat switches, superconducting joints, and current leads are shown explicitly. The y and z degrees of freedom have identical (in form) levitation circuits. Each of the superconducting joints is represented by a black dot. Each heat switch is shown schematically as a resistor in close proximity

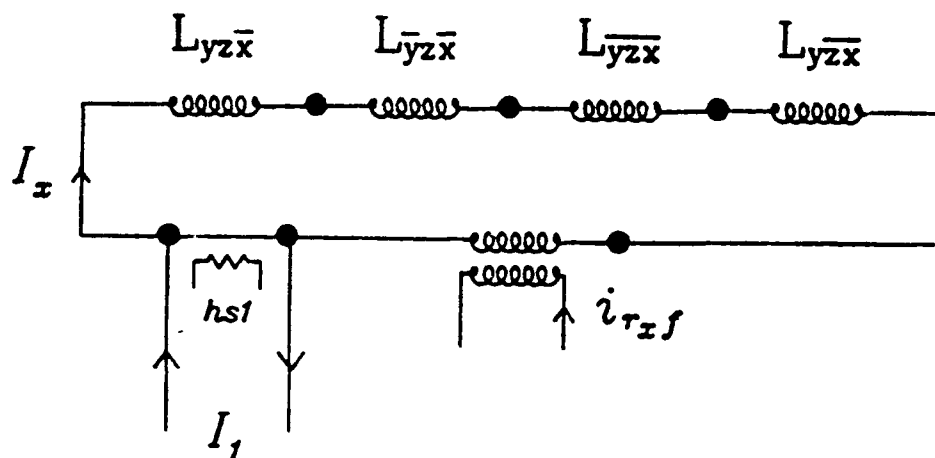
to a superconducting lead. Each heat switch has associated with it a pair of current leads which are used to store persistent currents in the circuitry.

All current leads in the SSA are constructed with 125 μm Cu clad Nb-Ti wire. The copper cladding reduces the risk of driving the current supply leads normal, and provides additional heat capacity that protects the leads. A programmable current supply, controllable through the GPIB interface, is used to supply external current to these current leads. If any portion of the superconducting circuit is driven normal while storing currents, the external current supply would damage the superconducting circuitry. In order to prevent this, an automatic protection circuit monitors the voltage across the current supply leads. Any voltage signal which exceeds a preset voltage threshold triggers a current shunt.

The r_z levitation-feedback circuit is less complex than the θ_x levitation-feedback circuit. Only a single heat switch, hs1, is used to disrupt the superconducting loop. The storage of a persistent current in the superconducting loop proceeds in several steps. Initially there is no current stored in the loop. The external current leads, I_1 , are then driven with a steady current of 0.5 A. At this point, all the current from the external current supply driving I_1 is passing through the heat switch. hs1 is then pulsed on for approximately 40 msec. This drives the short path between the two superconducting joints normal and forces the current to flow through the four inductors which levitate the proof mass in the r_x direction. Approximately 10 msec after the current driving the heat switch is removed, the heat switch becomes superconducting once again. This traps the current in the r_x levitation-feedback loop. This process is repeated at higher and higher current settings until the desired amount of flux is trapped in the r_x circuit. The bridge is carefully balanced in an iterative process which is described in the next chapter.

The θ_x levitation-feedback circuit contains two heat switches, hs2 and hs3, and two pairs of current supply leads, I_2 and I_3 . Initially, current is stored about the outer loop of the circuit. This is done by pulsing hs2 and hs3 on while supplying current to I_2 . This traps flux in the circuit so that $I_2 = I_{1\theta_x} = I_{2\theta_r}$. This provides an even downward pressure on the proof mass in the $-z$ direction. If a current is now supplied through I_3 and hs3 is pulsed on, the current trapped in each side of the circuit will be such that $I_{1\theta_x} = I_2 - I_3/2$, and $I_{2\theta_x} = I_2 + I_3/2$. This imbalance in current applies a torque about the θ_x axis of the proof mass. In practice, I_3 is used to apply a small torque to the proof

r_x Levitation-Feedback



θ_x Levitation-Feedback

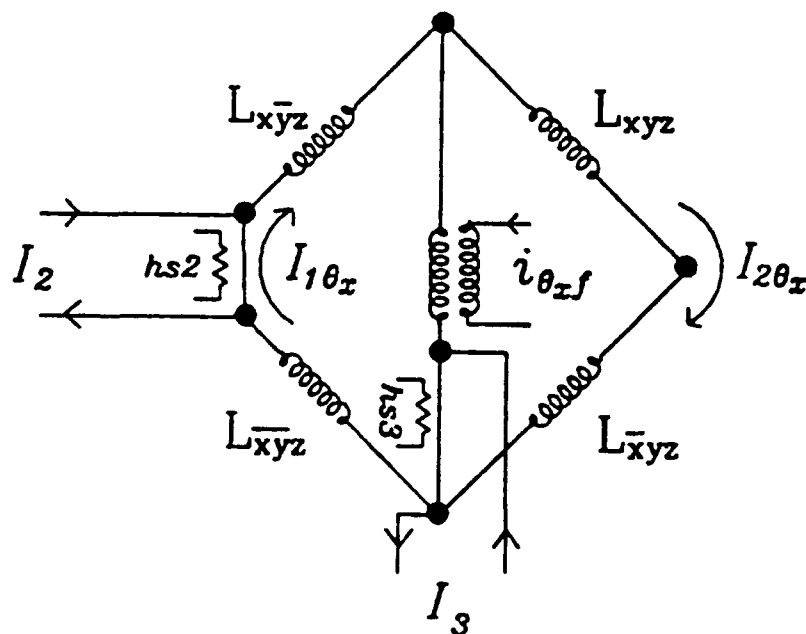


Figure 3.7. A schematic of the levitation circuitry.

mass which balances the θ_x sensing bridge.

3.2.2 Sensing Circuitry

The sensing circuit used in the SSA is shown in Fig. 3.8, where all heat switches, superconducting joints, and current leads are shown explicitly.

The six heat switches, hs4–hs9, are used to discharge any flux that may be trapped in the six sensing bridges. The seventh heat switch, hs10, is used to discharge any flux that may be trapped in the superconducting loop containing the SQUID input coil. This heat switch also serves to protect the SQUID from any input current spikes that may be induced in the sensing circuitry while currents are being stored in the levitation circuitry.

All leads from the sensing inductances are of equal length, and both sides of each sensing bridge are identical up to the small inductance added by each heat switch. This symmetry is important as the additional leads in the sensing circuitry generate stray inductance which can imbalance the sensing bridge. Any imbalance forces us to displace the proof mass away from equilibrium in order to rebalance the sensing bridge. Presently the heat switches in the SSA sensing circuit only lie on one side of each bridge. It is possible to construct an eight wire heat switch which would present a symmetrical set of stray inductances to the sensing bridge, but the present choice was made for its simplicity.

The six current leads, I_4 – I_9 , are driven by six room temperature oscillators. A polystyrene capacitor is connected across the primary of each transformer to form a tank circuit. The tank circuit strongly attenuates noise above its resonance frequency and, when driven on resonance, increases the driving current through the inductance bridge. The capacitors are selected so that each tank circuit resonates at a separate frequency with the lowest at a frequency of 500 Hz, and the highest at a frequency of 2500 Hz. The resonant frequencies lie equally spaced throughout this band.

The output of the SQUID amplifier (Model 2000, Quantum Design, Inc., San Diego, CA) is high-pass filtered, and fed into six separate lock-in amplifiers (Model 3961B, Ithaco, Inc., Ithaca, NY). Each lock-in amplifier is tuned to one of the six carrier frequencies and one of the six separately modulated signals is demodulated and recovered at the output of the lock-in.

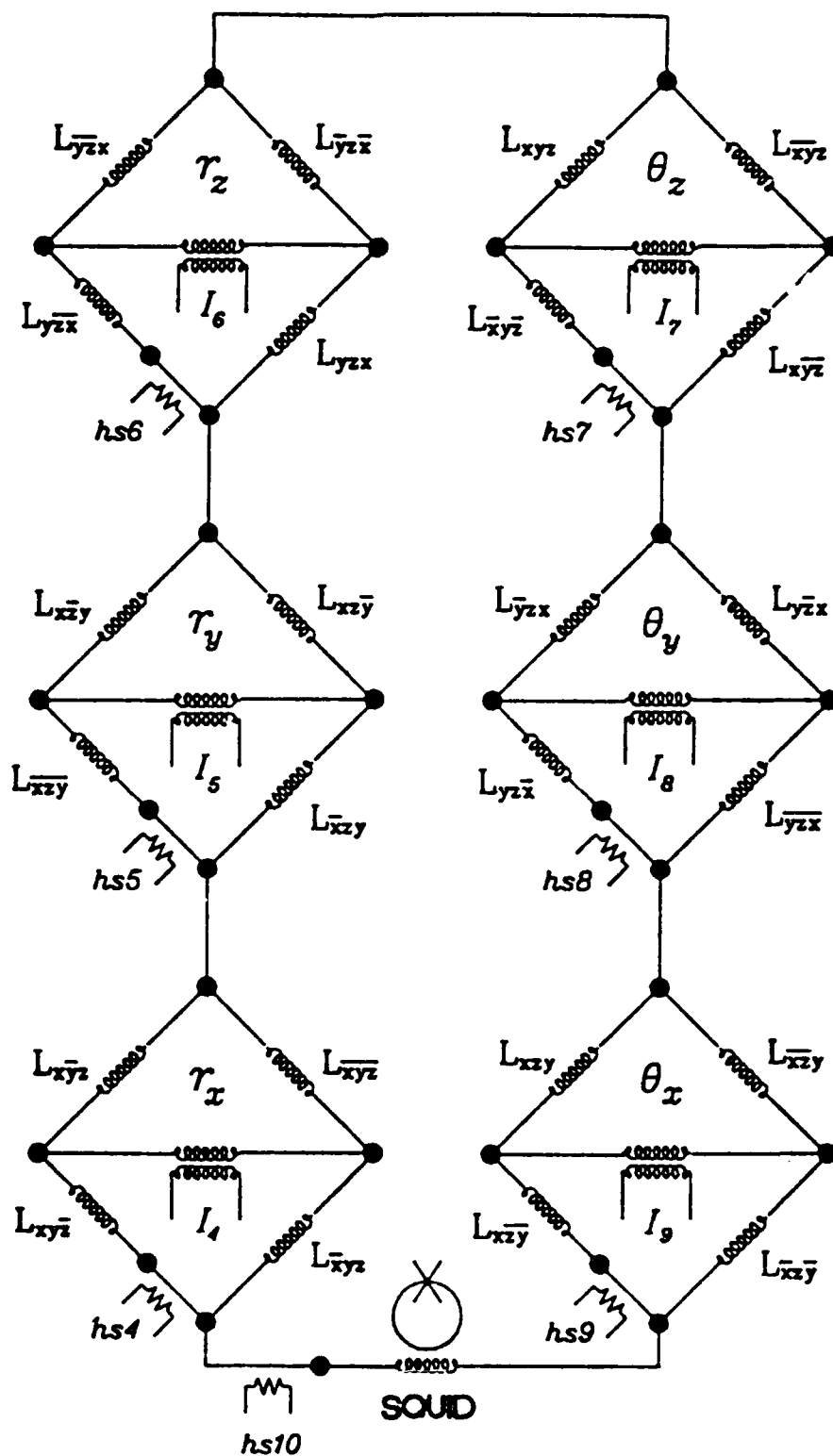


Figure 3.8. A schematic of the sensing circuitry.

3.3 Construction of the Experimental Test Apparatus

In this section, we describe the experimental test apparatus which houses the SSA: the thermal and mechanical design of the cryostat, the electrical isolation of the control leads, the vibration isolation of the SSA, and the room temperature shaker used to perform the calibration of the SSA.

3.3.1 Thermal and Mechanical Design of the Cryostat

The SSA is operated in a very quiet cryogenic vacuum space. A low boil-off super-insulated liquid He dewar (William G. Goree, Inc., Los Altos, California) was constructed with a careful design. The dewar has an inner diameter of 61 cm and an inner depth of 1.8 m. This large cryogenic space is carefully shielded. The inner jacket of the dewar is constructed from thin aluminum and Fiberglas. The upper section of the jacket is made of thin Fiberglas which has a low thermal conductivity to mechanical strength ratio. The lower section is made of aluminum. This combination helps to stiffen and electrically shield the lower section of the dewar without sacrificing the hold-time of the dewar. A long hold-time of liquid helium is needed for uninterrupted operation of the SSA and the SGG. This is also important in reducing the boiling noise from the liquid helium.

A super-insulated dewar was chosen over a more traditional nitrogen jacketed dewar in order to remove the noise of the boiling liquid nitrogen. This noise is of much more significance than the boiling helium since the liquid nitrogen would form the primary heat sink for the thermal radiation in the laboratory. With the current setup, no correlation between the activity in the helium bath and the noise in the SSA has been seen.

The outer jacket of the dewar is constructed from aluminum, and the entire unit is extremely rigid. This rigidity is important in order to reduce the long term "angular" drift of the dewar. Electromagnetic disturbances are also an important source of noise in a sensitive experiment. The cryostat has been carefully designed with this in mind. In addition to outer and inner layers of aluminum, three additional layers of shielding lie between the inner and outer jacket of the dewar. Two layers of mu-metal insure that any external magnetic field from the earth will be almost entirely excluded from the cryogenic space. A third shield, constructed from a thin layer of lead foil in close contact with the

inner aluminum jacket of the dewar, forms a superconducting shield which will exclude any residual electric and magnetic field. The resulting cryogenic space is exceptionally free of electromagnetic disturbances.

The cryostat insert which fits snugly into the cryogenic space is shown in Fig. 3.9. The top plate of the insert bolts to the top of the cryostat and a large rubber O-ring seals the cryogenic space from the laboratory atmosphere. This allows the liquid nitrogen, which is initially transferred into the dewar to precool the insert, to be pumped on by an external roughing pump and brought close to its triple point (63.15°K). This lowers the temperature of the insert and makes for a more efficient transfer of helium.

The large aluminum vacuum can at the base of the insert is anodized and coated internally with a thin layer of lead. This lead is evaporated onto the inner surface of the vacuum can by passing a large current through a niobium boat which is filled with lead. This lead thin film forms a type-I superconducting shield which further reduces magnetic flux level inside the experimental space. A final coating of Kodak KPR photo-resist is added to protect the thin coating.

Seven hollow Fiberglas tubes support the vacuum can from the brass plate at the top of the insert. Six of these tubes are equally spaced in a ring near the edge of the vacuum can and the seventh lies at the center. Each end of the hollow Fiberglas tubes is fitted to an aluminum fixture which is used to bolt the tubes in place. These aluminum fixtures are vacuum sealed with a thin layer of Armstrong A12 epoxy (Lunar Products, Inc., Fullerton, California), which matches the thermal expansion between the Fiberglas and the aluminum. These Fiberglas tubes in turn support several radiation shields constructed from copper coated Fiberglas PC-board material. These radiation shields provide thermal shielding and mechanically stiffen the insert. The spacing between the radiation shields is largest just above the vacuum can and decreases towards the top of the cryostat, where the thermal gradient is greatest.

All the leads that enter the cryostat are vapor cooled and heat sunk to the liquid helium bath. Two types of leads enter the cryostat: high current leads which are constructed from copper magnet wire, and low current leads which are constructed from manganin wire. Copper has a much higher thermal conductivity than manganin. For this reason, copper was used only for those few leads that must carry high current. All leads were spirally wound around the Fiberglas support tubes. This increases the surface area of the wire and allows for greater vapor cooling to take place. In addition,

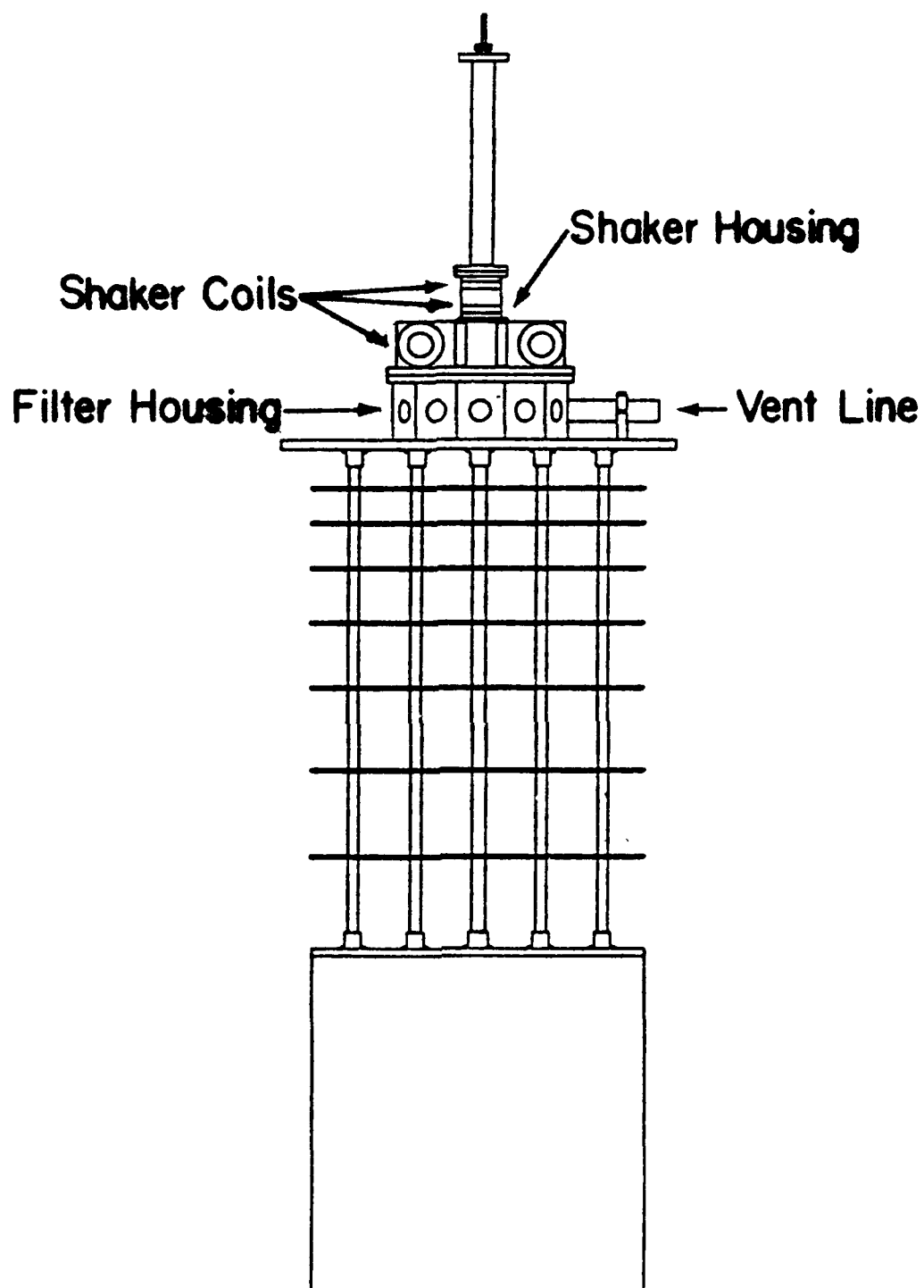


Figure 3.9. A schematic of the SSA cryostat insert.

the copper leads were heat sunk to the radiation shields.

The dewar is equipped with a helium level gauge (American Magnetics, Inc., Oak Ridge, Tennessee), which monitors the level of helium above the top of the vacuum can. In addition, several carbon resistors with large temperature coefficients are used to monitor the level of helium or nitrogen in the cryogenic space. A large nitrogen boil-off heater suspended below the vacuum can is used to boil away the liquid nitrogen prior to the initial filling with liquid helium. The heater is a thin aluminum plate with thirty 5 W, 1 Ω resistors epoxied to its surface and connected in series.

3.3.2 Electrical Isolation of the SSA

A large twelve-sided aluminum box on top of the dewar insert contains filters for all leads entering the cryogenic space. Each face of the filter box (except one) has one hermetically sealed forty-one pin connector bolted into it. The one face without a connector contains the vent line for the dewar. A twelve-sided copper wall fits concentrically inside the box. Each face of the copper wall (except the one with the vent line) has forty-one coaxial, bushing mounted emi filters (Model 9001-100-1010, Murata-Erie Corp., Toronto, Ontario) passing through it. These filters are high quality pi filters containing two capacitors and one inductor. Above thirty to forty kHz, each filter reduces the rf noise by 80 dB. Presently, only five of the eleven connectors are being used. The remaining six will be used by the SGG when it is integrated with the SSA. The center of the filter box is hollow and houses room temperature accelerometers used in the calibration of the SSA.

In addition to the rf filters at room temperature, there are eleven PC boards which contain filter capacitors. These are mounted on top of the vacuum can in the helium space. These capacitors provide additional filtering and help insure that the rf level of noise in the vacuum space is extremely low.

Each pair of feedback and oscillator leads that connect to the SSA are fed through a separate hollow Monel tube that extends from the brass plate at the top of the dewar insert to the top of the vacuum can. In this way the twin-ax leads are shielded all the way to the top of the vacuum can.

3.3.3 Vibration Isolation of the SSA and Shaker Design

A room temperature shaker, which is free to translate in x , y and z , and rotate about the z axis, is used in the calibration and test of the SSA. A cross section of this shaker is shown in Fig. 3.10. The shaker is mounted on top of the rf filter box on the cryostat insert. The center mass of the shaker is suspended in vacuum by a spring from the top of a Plexiglas tower. The center mass of the shaker is machined in the shape of a cross. A strong rare earth magnet is mounted at the end of each of the four protruding arms of the cross. Each of these magnets sits between two coils which are mounted to the outside of the shaker housing. By driving current through these eight coils in the appropriate combinations, the central mass of the shaker can be driven in three degrees of freedom: linear in x and y , and angular about the z axis (vertical). One more magnet mounted above the cross and below the supporting spring is used, along with a set of matching coils mounted outside the Plexiglas tower, to drive the shaker along the z axis. The housing of the shaker is constructed entirely of Plexiglas. This simplifies the task of alignment, and allows us to measure the rotational displacement and calculate the angular acceleration applied by the shaker to the SSA.

The calibration of acceleration applied to the SSA by the shaker in the linear degrees of freedom is provided by a set of three room temperature accelerometers (Sunstrand Data Corp., Redmond, WA) mounted immediately below the shaker mass. A thin Fiberglass rod is attached to the set of accelerometers and travels down through the hollow Fiberglass rod at the center of the dewar insert. This Fiberglass rod extends approximately 12 cm below the top of the vacuum can and is used to support the SSA.

The combined structure which supports the SSA can be modeled as a compound pendulum which is supported by a spring. The mode structure of this support is in general quite complicated, but in practice, we are only concerned with the frequency response well below the resonance modes of the suspension structure. At these low frequencies, the modes of the suspension structure can be ignored. At higher frequencies, the suspension can be thought of as a second order low-pass filter. This filtering of high frequency noise is important in order that the dynamic range of the SSA not be exceeded and the SQUID unlocked.

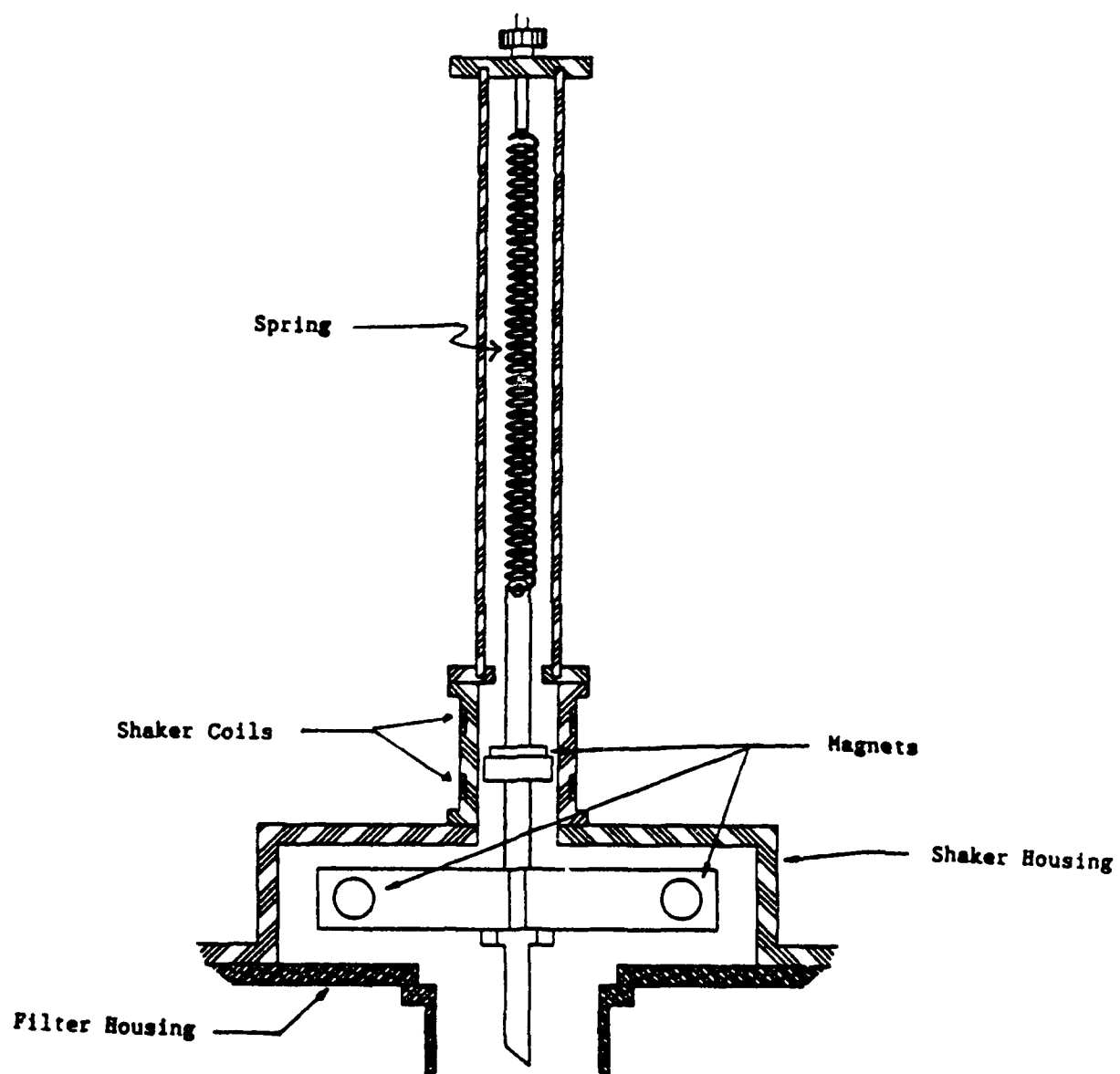


Figure 3.10. A cross sectional view of the SSA shaker.

3.4 Computer Control and Interface Electronics

The SSA contains nine pairs of current charging leads, sixteen heat switches, six pairs of current sensing leads, and six pairs of feedback control leads. Given the large number and combinations of parameters to control simultaneously, much of the experimental control had to be automated.

An AT-compatible computer forms the central core of the control system used with the SSA. This computer is equipped with two four-channel, sixteen-bit data acquisition boards (Model DT2816, Data Translation, Inc., Marlboro, MA) which allow the simultaneous capture of the six outputs from the SSA. A general purpose GPIB card (Model GPIB-PCIII, National Instruments Corp., Austin, TX) is used to control a programmable current supply (Model 2500EP, Valhalla Instruments, San Diego, CA), a precision DVM (Model 195A, Keithley Instruments, Inc., Cleveland, OH), and six lock-in amplifiers (Model 3961B, Ithaco Scientific Instruments Inc., Ithaca, NY). A parallel I/O card (Model DT2817, Data Translation, Inc., Marlboro, MA) is used to control custom cryostat interface electronics.

A custom interface control containing switchable current supplies, high and low current relays, and two separate instrumentation amplifiers, was constructed by the Electronics Development Group at the University of Maryland. This interface box is controlled manually or by twenty-four optically isolated digital logic lines connected to the AT-compatible computer.

The front panel of the interface can accept the input from two separate programmable current supplies. Presently, only one of these is in use, but changes in the design of the SSA in the future may necessitate the use of two separate supplies. High current relays are then used to route current to the appropriate charging leads of the SSA. Low current relays are then used to control which heat switches in the SSA are pulsed on and off. The amount of current used to drive each of these heat switches is set manually at the front panel. Two separate instrumentation amplifiers (one for each of the separate programmable current supplies) are used to differentially amplify the voltage across the current charging leads while current is being stored in the SSA. These outputs are used to control current protection circuits which shunt current away from the SSA if a preset voltage level is exceeded.

Chapter 4

Test of the Superconducting Six-Axis Accelerometer

In the previous two chapters we described the theory, design, and construction of the SSA. In this chapter we will describe the test and performance of the SSA.

Initially the proof mass rests on the three lower coil forms and all six inductance bridges are maximally unbalanced. Our task is to levitate the proof mass and balance all six bridges simultaneously. If each inductance in the SSA were identical, this task would be greatly simplified: all levitation currents would be identical and there would be no need to adjust the angular orientation of the proof mass. Every attempt has been made to insure that all of the coils in the SSA are as similar as possible. Despite this, variations in the diameter of the superconducting wire, errors in the orthogonality of the windings, and mechanical alignment errors conspire to insure that each coil is unique. This uniqueness forces all three levitation currents to be slightly different and additional currents must be stored in each of the angular levitation circuits in order to balance the three angular sensing circuits.

This balancing process is straightforward, but it must be carried out in an iterative manner. Each time one of the currents in the SSA is adjusted in order to balance one of the sensing bridges, the position of the proof mass changes. This small change in position causes the current stored in each of the other five levitation circuits to change. This change shifts the position in those other five degrees of freedom, and forces us to store new currents in each of those five levitation circuits.

In addition to the control for the SSA, the interface box contains additional circuitry to monitor the conditions inside the cryostat. Additional high current relays control the nitrogen boil-off heater and allow the computer to control the nitrogen boil-off cycle.

The SSA instrument has been designed to be completely automated. Presently, all currents in the SSA are stored under computer control, current protection circuitry can be checked and reset under computer control, and boil-off of the nitrogen in the dewar is automated.

Each lock-in amplifier contains a precision oscillator which is amplitude and frequency controllable. These oscillators are used to drive the sensing circuit in the SSA. Presently, the frequency and amplitude level of each oscillator is set manually and the complete automation of this is underway.

This process could go on indefinitely, were it not for the orthogonal design of the SSA. Each time one of the sensing bridges is rebalanced, the change in position along that degree of freedom is much greater than the change in position in the other five orthogonal directions. In practice, iteration through four or five cycles often brings us to the point where we are limited by the resolution of the current supply used to store currents in the SSA.

4.1 Accelerometer Parameters

The experimental parameters for the SSA are summarized in Table 4.1. The masses of the proof mass and SSA assembly are measured. The moments of inertia are computed from the mechanical design. The levitation and sensing inductance parameters are calculated in Section 4.1.1. The inductance of the feedback transformer secondary, L , was measured, as described in Section 4.1.2, and is an average value typical of the six feedback transformers. The input inductance of the SQUID, L_{SQ} , is taken from the manufacturer's data sheet. The remaining three parameters, c , d_L , and d_S , are taken from the mechanical design.

4.1.1 Levitation and Sensing Inductance Modeling

From our knowledge of the geometry of the superconducting coils in the SSA, we can calculate the parameters which describe the inductance of each of the coils. Each of the circular windings in the sensing or levitation coil can be thought of as a closed circular loop containing a current I . This loop creates a corresponding image current loop in the superconducting proof mass. By calculating the force between all current loops and image current loops and summing, we can calculate the force on the proof mass from each coil. This force will be a function of the distance, d , and orientation, θ , of the coil with respect to the proof mass. The force acting between the proof mass and one of the sensing or levitation coils can be related to the variation in inductance with position. By comparing these two forces, we can deduce the variation of inductance with position.

The force between two loops carrying equal and opposite currents I , is [8]

$$\mathbf{F}_{12} = \frac{\mu_0}{4\pi} I^2 \oint \oint \frac{\mathbf{x}_{12} d\mathbf{l}_1 \cdot d\mathbf{l}_2}{|\mathbf{x}_{12}|^3}, \quad (4.1)$$

| Parameter | Symbol | Value |
|--|-------------|-------------------------------------|
| Mass of the Proof Mass: | m | 0.144 kg |
| Mass of the SSA Assembly: | M | 4.8 kg |
| Moment of Inertia, Proof Mass: | I | $4.0 \times 10^{-5} \text{ kg m}^2$ |
| Moment of Inertia, SSA Assembly: | I_M | $8.2 \times 10^{-3} \text{ kg m}^2$ |
| Secondary Inductance of Feedback Transformers: | \bar{L} | 240 μH |
| Inductance of SQUID input Coil: | L_{SQ} | 2.0 μH |
| Parallel Displacement of Inductance Coil Center from Proof Mass Center: | c | $1.35 \times 10^{-2} \text{ m}$ |
| Perpendicular Displacement of Inductance Coil Center from Proof Mass Center | | |
| Levitation Coil: | d_L | $1.69 \times 10^{-3} \text{ m}$ |
| Sensing Coil: | d_S | $1.51 \times 10^{-3} \text{ m}$ |
| Levitation Coil Inductance Parameters: | | |
| | L_L | 31 μH |
| | Λ_L | $6.1 \times 10^{-2} \text{ H/m}$ |
| | β_L | $1.8 \times 10^{-3} \text{ H}$ |
| | γ_L | 48 H/m^2 |
| Sensing Coil Inductance Parameters: | | |
| | L_S | 1.8 μH |
| | Λ_S | $5.2 \times 10^{-3} \text{ H/m}$ |
| | β_S | $2.1 \times 10^{-4} \text{ H}$ |
| | γ_S | 5.9 H/m^2 |

Table 4.1. Experimental parameters for the SSA.

where $d\mathbf{l}_1$ and $d\mathbf{l}_2$ are infinitesimal segments of loops 1 and 2, respectively, and \mathbf{x}_{12} is the vector joining those two segments. Our two current loops, one physical of radius R_1 and one image of radius R_2 , are shown in Fig. 4.1. Each loop is situated at a distance $d + x$ and orientation θ with respect to the superconducting plane. Although Eq. (4.1) contains force components in the y and z directions, these components must vanish. Therefore, we need to compute only the x component of the force. Expanding Eq. (4.1) through first order in x and θ , and summing over all loops in both superconducting coils,

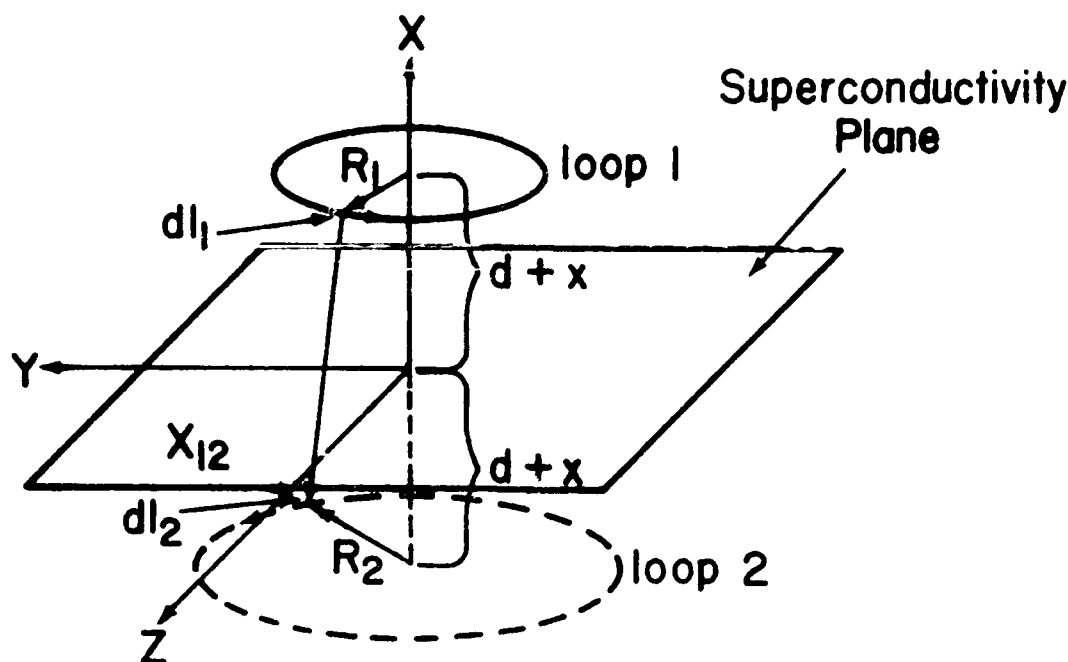


Figure 4.1. A schematic picture of a current loop above a superconducting plane interacting with an image current loop below.

we find

$$F_x = \frac{\mu_0}{4\pi} I^2 \sum_{R_1} \sum_{R_2} \oint \oint \frac{R_1 R_2 \cos(\theta_2 - \theta_1)}{[4d^2 + R_1^2 + R_2^2 - 2R_1 R_2 \cos(\theta_2 - \theta_1)]^{3/2}} \times \left(2d + 2x \left\{ 1 - \frac{12d^2}{[4d^2 + R_1^2 + R_2^2 - 2R_1 R_2 \cos(\theta_2 - \theta_1)]} \right\} \right) d\theta_1 d\theta_2, \quad (4.2)$$

where we have dropped all terms which vanish due to symmetries in the integrals.

The torque applied to loop 1 by loop 2 is given by the expression

$$\tau_{12} = \frac{\mu_0}{4\pi} I^2 \oint \oint \frac{\mathbf{R}_1 \times \mathbf{x}_{12} d\mathbf{l}_1 \cdot d\mathbf{l}_2}{|\mathbf{x}_{12}|^3}, \quad (4.3)$$

where \mathbf{R}_1 is the vector from the center of loop 1 to the infinitesimal line segment $d\mathbf{l}_1$. An expansion of this expression for small x and θ , and summation over all loops in each coil, gives

$$T_z = -\frac{\mu_0}{2\pi} R_1^2 R_2^2 \theta \sum_{R_1} \sum_{R_2} \oint \oint \frac{\cos(\theta_2 - \theta_1) \cos \theta_1 d\theta_1 d\theta_2}{[4d^2 + R_1^2 + R_2^2 - 2R_1 R_2 \cos(\theta_2 - \theta_1)]^{3/2}} \times \left\{ \frac{6d^2 (R_1 \cos \theta_1 + R_2 \cos \theta_2)}{[4d^2 + R_1^2 + R_2^2 - 2R_1 R_2 \cos(\theta_2 - \theta_1)]} - R_2 \cos \theta_2 \right\}. \quad (4.4)$$

The forces acting on the proof mass can also be calculated from the variation of inductance, L , with position:

$$F_x = \frac{1}{2} I^2 \frac{\partial L}{\partial x}, \quad (4.5)$$

$$T_z = \frac{1}{2} I^2 \frac{\partial L}{\partial \theta}. \quad (4.6)$$

Substituting the expression, Eq.(2.89), for the inductance into these two equations, we find

$$F_x = \frac{1}{2} \Lambda I^2 - \frac{1}{2} \gamma x I^2, \quad (4.7)$$

$$T_z = -\frac{1}{2} \beta \theta I^2. \quad (4.8)$$

Setting Eqs. (4.5) and (4.6) equal to Eqs. (4.2) and (4.4), and solving for Λ , β , and γ , we find

$$\Lambda = \frac{\mu_0}{\pi} \sum_{R_1} \sum_{R_2} \oint \oint \frac{R_1 R_2 \cos(\theta_2 - \theta_1) d}{[4d^2 + R_1^2 + R_2^2 - 2R_1 R_2 \cos(\theta_2 - \theta_1)]^{3/2}} d\theta_1 d\theta_2, \quad (4.9)$$

$$\begin{aligned} \gamma = \frac{\mu_0}{\pi} \sum_{R_1} \sum_{R_2} \oint \oint \frac{R_1 R_2 \cos(\theta_2 - \theta_1)}{[4d^2 + R_1^2 + R_2^2 - 2R_1 R_2 \cos(\theta_2 - \theta_1)]^{3/2}} \\ \times \left\{ \frac{12d^2}{[4d^2 + R_1^2 + R_2^2 - 2R_1 R_2 \cos(\theta_2 - \theta_1)]} - 1 \right\} d\theta_1 d\theta_2, \end{aligned} \quad (4.10)$$

$$\begin{aligned} \beta = \frac{\mu_0}{\pi} \sum_{R_1} \sum_{R_2} R_1^2 R_2 \oint \oint \frac{\cos(\theta_2 - \theta_1) \cos \theta_1 d\theta_1 d\theta_2}{[4d^2 + R_1^2 + R_2^2 - 2R_1 R_2 \cos(\theta_2 - \theta_1)]^{3/2}} \\ \times \left\{ \frac{6(R_1 \cos \theta_1 + R_2 \cos \theta_2) d^2}{[4d^2 + R_1^2 + R_2^2 - 2R_1 R_2 \cos(\theta_2 - \theta_1)]} - R_2 \cos \theta_2 \right\}. \end{aligned} \quad (4.11)$$

The expressions for Λ and γ can be reduced to one-dimensional integrals

$$\Lambda = 2\mu_0 \sum_{R_1} \sum_{R_2} \oint \frac{R_1 R_2 \cos u}{[4d^2 + R_1^2 + R_2^2 - 2R_1 R_2 \cos u]^{3/2}} du, \quad (4.12)$$

$$\begin{aligned} \gamma = 2\mu_0 \sum_{R_1} \sum_{R_2} \oint \frac{R_1 R_2 \cos u}{[4d^2 + R_1^2 + R_2^2 - 2R_1 R_2 \cos u]^{3/2}} \\ \times \left\{ \frac{12d^2}{[4d^2 + R_1^2 + R_2^2 - 2R_1 R_2 \cos u]} - 1 \right\} du, \end{aligned} \quad (4.13)$$

and numerically integrated using Romberg's method of order 10 [13].

The expression for β is less tractable and must be handled as a two-dimensional integral. This was implemented numerically as a one-dimensional integral which performs a series of one-dimensional integrals. These routines were implemented in the C

language, and the calculation of β for the levitation coil took in excess of 24 hours of CPU time on a VAX 8800.

Each sensing coil consists of 30 turns of Nb-Ti wire. The inner and outer diameter of each sensing coil is 0.51 cm and 1.22 cm, respectively. Once the proof mass is levitated, the center of each wire in the sensing coil rests $330 \mu\text{m}$ away from the proof mass surface. Substituting these parameters into our expressions for Λ , β , and γ , we find, after numerically integrating,

$$\Lambda_S = 5.4 \times 10^{-3} \text{ H/m}, \quad (4.14)$$

$$\beta_S = 2.1 \times 10^{-4} \text{ H}, \quad (4.15)$$

$$\gamma_S = 5.9 \text{ H/m}^2. \quad (4.16)$$

Multiplying Λ_S by the sensing coil to proof mass separation, $330 \mu\text{m}$, gives $L_S = 1.8 \mu\text{H}$.

Each levitation coil consists of two layers of Nb-Ti wire. Each layer holds 40 turns. The inner and outer diameter of each levitation coil are 1.28 cm and 2.11 cm, respectively. Once the proof mass is levitated, the centers of the wires which make up the upper layer in each levitation coil rest at a distance $d_1 = 440 \mu\text{m}$ away from the proof mass surface, and the centers of the wires which make up the lower layer rest at a distance $d_2 = 570 \mu\text{m}$ away from the proof mass surface. Because each levitation coil consists of two layers, the expressions for Λ , γ , and β are slightly more complicated and the term $4d^2$, which represents the distance between the physical current and the image current, must be replaced by $4d_1^2$, $4d_2^2$, and $(d_1 + d_2)^2$ as the double summation runs over the various layers of physical current and image current. Expanding the expressions for Λ , γ , and β into these three cases, and substituting the geometrical parameters, we find, after numerically integrating,

$$\Lambda_L = 6.1 \times 10^{-2} \text{ H/m}, \quad (4.17)$$

$$\beta_L = 1.8 \times 10^{-3} \text{ H}, \quad (4.18)$$

$$\gamma_L = 48 \text{ H/m}^2. \quad (4.19)$$

Multiplying Λ_L by the average levitation coil-proof mass separation, $(d_1 + d_2)/2$, gives $L_L = 31 \mu\text{H}$.

Each of the expressions for Λ , γ , and β ignores the rearrangement of the current in each of the superconducting wires due to the other superconducting wires and image

currents, and neglects the finite size of the superconducting plane. These are small errors, and our estimation of the coil parameters (β_S , Λ_S , γ_S , β_L , Λ_L , and γ_L) should be correct within ten to twenty percent.

4.1.2 DC Inductance Measurements

By storing a small current in each of the levitation circuits and then allowing that current which is trapped in the circuit to decay, it is possible to measure the amount of flux trapped in each of the superconducting loops. Since the amount of flux trapped in a superconducting loop is the product of the inductance and the current stored, it is possible to deduce the circuit inductance.

This technique [10] integrates the voltage generated across the heat switch, i.e.,

$$\Phi = L_{tot}I = \int_{-\infty}^{+\infty} V(t)dt = - \int_{-\infty}^{+\infty} L_{tot} \frac{dI}{dt} dt, \quad (4.20)$$

where L_{tot} is the total inductance of the superconducting loop. L_{tot} for each of the three linear inductance circuits can be computed from Eqs. (2.92) thru (2.115) and Fig. 2.5. We find

$$L_{totr_x} = L_{totr_y} = L_{totr_z} = 4L_L + L. \quad (4.21)$$

Storing small currents in each of the three linear levitation circuits does not levitate the proof mass, and L_L in Eq. (4.21) must be computed using the spacing ($250 \mu\text{m}$) between the proof mass and the levitation coil when the proof mass is resting on the sensing coil. We find $L_L = \Lambda_L 250 \mu\text{m} = 16 \mu\text{H}$. Experimentally, $L_{totr_x} = 330 \mu\text{H}$, $L_{totr_y} = 280 \mu\text{H}$, and $L_{totr_z} = 300 \mu\text{H}$. Substituting these values into the above equation, solving for L and averaging, we find

$$L = 240 \mu\text{H}. \quad (4.22)$$

Flux measurements of the three angular levitation circuits are consistent with this result.

4.2 Accelerometer Resonant Modes

The final set of currents stored in the SSA, which balance all six inductance bridges simultaneously, are given in Table 4.2. All three linear levitation currents are slightly different from each other, as expected. Initially, we attempted to store 0.9 A in all three angular levitation circuits and we discovered that one of the heat switches in

the θ_x levitation circuit was not operational. This forced us to use a symmetric pair of levitation currents, $I_{1\theta_y} = I_{1\theta_z}$.

From Eqs.(2.118), (2.119), (2.120), (2.124), (2.125), and (2.126), the expected levitation force is

$$f_{DCr_x} = [2I_{r_x}^2 - (I_{2\theta_y}^2 + I_{1\theta_y}^2)] \Lambda_L, \quad (4.23)$$

$$f_{DCr_y} = [2I_{r_y}^2 - (I_{2\theta_z}^2 + I_{1\theta_z}^2)] \Lambda_L, \quad (4.24)$$

$$f_{DCr_z} = [2I_{r_z}^2 - (I_{2\theta_x}^2 + I_{1\theta_x}^2)] \Lambda_L. \quad (4.25)$$

Setting these equations equal to the applied external force, $mg_E/\sqrt{3}$, substituting in our experimental currents, and solving for Λ_L , we find

$$\Lambda_L = 6.6 \times 10^{-2} \text{ H/m (from } f_{DCr_x}), \quad (4.26)$$

$$\Lambda_L = 6.9 \times 10^{-2} \text{ H/m (from } f_{DCr_y}), \quad (4.27)$$

$$\Lambda_L = 6.8 \times 10^{-2} \text{ H/m (from } f_{DCr_z}). \quad (4.28)$$

The first of these experimental values is slightly lower than the other two. This can be understood if we consider the fact that the diameter of the Nb-Ti wire varies slightly between coils, which changes the density of the windings and modifies Λ_L . The average experimental value, $\Lambda_L = 6.8 \times 10^{-2} \text{ H/m}$, is 11% higher than our theoretical value, but is reasonable when we take into account the crudeness of our inductance model.

The spring constants for each of the six degrees of freedom can be obtained from the levitation potentials in Eqs. (2.118), (2.119), (2.120), (2.124), (2.125), and (2.126). We find

$$k_{r_x} = 2 \left(\frac{8\Lambda_L^2}{4L_L + L} + \gamma_L \right) I_{r_x}^2 + 2(I_{2\theta_y}^2 + I_{1\theta_y}^2) \frac{\Lambda_L^2}{L_L + L} + (I_{2\theta_y} + I_{1\theta_y})^2 \frac{L\Lambda_L^2}{L_L(L_L + L)}, \quad (4.29)$$

$$k_{r_y} = 2 \left(\frac{8\Lambda_L^2}{4L_L + L} + \gamma_L \right) I_{r_y}^2 + 2(I_{2\theta_z}^2 + I_{1\theta_z}^2) \frac{\Lambda_L^2}{L_L + L} + (I_{2\theta_z} + I_{1\theta_z})^2 \frac{L\Lambda_L^2}{L_L(L_L + L)}, \quad (4.30)$$

$$k_{r_z} = 2 \left(\frac{8\Lambda_L^2}{4L_L + L} + \gamma_L \right) I_{r_z}^2 + 2(I_{2\theta_x}^2 + I_{1\theta_x}^2) \frac{\Lambda_L^2}{L_L + L} + (I_{2\theta_x} + I_{1\theta_x})^2 \frac{L\Lambda_L^2}{L_L(L_L + L)}, \quad (4.31)$$

$$\tau_{\theta_x} = (\Lambda_L d_L + c^2 \gamma_L + \beta_L) (2I_{r_y}^2 + 2I_{r_z}^2 + I_{2\theta_x}^2 + I_{1\theta_x}^2 + I_{2\theta_z}^2 + I_{1\theta_z}^2)$$

| Parameter | Symbol | Value |
|--|-----------------|----------|
| x Levitation Current | I_{r_x} | 2.639 A |
| y Levitation Current | I_{r_y} | 2.588 A |
| z Levitation Current | I_{r_z} | 2.455 A |
| θ_x Levitation Circuit 1 Current | $I_{1\theta_x}$ | -0.280 A |
| θ_x Levitation Circuit 2 Current | $I_{2\theta_x}$ | 0.280 A |
| θ_y Levitation Circuit 1 Current | $I_{1\theta_y}$ | 0.786 A |
| θ_y Levitation Circuit 2 Current | $I_{2\theta_y}$ | 1.014 A |
| θ_z Levitation Circuit 1 Current | $I_{1\theta_z}$ | 0.918 A |
| θ_z Levitation Circuit 2 Current | $I_{2\theta_z}$ | 0.882 A |
| x Resonance Frequency | f_{r_x} | 21.6 Hz |
| y Resonance Frequency | f_{r_y} | 21.5 Hz |
| z Resonance Frequency | f_{r_z} | 18.2 Hz |
| θ_x Resonance Frequency | f_{θ_x} | 14.96 Hz |
| θ_y Resonance Frequency | f_{θ_y} | 15.15 Hz |
| θ_z Resonance Frequency | f_{θ_z} | 16.23 Hz |
| Mechanical Quality Factor for the Linear Degrees of Freedom | Q_r | 220 |
| Mechanical Quality Factor for the Angular Degrees of Freedom | Q_θ | 700 |

Table 4.2. Levitation currents, resonance frequencies, and mechanical quality factors for each of the six modes of the SSA.

$$+ 2(I_{2\theta_x}^2 + I_{1\theta_x}^2) \frac{c^2 \Lambda_L^2}{L_L + L} + (I_{2\theta_x} - I_{1\theta_x})^2 \frac{L \Lambda_L^2 c^2}{L_L (L_L + L)}, \quad (4.32)$$

$$\begin{aligned} \tau_{\theta_y} = & \left(\Lambda_L d_L + c^2 \gamma_L + \beta_L \right) (2I_{r_x}^2 + 2I_{r_z}^2 + I_{2\theta_x}^2 + I_{1\theta_x}^2 + I_{2\theta_y}^2 + I_{1\theta_y}^2) \\ & + 2(I_{2\theta_y}^2 + I_{1\theta_y}^2) \frac{c^2 \Lambda_L^2}{L_L + L} + (I_{2\theta_y} - I_{1\theta_y})^2 \frac{L \Lambda_L^2 c^2}{L_L (L_L + L)}. \end{aligned} \quad (4.33)$$

$$\begin{aligned} \tau_{\theta_z} = & \left(\Lambda_L d_L + c^2 \gamma_L + \beta_L \right) (2I_{r_x}^2 + 2I_{r_y}^2 + I_{2\theta_y}^2 + I_{1\theta_y}^2 + I_{2\theta_z}^2 + I_{1\theta_z}^2) \\ & + 2(I_{2\theta_z}^2 + I_{1\theta_z}^2) \frac{c^2 \Lambda_L^2}{L_L + L} + (I_{2\theta_z} - I_{1\theta_z})^2 \frac{L \Lambda_L^2 c^2}{L_L (L_L + L)}. \end{aligned} \quad (4.34)$$

Substituting in our experimental currents, the average experimental value of Λ_L , and our theoretical parameters, and computing the resultant resonance frequencies, we find

$$f_{r_x} = 21.2 \text{ Hz}, \quad (4.35)$$

$$f_{r_y} = 20.9 \text{ Hz}, \quad (4.36)$$

$$f_{r_z} = 17.8 \text{ Hz}, \quad (4.37)$$

$$f_{\theta_x} = 13.8 \text{ Hz}, \quad (4.38)$$

$$f_{\theta_y} = 13.9 \text{ Hz}, \quad (4.39)$$

$$f_{\theta_z} = 14.5 \text{ Hz}. \quad (4.40)$$

The theoretical linear resonance frequencies match the experimental resonance frequencies quite closely. The theoretical angular resonance frequencies, however, are all approximately 10% below the corresponding experimental values. This implies that we have underestimated the angular spring constant by 20%. This is significant, but the angular spring constants are much more dependent on the nonlinear inductance model parameters, as can be seen from Eqs. (4.32) through (4.34). These parameters should be more dependent on subtle effects that we have neglected in our inductance modeling. The relative scaling between each group matches quite well with the experimental values, and confirms that our basic understanding of the dynamics of the SSA is correct. It is also worth pointing out that without the nonlinear inductance coefficients, β and γ , we would be unable to understand the mode structure of the SSA.

Thus far we have neglected the contributions that the sensing currents make to the resonance frequencies of the SSA. We will see in the next section that this is an excellent approximation.

4.3 Calibration and Noise Measurement

In this section, we characterize the circuitry used to drive the six sensing circuits in the SSA, examine the calibration of the SSA, calculate the energy coupling coefficients, and compare the expected sensitivity of the SSA with the experimental results.

4.3.1 Sensing Drive Circuitry

Each of the sensing circuits in the SSA is driven by a low noise current-to-voltage converter connected to an rf isolation transformer. This drive circuitry is shown in Fig. 4.2. A pair of pi filters are placed in line between the current-to-voltage converter and the rf isolation transformer. The combined lead and filter resistance in each leg of the circuit is $R_f = 2.0 \Omega$ and the pair of pi filters are modeled as two capacitors, $C_f = 0.185 \mu\text{F}$, and two inductors, $L_f = 0.17 \text{ mH}$. The outputs from the two pi filters

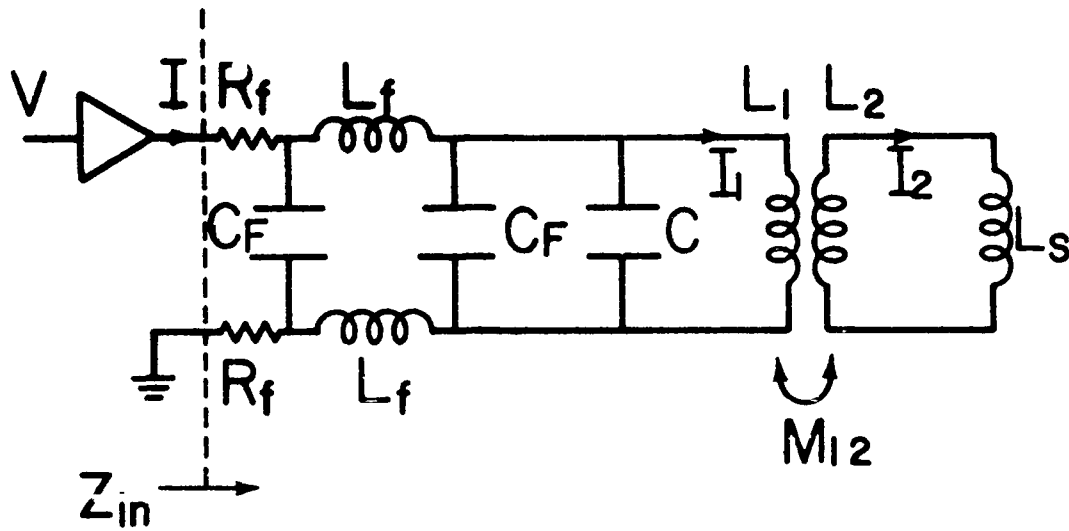


Figure 4.2. The rf isolation transformer and circuitry used to drive each of the sensing circuits in the SSA.

connect to a tank capacitance C placed in parallel with the isolation transformer. The rf isolation transformer is wound on a hollow aluminum fixture and consists of a primary and secondary coil of inductance L_1 and L_2 , respectively. The mutual inductance of the isolation transformer is M_{12} . A thin brass sheet separates the primary and secondary windings, and the eddy current losses in this isolation layer are represented by a resistance R , which is placed between the tank capacitor and the primary of the transformer.

The experimental parameters for each of the sensing circuits are shown in Table 4.3. The capacitances listed are the nominal values, as measured at room temperature.

It is straightforward to show that the current I_1 in the primary of the rf isolation transformer induces a current I_2 in the secondary of the transformer, of magnitude

$$I_2 = -\frac{M_{12}}{L_2 + L_S} I_1. \quad (4.41)$$

The effective input inductance of the isolation transformer can also be computed:

$$L_{eff} = \frac{L_1(L_2 + L_S) - M_{12}^2}{L_2 + L_S}. \quad (4.42)$$

This effective inductance will resonate with the combined capacitance, $C + C_f$, at a frequency

$$f = \frac{1}{2\pi} \frac{1}{\sqrt{L_{eff}(C + C_f)}}. \quad (4.43)$$

| Circuit | L_1 | L_2 | M_{12} | C | $ Z_{in} $ | f_{exp} |
|------------|---------|---------|----------|-------------|--------------|-----------|
| r_x | 3.75 mH | 0.17 mH | 0.53 mH | 10 μ F | 86 Ω | 1.00 kHz |
| r_y | 3.54 mH | 0.19 mH | 0.51 mH | 2 μ F | 95 Ω | 2.12 kHz |
| r_z | 3.54 mH | 0.20 mH | 0.50 mH | 1.3 μ F | 109 Ω | 2.47 kHz |
| θ_x | 3.51 mH | 0.17 mH | 0.51 mH | 45 μ F | 52 Ω | 0.50 kHz |
| θ_y | 3.57 mH | 0.19 mH | 0.51 mH | 5 μ F | 90 Ω | 1.41 kHz |
| θ_z | 3.54 mH | 0.20 mH | 0.53 mH | 3 μ F | 88 Ω | 1.84 kHz |

Table 4.3. Parameters for rf isolation circuits in the SSA.

It can also be shown that the transfer function between the input current into the rf isolation circuit, I , and the current passing through the primary of the isolation transformer, I_1 , is

$$\frac{I_1}{I} = \frac{1}{1 - \omega^2 L_{eff}(C + C_f) + Ri\omega(C + C_f)}, \quad (4.44)$$

where we have neglected the contribution from the first filter capacitor, C_f . The first filter capacitor will only play a significant role in the drive circuit when the frequency of interest is greater than 10 kHz, and all of our sensing circuits operate at frequencies below 2.5 kHz. At resonance, this reduces to

$$\frac{I_1}{I} = -i \frac{1}{R} \sqrt{\frac{L_{eff}}{C + C_f}}. \quad (4.45)$$

Combining this with Eq. (4.41), we find that the magnitude of the transfer function relating the drive current, I , to the sensing current, I_2 , is

$$\left| \frac{I_2}{I} \right| = \frac{1}{R} \sqrt{\frac{L_{eff}}{C + C_f}} \frac{M_{12}}{L_2 + L_S}. \quad (4.46)$$

It is clear from this expression that the transformer damping resistance is crucial in controlling the drive circuitry gain. We expect this resistance to increase as a function of frequency, and this will correspondingly reduce the gain in the rf isolation transformer as the frequency of the tank circuit resonance increases. This is a rather rough model of a very complicated distributed network. Given the sensitivity of the overall gain to the

damping resistance, we should not expect our theoretical results to agree precisely with the experimental results.

The damping resistance, R , can be computed by measuring the magnitude of the circuit input impedance, Z_{in} . Using straightforward circuit analysis, it can be shown that the input impedance of the complete rf isolation circuit is

$$Z_{in} = 2R_f + 2i\omega L_f + \frac{R + i\omega L_{eff}}{1 - \omega^2 L_{eff}(C + C_f) + Ri\omega(C + C_f)}, \quad (4.47)$$

where we have once again neglected the contribution from the first filter capacitor. At resonance, this impedance reduces to

$$Z_{in} = 2R_f + \frac{L_{eff}}{R(C + C_f)} - i \frac{L_{eff} - 2L_f}{\sqrt{L_{eff}(C + C_f)}}. \quad (4.48)$$

Solving for R , we find

$$R = \frac{L_{eff}}{(C + C_f) \left[\sqrt{|Z_{in}|^2 - \frac{(L_{eff} - 2L_f)^2}{L_{eff}(C + C_f)}} - 2R_f \right]}. \quad (4.49)$$

Substituting the experimental parameters from Table 4.3 into our expressions for R , L_{eff} (Eq. (4.42)), resonance frequency (Eq. (4.43)), and drive current transfer function (Eq. (4.46)), we find the theoretical parameters as listed in Table 4.4. The theoretical values for the resonance frequencies are all slightly larger than the corresponding experimental values. This is not too surprising, considering that the capacitance value is measured at room temperature, whereas the resonance is measured with the circuit at 4.2 K.

4.3.2 Residual Misbalance

Each of the sensing circuits in the SSA is balanced by adjusting the levitation current in the six levitation circuits which surround the proof mass. As described at the beginning of this chapter, this process proceeds in an iterative manner until, after several cycles, we are limited by the resolution of the current supply and a small residual misbalance exists in each of the sensing circuits.

The in-phase component of this misbalance is due to a slight error in the proof mass position, and is inductive in nature. In practice, this component of the misbalance is removed by sending a small DC current into each of the feedback transformers and

| Circuit | L_{eff} | f_{theory} | R | Transfer Function |
|------------|-----------|--------------|---------------|------------------------|
| r_x | 2.11 mH | 1.09 kHz | 2.5Ω | $I_{r_x}/I = 17.5$ |
| r_y | 2.18 mH | 2.31 kHz | 11Ω | $I_{r_y}/I = 7.6$ |
| r_z | 2.30 mH | 2.72 kHz | 15Ω | $I_{r_z}/I = 6.6$ |
| θ_x | 2.09 mH | 0.53 kHz | 1.04Ω | $I_{\theta_x}/I = 19$ |
| θ_y | 2.21 mH | 1.49 kHz | 5Ω | $I_{\theta_y}/I = 11$ |
| θ_z | 2.15 mH | 1.92 kHz | 6.6Ω | $I_{\theta_z}/I = 8.5$ |

Table 4.4. Theoretical parameters for rf isolation circuits in the SSA.

thereby adjusting the position of the proof mass until each sensing bridge in the SSA is nulled.

The out-of-phase component of the misbalance is independent of proof mass position, and is resistive in nature. To the extent that each sensing coil in the SSA is identical and suffers the same resistive loss, this resistive portion should vanish. In fact, each of the sensing coils is very well matched since each coil is formed from a single layer of windings of equal turns. The levitation coils are a two layer winding, the fabrication of which is much more difficult to control, and therefore these coils are less well matched.

In the current design, levitation and sensing coils rest side by side and are weakly coupled together. Thus, the limit on how well the sensing coils match comes from the levitation coils. We are currently attempting to understand this problem, and hope to improve this in the new design of the SSA.

In order to quantitatively understand the importance of the residual resistive misbalance, it is interesting to consider the bridge circuit shown in Fig. 4.3. Three of the inductances in the bridge are identical, and suffer dielectric and eddy current losses so that they present an impedance $i\omega L_S + R_S$. The fourth inductor is slightly different from the other three, and presents an impedance $i\omega L_S + R_S + \delta R_S$. Solving for the current through the SQUID input coil and the five other bridges, we find

$$i = -\frac{\delta R_S I \cos \omega t}{4[R_S + i\omega(6L_S + L_{SQ})]}, \quad (4.50)$$

where we have expanded through first order in δR_S .

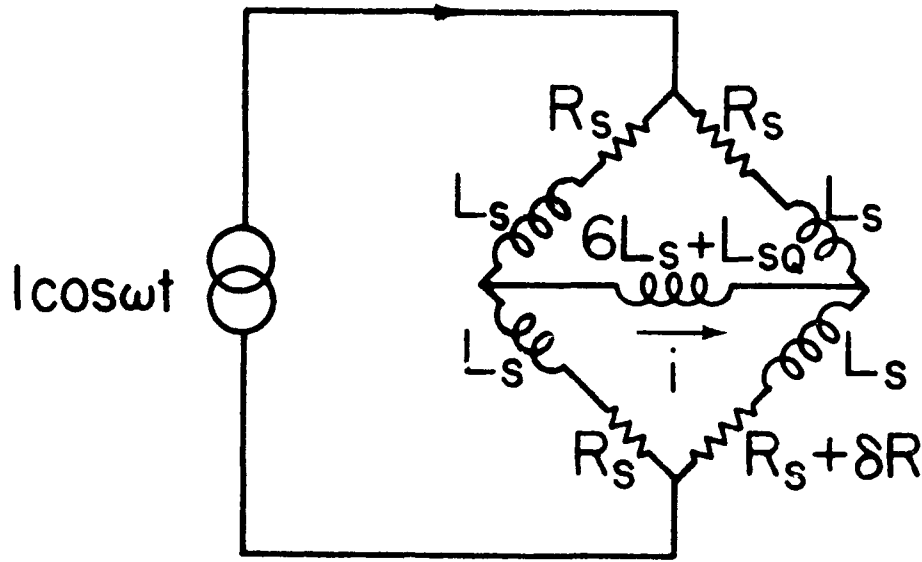


Figure 4.3. A bridge circuit containing a small resistive component.

Measurements of the resistive component of the impedance of a single sensing coil at three separate frequencies give

$$R_S(0.5 \text{ kHz}) = 19.5 \mu\Omega, \quad (4.51)$$

$$R_S(1.0 \text{ kHz}) = 46.3 \mu\Omega, \quad (4.52)$$

$$R_S(5.0 \text{ kHz}) = 171 \mu\Omega. \quad (4.53)$$

Recalling that $L_S = 1.8 \mu\text{H}$, we find, as must be the case, $R_S \ll \omega L_S$ for the range of carrier frequencies used. Applying this limit to Eq.(4.50), we find that the amplitude of the flux signal through the SQUID loop is

$$\Phi = \frac{M_{SQ} I R_S}{4\omega(6L_S + L_{SQ})} \frac{\delta R_S}{R_S}, \quad (4.54)$$

where $M_{SQ} = 2.0 \times 10^{-8} \text{H}$ is the mutual inductance between the SQUID input coil and the SQUID loop.

The slew rate of the SQUID feedback controller determines the maximum signal size, Φ_{max} , that the SQUID amplifier can handle. Thus, the maximum amplitude of the current into the sensing bridge is

$$I_{max} = \frac{4\omega(6L_S + L_{SQ})\Phi_{max}}{M_{SQ} R_S (\delta R_S / R_S)} \quad (4.55)$$

For the Quantum Design Model 2000 SQUID controller, the maximum signal size is $8.0 \times 10^3 \Phi_o$ up to about 60 Hz. Above this it drops off with frequency, reaching $1 \Phi_o$ at approximately 20 kHz. At 2.5 kHz, the maximum signal is approximately $20 \Phi_o$. Assuming a 5 % misbalance in R_S ,

$$I_{max} = 0.34 \text{ A.} \quad (4.56)$$

The actual limit on the drive current through the bridge driven at 2.5 kHz was found to be close to this value. Note that at lower frequencies Φ_{max} will be higher so I_{max} should be higher. In fact, for the bridges driven at the lower frequencies, the current was limited by a superconducting-to-normal transition, probably caused by eddy current heating in the isolation transformer.

4.3.3 Linear Acceleration

The three linear acceleration circuits are calibrated by driving the shaker along the vertical and comparing the signal from the vertically oriented room temperature accelerometer to the signals from the SSA. The r_x , r_y , and r_z circuits were driven with currents of 13.25 mA, 0.75 mA, and 13.25 mA, respectively. Multiplying these currents by the three corresponding gains (I_{r_i}/I) listed in Table 4.4, we find

$$I_{r_x} = 232 \text{ mA.} \quad (4.57)$$

$$I_{r_y} = 5.7 \text{ mA,} \quad (4.58)$$

$$I_{r_z} = 113 \text{ mA.} \quad (4.59)$$

The r_y levitation circuit was limited in drive current because the leads used to drive the r_y feedback transformer were damaged during the cool-down and no feedback current could be sent to that circuit. This left a large misbalance signal which caused the SQUID to unlock if a current with an amplitude larger than 0.75 mA was driven into the r_y sensing circuit.

The experimental sensitivities for r_x , r_y , and r_z at these drive currents were measured to be

$$\langle H_{axi} \rangle_{rms} = 3.1 \times 10^5 \Phi_o/g, \quad (4.60)$$

$$\langle H_{ay1} \rangle_{rms} = 9.9 \times 10^3 \Phi_o/g, \quad (4.61)$$

$$\langle H_{az1} \rangle_{rms} = 1.6 \times 10^5 \Phi_o/g. \quad (4.62)$$

The theoretical transfer functions for the three linear degrees of freedom are, from Eqs. (2.195) through (2.197),

$$\langle H_{axi} \rangle_{rms} = \frac{I_r}{\sqrt{2}} \frac{\Lambda_S}{L_{SQ} + 6L_S} \frac{1}{\omega_r^2 + i\omega_r\omega/Q_r - \omega^2}, \quad (4.63)$$

$$\langle H_{ayi} \rangle_{rms} = \frac{I_r}{\sqrt{2}} \frac{\Lambda_S}{L_{SQ} + 6L_S} \frac{1}{\omega_r^2 + i\omega_r\omega/Q_r - \omega^2}, \quad (4.64)$$

$$\langle H_{azi} \rangle_{rms} = \frac{I_r}{\sqrt{2}} \frac{\Lambda_S}{L_{SQ} + 6L_S} \frac{1}{\omega_r^2 + i\omega_r\omega/Q_r - \omega^2}. \quad (4.65)$$

These equations were derived for identical resonance frequencies and identical drive levels. All three of our linear resonance frequencies differ slightly, so that ω_r must be replaced by ω_{rx} , ω_{ry} , and ω_{rz} in each of the three equations. All three drive levels differ, and I_r must be similarly replaced by I_{rx} , I_{ry} , and I_{rz} . Making these substitutions and taking the limit where $\omega \ll \omega_r$, we find

$$\langle H_{axi} \rangle_{rms} = \frac{I_{rx}}{4\sqrt{2}\pi^2 f_{rx}^2} \frac{\Lambda_S}{L_{SQ} + 6L_S}, \quad (4.66)$$

$$\langle H_{ayi} \rangle_{rms} = \frac{I_{ry}}{4\sqrt{2}\pi^2 f_{ry}^2} \frac{\Lambda_S}{L_{SQ} + 6L_S}, \quad (4.67)$$

$$\langle H_{azi} \rangle_{rms} = \frac{I_{rz}}{4\sqrt{2}\pi^2 f_{rz}^2} \frac{\Lambda_S}{L_{SQ} + 6L_S}. \quad (4.68)$$

Substituting the values of sensing currents and other parameters into these equations, we find

$$\langle H_{axi} \rangle_{rms} = 3.5 \times 10^5 \Phi_o/g, \quad (4.69)$$

$$\langle H_{ayi} \rangle_{rms} = 8.8 \times 10^3 \Phi_o/g, \quad (4.70)$$

$$\langle H_{azi} \rangle_{rms} = 2.4 \times 10^5 \Phi_o/g. \quad (4.71)$$

The first two of these theoretical sensitivities agree with the experimental values within 10%. This is a rather good agreement, given the crudeness with which we are able to model the damping in the rf isolation transformer. The third value is 50% larger than the experimental value.

A log-log plot showing the low-frequency noise spectra from 0.3 mHz to 0.3 Hz for the r_x and r_z sensing circuits is shown in Fig. 4.4. Above 0.1 Hz, the spectrum is dominated by the background seismic noise of the laboratory. Below 0.1 Hz, the spectrum appears to be dominated by $1/f$ type noise. The broad peak around 0.2 Hz corresponds to the peak in the seismic noise of the earth reported by seismologists [1,2],

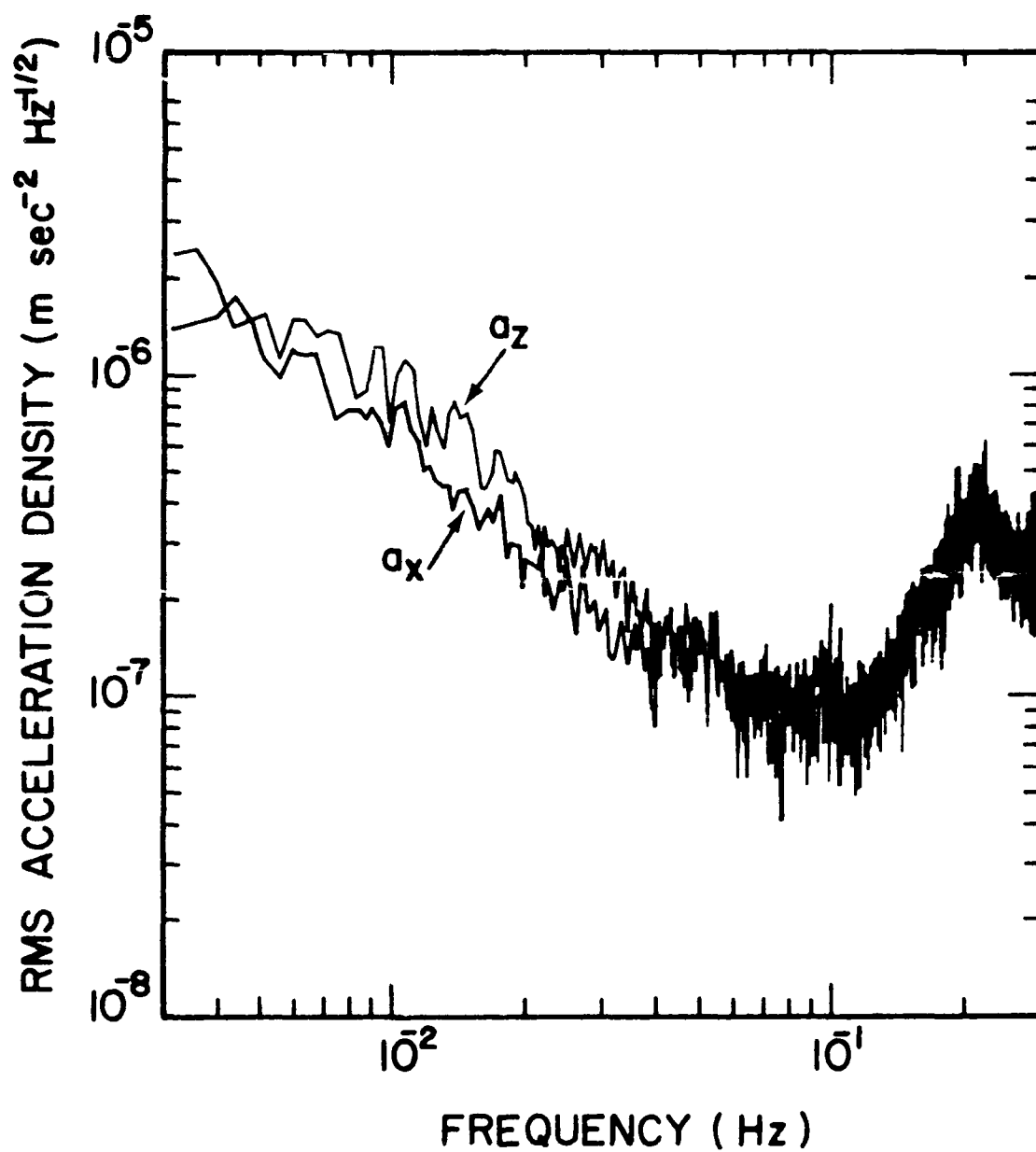


Figure 4.4. The very low frequency spectra of noise as measured by the r_x and r_z sensing circuits.

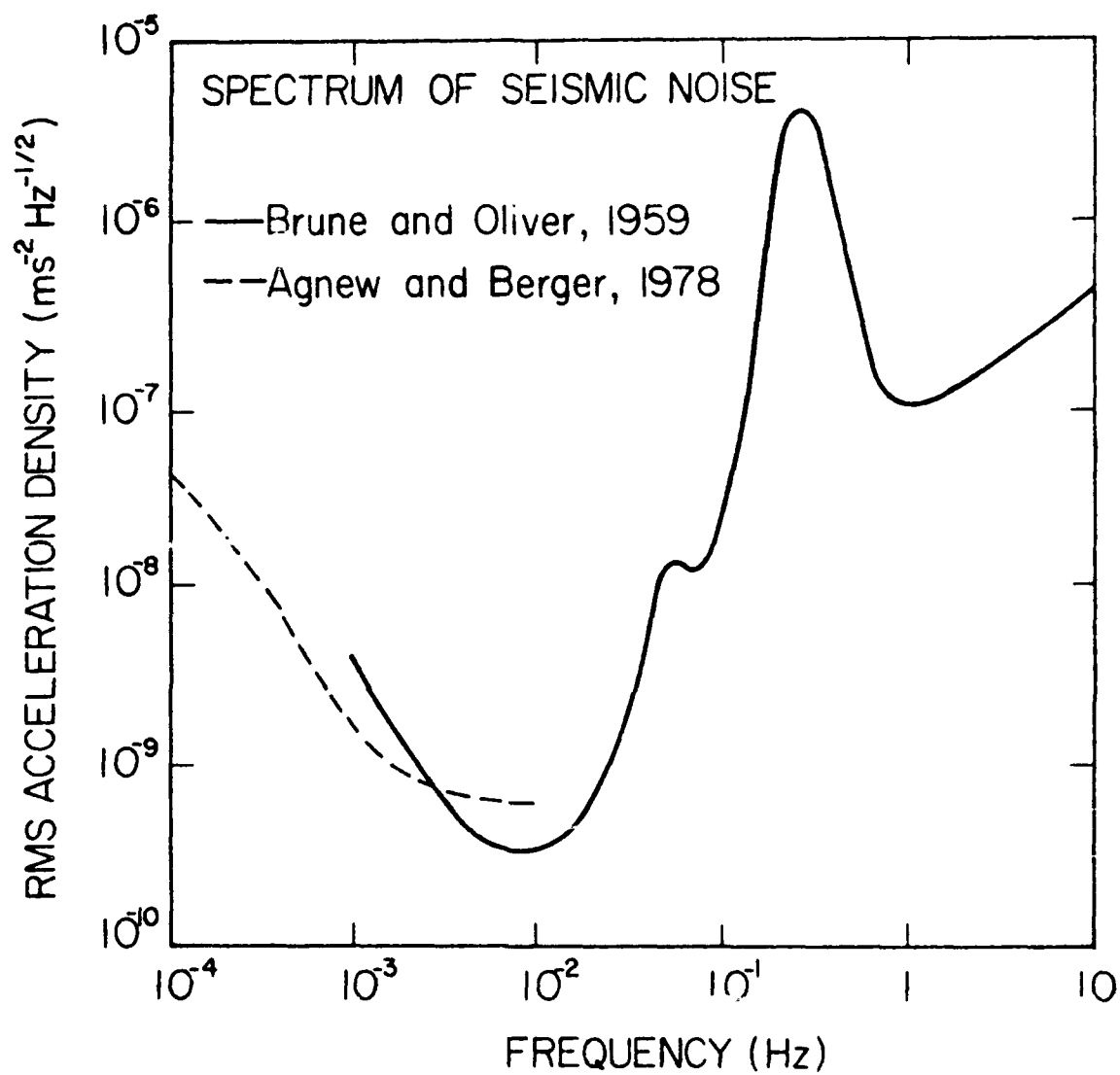


Figure 4.5. The expected low frequency spectrum of seismic noise generated by the earth.

as is shown in Fig. 4.5. The peak is attributed to the periodic pounding of the shores by ocean waves. Its amplitude is strongly dependent on a number of factors, including the distance to the shore and the amplitude of the ocean waves, so it is not surprising that the agreement between the peak heights on the two figures is not better. Note that the seismic noise drops by over two orders of magnitude below this peak. The fact that the SSA's signal does not reach a lower minimum is an indication that the spectrum is dominated by instrument noise below 0.1 Hz.

The source of the low frequency noise has not been identified. It could be due to a slow tilt of the accelerometer platform brought about by mechanical creep in the suspension. Such a tilt would modulate the earth's gravity. Low frequency drifts in the oscillator amplitude or the temperature may also be sources of $1/f$ noise. Additionally, flux creep can cause drifts in superconducting levitation circuits which induce $1/f$ noise in the outputs [9]. As mentioned previously, Nb-Ti wire was used in the present design of the SSA in order to overcome the reliability problems encountered with the niobium wire available at the time. It is well known that flux creep may be significant in type-II superconductors such as Nb-Ti. Future work must concentrate on determining and reducing low frequency noise.

Energy Coupling and Fundamental Instrument Noise

The fundamental instrument noise in the three linear degrees of freedom in the SSA is described by Eqs. (2.229) through (2.232). In deriving these equations, we assumed that all three linear modes were identical and did not take into account variations in the resonance frequencies, ω_r , the quality factors, Q_r , and the energy coupling coefficients, β_r . Replacing β_r by β_{rx} , β_{ry} , and β_{rz} , and Q_r by Q_{rx} , Q_{ry} , and Q_{rz} , and substituting ω_{rx} , ω_{ry} , and ω_{rz} in place of the generic ω_r , we find

$$P_{ax} = \frac{4\omega_{rx}}{m} \left(\frac{k_B T}{Q_{rx}} + \frac{\omega_{rx} E_S}{\beta_{rx}} \right), \quad (4.72)$$

$$P_{ay} = \frac{4\omega_{ry}}{m} \left(\frac{k_B T}{Q_{ry}} + \frac{\omega_{ry} E_S}{\beta_{ry}} \right), \quad (4.73)$$

$$P_{az} = \frac{4\omega_{rz}}{m} \left(\frac{k_B T}{Q_{rz}} + \frac{\omega_{rz} E_S}{\beta_{rz}} \right). \quad (4.74)$$

where β_{r_x} , β_{r_y} , and β_{r_z} are, from Eq. (2.228),

$$\beta_{r_x} = \frac{1}{2} \left(\frac{I_{r_x} \Lambda_S}{L_{SQ} + 6L_S} \right)^2 \frac{L_{SQ}}{m\omega_{r_x}^2}, \quad (4.75)$$

$$\beta_{r_y} = \frac{1}{2} \left(\frac{I_{r_y} \Lambda_S}{L_{SQ} + 6L_S} \right)^2 \frac{L_{SQ}}{m\omega_{r_y}^2}, \quad (4.76)$$

$$\beta_{r_z} = \frac{1}{2} \left(\frac{I_{r_z} \Lambda_S}{L_{SQ} + 6L_S} \right)^2 \frac{L_{SQ}}{m\omega_{r_z}^2}. \quad (4.77)$$

Substituting the sensing currents along with other parameters into these equations, we find

$$\beta_{r_x} = 3.3 \times 10^{-6}, \quad (4.78)$$

$$\beta_{r_y} = 2.0 \times 10^{-9}, \quad (4.79)$$

$$\beta_{r_z} = 1.1 \times 10^{-6}. \quad (4.80)$$

These couplings are extremely small and explain why we did not have to consider the contribution of the sensing current to the linear resonance frequencies in the previous section. These small couplings severely limit the sensitivity of the accelerometer. In the new design, these coupling coefficients should be larger, and the SSA should approach its potential sensitivity.

The white noise level normally observed from the Quantum Design RF SQUIDS is $10^{-4} \Phi_0/\sqrt{\text{Hz}}$, which is equivalent to a power spectral density of $E_S = 10^{-28} \text{ J/Hz}$. Substituting this, the experimental parameters, and the values for the energy coupling coefficients into expressions for the power spectral density, Eqs. (4.72) through (4.74), we find

$$P_{a_x}^{1/2} = 4.0 \times 10^{-10} \text{ g}/\sqrt{\text{Hz}}, \quad (4.81)$$

$$P_{a_y}^{1/2} = 1.6 \times 10^{-8} \text{ g}/\sqrt{\text{Hz}}, \quad (4.82)$$

$$P_{a_z}^{1/2} = 5.9 \times 10^{-10} \text{ g}/\sqrt{\text{Hz}}. \quad (4.83)$$

At frequencies above approximately 40 Hz, the signal due to seismic noise drops below the white noise level of the SQUID amplifier, so this level can be observed directly. Dividing by the measured sensitivities, Eqs. (4.60) through (4.62), we obtain

$$P_{a_x}^{1/2} = 3.2 \times 10^{-10} \text{ g}/\sqrt{\text{Hz}}, \quad (4.84)$$

$$P_{a_y}^{1/2} = 1.0 \times 10^{-8} \text{ g}/\sqrt{\text{Hz}}, \quad (4.85)$$

$$P_{a_z}^{1/2} = 6.4 \times 10^{-10} \text{ g}/\sqrt{\text{Hz}}. \quad (4.86)$$

These are in reasonable agreement with the theoretical noise limits.

4.3.4 Angular Acceleration

The three angular acceleration circuits are calibrated by driving the shaker about the vertical axis and comparing the three angular signals from the SSA to the rms amplitude of the angular motion.

The θ_x , θ_y , and θ_z circuits were driven with currents of 25.5, 13.3 mA, and 13.0 mA, respectively. Multiplying these currents by the three corresponding gains in Table 4.3, we find

$$I_{\theta_x} = 484 \text{ mA}, \quad (4.87)$$

$$I_{\theta_y} = 146 \text{ mA}, \quad (4.88)$$

$$I_{\theta_z} = 110 \text{ mA}. \quad (4.89)$$

The experimental sensitivities for θ_x , θ_y , and θ_z at these drive currents were measured to be

$$\langle H_{\alpha_x i} \rangle_{rms} = 2.1 \times 10^3 \Phi_o / \text{rad/sec}^2, \quad (4.90)$$

$$\langle H_{\alpha_y i} \rangle_{rms} = 6.9 \times 10^2 \Phi_o / \text{rad/sec}^2, \quad (4.91)$$

$$\langle H_{\alpha_z i} \rangle_{rms} = 4.7 \times 10^2 \Phi_o / \text{rad/sec}^2. \quad (4.92)$$

The theoretical transfer functions for the three angular degrees of freedom are, from Eqs. (2.198) through (2.200),

$$\langle H_{\alpha_x i} \rangle_{rms} = \frac{I_{\theta}}{\sqrt{2}} \frac{c\Lambda_S}{LSQ + 6LS\omega_{\theta}^2 + i\omega_{\theta}\omega/Q_{\theta} - \omega^2} \frac{1}{\omega_{\theta}}, \quad (4.93)$$

$$\langle H_{\alpha_y i} \rangle_{rms} = \frac{I_{\theta}}{\sqrt{2}} \frac{c\Lambda_S}{LSQ + 6LS\omega_{\theta}^2 + i\omega_{\theta}\omega/Q_{\theta} - \omega^2} \frac{1}{\omega_{\theta}}, \quad (4.94)$$

$$\langle H_{\alpha_z i} \rangle_{rms} = \frac{I_{\theta}}{\sqrt{2}} \frac{c\Lambda_S}{LSQ + 6LS\omega_{\theta}^2 + i\omega_{\theta}\omega/Q_{\theta} - \omega^2} \frac{1}{\omega_{\theta}}. \quad (4.95)$$

Since actual angular resonance frequencies differ slightly, ω_{θ} must be replaced by ω_{θ_x} , ω_{θ_y} , and ω_{θ_z} in each of the three equations. Likewise, I_{θ} must be replaced by I_{θ_x} , I_{θ_y} ,

and I_{θ_x} . Making these substitution and taking the limit where $\omega \ll \omega_\theta$, we find

$$\langle H_{\alpha_x i} \rangle_{rms} = \frac{I_{\theta_x}}{4\sqrt{2}\pi^2 f_{\theta_x}^2} \frac{c\Lambda_S}{LSQ + 6LS}, \quad (4.96)$$

$$\langle H_{\alpha_y i} \rangle_{rms} = \frac{I_{\theta_y}}{4\sqrt{2}\pi^2 f_{\theta_y}^2} \frac{c\Lambda_S}{LSQ + 6LS}, \quad (4.97)$$

$$\langle H_{\alpha_z i} \rangle_{rms} = \frac{I_{\theta_z}}{4\sqrt{2}\pi^2 f_{\theta_z}^2} \frac{c\Lambda_S}{LSQ + 6LS}. \quad (4.98)$$

Substituting the values of sensing currents and other parameters into these equations, we find

$$\langle H_{\alpha_x i} \rangle_{rms} = 2.1 \times 10^3 \Phi_o / \text{rad/sec}^2, \quad (4.99)$$

$$\langle H_{\alpha_y i} \rangle_{rms} = 6.2 \times 10^2 \Phi_o / \text{rad/sec}^2, \quad (4.100)$$

$$\langle H_{\alpha_z i} \rangle_{rms} = 4.1 \times 10^2 \Phi_o / \text{rad/sec}^2. \quad (4.101)$$

These values are in good agreement with the experimental sensitivities.

The low-frequency spectra of seismic noise, as measured by the θ_x , θ_y , and θ_z sensing circuits, are shown in Fig. 4.6. The figure shows the fundamental and harmonics of the angular calibration signal at 0.4 Hz. The four other peaks are due to modes of the suspension, such as the pendulum mode at 0.36 Hz and the vertical spring mode at 1.3 Hz.

Energy Coupling and Fundamental Instrument Noise

The fundamental instrument noise in the three angular degrees of freedom in the SSA is described by Eq. (2.233). In deriving this equation, we assumed that all three angular modes were identical and did not take into account variations in the resonance frequencies, ω_θ , and the energy coupling coefficients, β_θ . Replacing β_θ by β_{θ_x} , β_{θ_y} , and β_{θ_z} , and substituting ω_{θ_x} , ω_{θ_y} , and ω_{θ_z} in place of the generic ω_θ , we find

$$P_{\alpha_x} = \frac{4\omega_{\theta_x}}{I} \left(\frac{k_B T}{Q_{\theta_x}} + \frac{\omega_{\theta_x} E_S}{\beta_{\theta_x}} \right), \quad (4.102)$$

$$P_{\alpha_y} = \frac{4\omega_{\theta_y}}{I} \left(\frac{k_B T}{Q_{\theta_y}} + \frac{\omega_{\theta_y} E_S}{\beta_{\theta_y}} \right), \quad (4.103)$$

$$P_{\alpha_z} = \frac{4\omega_{\theta_z}}{I} \left(\frac{k_B T}{Q_{\theta_z}} + \frac{\omega_{\theta_z} E_S}{\beta_{\theta_z}} \right). \quad (4.104)$$

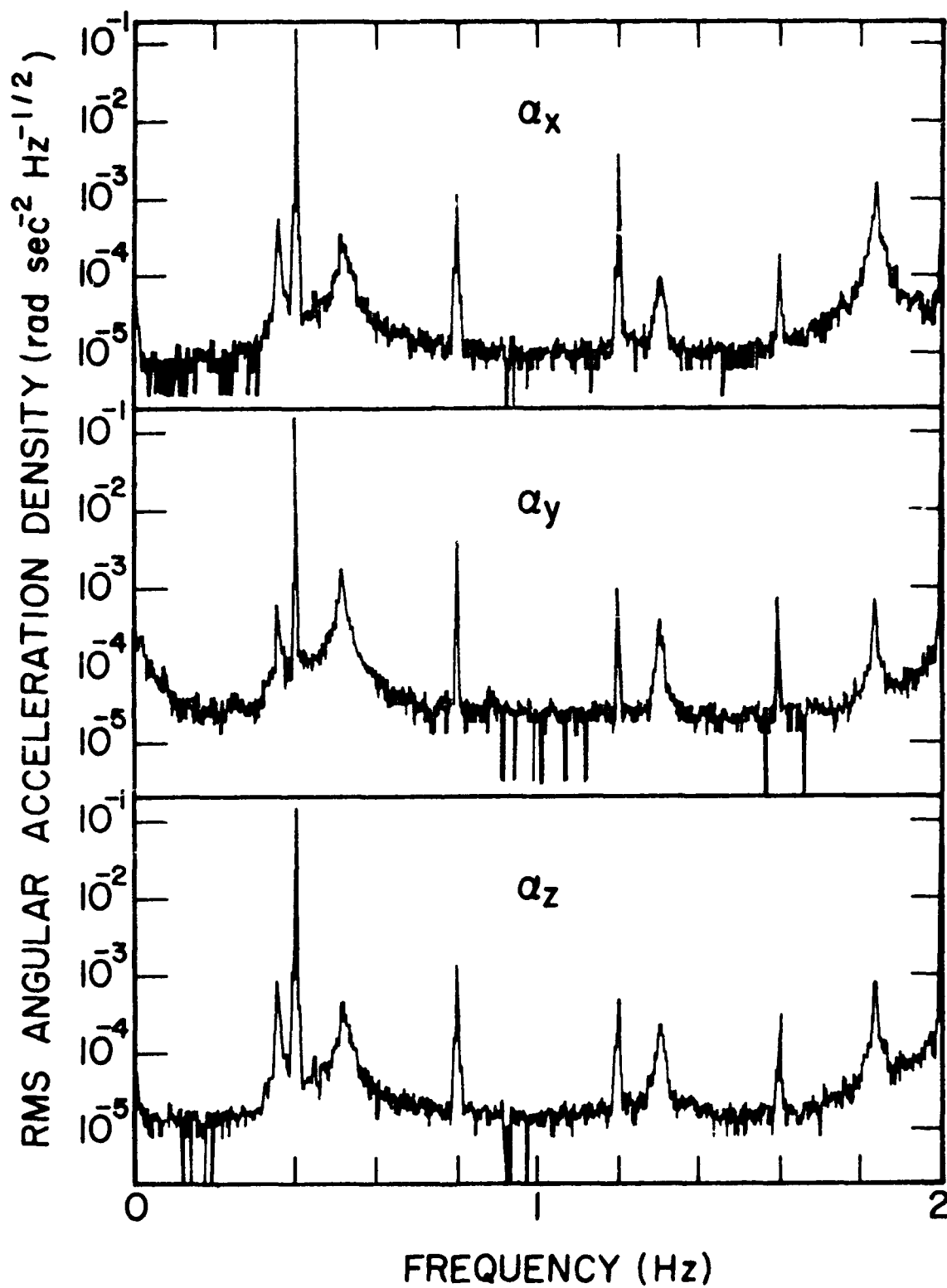


Figure 4.6. The low-frequency spectra of seismic noise as measured by the θ_x , θ_y , and θ_z sensing circuits.

where β_{θ_x} , β_{θ_y} , and β_{θ_z} are, from Eq. (2.234),

$$\beta_{\theta_x} = \frac{1}{2} \left(\frac{I_{\theta_x} c \Lambda_S}{L_{SQ} + 6L_S} \right)^2 \frac{L_{SQ}}{I \omega_{\theta_x}^2}, \quad (4.105)$$

$$\beta_{\theta_y} = \frac{1}{2} \left(\frac{I_{\theta_y} c \Lambda_S}{L_{SQ} + 6L_S} \right)^2 \frac{L_{SQ}}{I \omega_{\theta_y}^2}, \quad (4.106)$$

$$\beta_{\theta_z} = \frac{1}{2} \left(\frac{I_{\theta_z} c \Lambda_S}{L_{SQ} + 6L_S} \right)^2 \frac{L_{SQ}}{I \omega_{\theta_z}^2}. \quad (4.107)$$

Substituting the experimental values of the sensing currents along with other parameters into these equations, we find

$$\beta_{\theta_x} = 2.0 \times 10^{-5}, \quad (4.108)$$

$$\beta_{\theta_y} = 1.8 \times 10^{-6}, \quad (4.109)$$

$$\beta_{\theta_z} = 8.7 \times 10^{-7}. \quad (4.110)$$

These couplings are extremely small and explain why we did not have to consider the contribution of the sensing currents to the angular resonance frequencies in the previous section. These small couplings severely limit the angular acceleration sensitivity of the present model of the SSA, as in the case of the linear accelerations. The couplings of the new design should be much larger, and the SSA should approach its potential sensitivity.

Substituting $E_S = 10^{-28}$ J/Hz for the Quantum Design RF SQUIDS, the experimental parameters, and the values for the energy coupling coefficients into expressions for the power spectral density, Eqs. (4.102) through (4.104), we find

$$P_{\alpha_x}^{1/2} = 6.7 \times 10^{-8} \text{ rad/sec}^2 / \sqrt{\text{Hz}}, \quad (4.111)$$

$$P_{\alpha_y}^{1/2} = 2.2 \times 10^{-7} \text{ rad/sec}^2 / \sqrt{\text{Hz}}, \quad (4.112)$$

$$P_{\alpha_z}^{1/2} = 3.5 \times 10^{-7} \text{ rad/sec}^2 / \sqrt{\text{Hz}}. \quad (4.113)$$

Again, the white noise level of the SQUID amplifier can be observed directly at frequencies above 40 Hz. Dividing this noise level by the measured sensitivities, Eqs. (4.90) through (4.92), we find

$$P_{\alpha_x}^{1/2} = 4.8 \times 10^{-8} \text{ rad/sec}^2 / \sqrt{\text{Hz}}, \quad (4.114)$$

$$P_{\alpha_y}^{1/2} = 1.7 \times 10^{-7} \text{ rad/sec}^2 / \sqrt{\text{Hz}}, \quad (4.115)$$

$$P_{\alpha_z}^{1/2} = 2.1 \times 10^{-7} \text{ rad/sec}^2 / \sqrt{\text{Hz}}. \quad (4.116)$$

These are in reasonable agreement with the theoretical noise limits.

4.4 Future Improvements

The present design of the SSA works, and the measurements of its parameters agree quite well with theory. Analysis of the experimental results points out several areas in which improvement can be made: 1) The minimum detectable signal can potentially be increased several orders of magnitude by increasing the electro-mechanical coupling, β . 2) The sources of the $1/f$ noise must be determined and reduced. 3) The device must be operated in the closed-loop mode to increase the maximum detectable acceleration signal and reduce nonlinearity.

The electro-mechanical coupling can be most easily increased by raising the bridge drive current, I_r . However, the misbalance in the resistive component of the bridge circuit imposes a limit on the current, as discussed in Section 4.3.2. In order to achieve better matching between the coils, it is necessary to use single layer coils for both levitation and sensing. However, this reduces the inductance of the levitation coils and so increases the current required for levitation. One way to avoid approaching the critical current of the wire is to use a single large coil on each active face of the coil form in place of the separate sensing and levitation coils. This configuration requires the sensing/levitation circuit for each axis to have a separate SQUID, but it has the advantage that the single coils are much easier to fabricate. Furthermore, the single coil will have a much larger value of λ_S : approximately 5.7 times the present value. It is expected that with these improvements, a bridge drive current in excess of 1 Amp will be attained. Assuming the resonance frequency is kept the same as that of the present model, β should be approximately 10^3 time larger than current values, implying a minimum detectable signal 10^3 times lower.

As discussed briefly in Section 4.3.3, one likely source of $1/f$ noise is flux creep in Nb-Ti. Flux creep should be greatly reduced by using Nb in all the superconducting circuits. Switching back to Nb at this point is reasonable because of a better understanding of how the processing of the Nb wire affects its mechanical properties. In addition, using only a single set of coils for both levitation and sensing simplifies the overall design.

Like most conventional accelerometers, the SSA should operate best in a feedback loop: The six demodulated outputs are fed into a controller which applies current to the six levitation circuits to maintain the balance of the bridges. In this way, the effective bandwidth of the device can be pushed to several times the natural resonance

frequency. The controller also provides damping. Because the open loop system is lightly damped, a large acceleration impulse or strong acceleration noise often causes a signal at the resonance frequency large enough to exceed the slew rate of the SQUID amplifier. By providing damping, the maximum readable signal is increased. In the present circuit, all the sensing bridges are directly connected, so the spacing between the carrier frequencies limits the bandwidth allotted to each axis, and thus the ultimate effective bandwidth attainable using a controller. By using separate SQUIDs for each axis, the ultimate bandwidth of the accelerometer should be limited by the carrier frequency if coupling between the circuits through stray inductances can be made negligible.

A new version of the accelerometer has been designed incorporating the above changes. The Model II SSA will have only 24 coils connected in six independent bridge circuits that will provide both levitation and sensing. Each bridge will have its own SQUID amplifier. A simple PID (proportional, integral, differential) controller has recently been built and tested on the present version of the SSA. Using the results of these tests, an improved controller will be built for the Model II SSA. With these improvements, substantial improvement in sensitivity, especially in the crucial low frequency region, should be attained.

Bibliography

- [1] D. C. Agnew and J. Berger. Vertical seismic noise at very low frequencies. *J. Geophys. Res.*, 83(11):5420, 1978.
- [2] J. N. Brune and J. Oliver. The seismic noise of the earth's surface. *Bull. Seism. Soc. Am.*, 49(4):349, 1959.
- [3] H. A. Chan. *Null Test of the Gravitational Inverse Square Law with a Superconducting Gravity Gradiometer*. PhD thesis, University of Maryland, College Park, Maryland, 1982.
- [4] H. A. Chan, H. J. Paik, M. V. Moody, and J. W. Parke. Superconducting techniques for gravity survey and inertial navigation. *IEEE Trans. Magnetics*, MAG-21(2):411-414, 1985.
- [5] Alex J. Dragt. Class notes from classical mechanics. University of Maryland, College Park, Md.
- [6] J. N. Hollenhorst. *Signals and Noise in the rf SQUID*. PhD thesis, Stanford University, Stanford, California, 1979.
- [7] J. N. Hollenhorst and R. P. Giffard. Input noise in the hysteretic SQUID: theory and experiment. *J. Appl. Phys.*, 51:1719, 1980.
- [8] J. D. Jackson. *Classical Electrodynamics*. John Wiley & Sons, Inc., New York, 1975.
- [9] E. R. Mapoles. *Development of a Superconducting Gravity Gradiometer for a Test of the Inverse Square Law*. PhD thesis, Stanford University, Stanford, California, 1981.

- [10] H. J. Paik. *Analysis and Development of a Very Sensitive Low Temperature Gravitational Radiation Detector*. PhD thesis, Stanford University, Stanford, California, 1974.
- [11] H. J. Paik. *Development of a Sensitive Six-Axis Superconducting Accelerometer*. Proposal to the Air Force Geophysical Laboratory, University of Maryland, Department of Physics and Astronomy, 1984.
- [12] H. J. Paik. Superconducting inductance-bridge transducer for resonant-mass gravitational-radiation detector. *Phys. Rev. D*, 33(2):309-318, 1986.
- [13] William H. Press, Brian P. Flannery, Saul A. Teukolsky, and William T. Vetterling. *Numerical Recipes in C: The Art of Scientific Computing*. Cambridge University Press, New York, 1988.
- [14] Henry Stark and Franz B. Tuteur. *Modern Electrical Communications*. Prentice-Hall, Englewood Cliffs, New Jersey, 1979.
- [15] Anthony D. Whalen. *Detection of Signals in Noise*. Academic Press, New York, 1971.